UNIVERSITY OF CALIFORNIA, SAN DIEGO

Study of Inward Particle Flux in a Multi-instability Plasma System

A dissertation submitted in partial satisfaction of the requirements for the degree
Doctor of Philosophy

in

Engineering Sciences (Engineering Physics)

by

Lang Cui

Committee in charge:

George R. Tynan, Chair
Farhat N. Beg
Patrick H. Diamond
Richard A. Moyer
Kevin B. Quest

2015

The Dissertation of Lang Cui is approved, and it is acceptable in quality and form for publication on microfilm and electronically:

_____

_____

_____

_____

_____

Chair

University of California, San Diego

2015

DEDICATION

To my parents *Yikun* and *Yuhui*

TABLE OF CONTENTS

Signature Page iii

Dedication iv

Table of Contents v

List of Supplemental Files viii

List of Figures ix

List of Tables xv

Acknowledgements xvi

Vita xviii

Abstract of the Disseration xix

Chapter 1 Introduction and Background 1
1.1 Fusion 1
1.1.1 Fusion reaction 1
1.1.2 Magnetic Confinement 3
1.2 Drift wave turbulence-Zonal Flow System 5
1.2.1 Overview of Drift wave turbulence 5
1.2.2 Drift wave-Zonal flow system 10
1.2.3 Electrostatic plasma instabilities 17
1.3 Turbulent Particle Transport 19
1.3.1 Anomalous particle transport 19
1.3.2 Experimental observations of inward particle flux 23
1.4 The aim of this dissertation 29

Chapter 2 Experimental set up and methods of analysis 32
2.1 CSDX linear plasma machine 32
2.2 Upgraded CSDX 34
2.3 Plasma Diagnostics 37
2.3.1 The dual 3×3 Langmuir probe 37
2.3.2 The 4-tip turbulent Reynolds stress Langmuir probe 39
2.3.3 Mach probe 42
2.3.4 Data acquisition system 44
2.3.5 Laser induced fluorescence 44
2.3.6 High-speed imaging diagnostics 46
2.4 Methods for data analysis 50

2.4.1 General statistical analysis techniques 50
2.4.2 Bispectral analysis 53
2.4.3 Velocity measurements 56
2.4.4 Estimation of turbulent quantities in CSDX 58
2.5 Previous CSDX experimental research in the drift wave-zonal flow system 59

Chapter 3 Development of an up-gradient turbulent particle flux in a linear plasma device 71
3.1 Introduction 71
3.2 Experimental Setup 73
3.3 Experimental results 77
3.3.1 Motivation 77
3.3.2 Mean profiles 78
3.3.3 Observations of up-gradient particle flux using fast-speed camera 84
3.3.4 Comparison between the flux estimates from probes and imaging 90
3.3.5 Motion of turbulent structures 92
3.4 Summary and Discussion 95

Chapter 4 Examination of the link between flow shear and the development of inward particle flux 97
4.1 Introduction 97
4.2 Experimental studies of the relationship between shear flow and inward flux 99
4.2.1 Fluctuation-flow energy transfer reverses 99
4.2.2 Examination of causality 102
4.3 Study of nonlinear flow-fluctuation energy transfer in frequency domain 105
4.4 Discussion 112
4.5 Summary 114

Chapter 5 Study of underlying physics mechanism for inward particle flux in a multi-instability plasma system 115
5.1 Introduction 115
5.2 Fluctuation power spectra in CSDX-U 116
5.3 Flow shear-driven inward pinch 119
5.4 Inward pinch driven by ion mixing mode mechanism 123
5.4.1 Evidences of Ion Temperature Gradient (ITG) instability 123
5.4.2 Ion mixing mode driven inward pinch 130
5.5 Inward pinch driven by parallel flow shear 133
5.6 Summary 136

Chapter 6 Summary and future plans 138
6.1 Summary and discussion 138
6.2 Limitations of present work 143
6.3 Recommendation for Future Work 144
6.3.1 Better measurements for electron temperature T_e 144

6.3.2 Investigation of interaction between vorticity, density gradient and velocity shear.....147
6.3.3 Changing gas species from Argon to Helium /Hydrogen 148
6.3.4 A testing of ideas from linear machines on tokamak plasmas 148

References.....151

LIST OF SUPPLEMENTAL FILES

Movies showing light intensity fluctuations from Ar I for B = 1000G.
1000G(Coverted).mov

Movies showing light intensity fluctuations from Ar I for B = 1400G.
1400G(Coverted).mov

LIST OF FIGURES

Figure 1-1 The schematic of deuterium-tritium fusion reaction 2

Figure 1-2 The motion of charged particles in a uniform magnetic field. 4

Figure 1-3 Physical mechanism of a drift wave. [2] 7

Figure 1-4 Schematic of zonal electric field. The poloidal cross-section is shown here, where the hatched region and dotted region denote the positive and negative charges respectively. [9]. 10

Figure 1-5 Schematics of zonal flow-drift wave interaction for zonal flow with a wave vector k_{ZF} and two drift wave vectors k_1 and k_2 . Here $k_1 + k_2 = k_{ZF}$ with $k_1 , k_2 \gg k_{ZF}$ 11

Figure 1-6 Schematics of turbulence work on zonal flow. 13

Figure 1-7 (a)-(c) The stretching and decorrelation mechanism: eddies are torn apart. (d)-(f) The vortes thinning mechanism: the eddies are taken over by the zonal flow. 15

Figure 1-8 The paradigm of drift wave-zonal flow system for plasma turbulence. 16

Figure 1-9 Drift wave mechanism showing E × B convection [23] 20

Figure 1-10 The general case where the drift wave density fluctuations are shifted in phase from the potential fluctuations. This results in a net flux of density down the density gradient when the particle flux is integrated over a fixed radial surface. 21

Figure 1-11 (a) Density profile evolution in ECH heated plasmas. (b) The measured profile of the turbulent particle transport $\langle \tilde{n}\tilde{v}_\rho \rangle$, extrapolated to the whole flux surface, and a main ionization source $\langle S_n \rangle$ in the region of $0.99 \lesssim \psi \lesssim 1.01$.[38]..... 26

Figure 1-12 (a) the fluctuation-induced particle flux (b) before (diamonds) and after (squares) the transition from low to the fluctuating high confinement mode. (Right panel). [41]..... 27

Figure 1-13 For several bias values: (a) Radial profile of azimuthal velocity, with fit. (b) Radial profile of turbulent particle flux. [43]. 28

Figure 2-1 Schematic of the CSDX linear plasma device including setup of Langmuir probe and camera diagnostic. [21]. 33

Figure 2-2 Picture of the Controlled Shear De-correlation Experiment. [7]. 34

Figure 2-3 Comparison of time-averaged radial profiles between previous CSDX experiments (left panel; B = 1kG) and CSDX-U (right panel; B = 1.3kG). (a) Time averaged density $\langle n_0 \rangle$. (b) Gradient of the time-averaged density $-\frac{\partial \langle n \rangle}{\partial r}$. (c) Time-averaged azimuthal velocity $\langle v_\theta \rangle$ 36

Figure 2-4 Dual 3x3 Langmiur probe array, of which one 3x3 array (9 channels) is for floating potential and anther 3x3 array is for ion saturation current (or density). These two arrays shift in the axial direction by 1.5 mm [7,16]. 38

Figure 2-5 A circuit schematic of density and potential measurements. 39

Figure 2-6 The 4-tip turbulent flux probe array. (a) and (b) shows the position relative to the magnetic field line. (c) is a 3D sketch and (d) is a picture of the Langmiur probe array. One of the 3 short tips is for ion saturation current, and the rest (two short tips and one long tip) are for floating potential, as indicated in (b). [16] 40

Figure 2-7 Comparison between 18-tip probe (left panel) and 4-tip probe (right panel). Radial profiles of (a) mean density (b) turbulent particle flux. 41

Figure 2-8 Schematic view of Mach probe. 42

Figure 2-9 Evolution of parallel flow velocity measured by Mach probe. [21]. 43

Figure 2-10 Schematic of the LIF setup on CSDX. [58]. 45

Figure 2-11 (a) raw imaging data (b) mean subtracted fluctuating light intensity 47

Figure 2-12 (a) Raw ion saturation current signal from Langmiur probe (black line) and light intensity fluctuation from fast imaging (red line) as a function of time. (b) Cross-correlation between ion saturation current and light intensity fluctuations. 49

Figure 2-13 Time series of density fluctuations at three different radial locations for B = 2400G. [21]. 52

Figure 2-14 2D time-delay estimation (TDE) technique. [7]. 57

Figure 2-15 Radial profiles of the normalized standard deviations of potential (top panel) and density (bottom panel). [46]. 60

Figure 2-16 Radial profiles of potential fluctuation power spectrum with B filed. [46].. 60

Figure 2-17 Built-up in local k-spectra at 1000G. [46]. 61

Figure 2-18 Evolution of azimuthal flow with B field. [51]. 62

Figure 2-19 Evolution of azimuthal energy wave-number spectrum $\boldsymbol{E}(\boldsymbol{k_\theta})$ with magnetic fields. [77]..... 62

Figure 2-20 Radial profile of azimuthal velocity field measured from different methods. Blue curve: Mach probe data; Black diamonds: TDE inferred azimuthal velocity; black solid line: velocity from turbulent momentum conservation analysis; red curve: two-field turbulence simulation [12]. 64

Figure 2-21 Radial profiles of (a) mean density, (b) turbulent Reynolds stress, (c) mean square of turbulent radial velocity (d) diffusive turbulent transport term, (e) residual stress and (f) mean azimuthal velocity. [49]..... 66

Figure 2-22 Auto-spectra profiles (a) density, (b) potential and (c) azimuthal velocity for the weakly turbulent plasmas in CSDX (B = 1000G). [48]. 67

Figure 2-23 Frequency Resolved Net Kinetic Energy Transfer. Red shadow area indicates zonal flow frequency region and blue shadow area indicates the drift wave turbulence frequency region. [48]. 68

Figure 2-24 Sequential snapshots showing the birth, evolution, and death of vortex-like structures at weakly turbulence plasma state [55]. 69

Figure 3-1 Schematic of CSDX (include the layout of Langmuir probe and camera diagnostic at the experiment)..... 75

Figure 3-2 Evolution of turbulent particle flux. [21]..... 78

Figure 3-3 Radial profile of electron temperature. The profile at 1400G is plotted in red. 79

Figure 3-4 Time-averaged radial profiles of (a) mean density $\langle \boldsymbol{n_0} \rangle$ calculated from ion saturation current (b) RMS amplitudes of density fluctuations, normalized by the equilibrium density. 79

Figure 3-5 Time-averaged radial profiles of: (a) mean azimuthal velocity $\langle \boldsymbol{V_\theta} \rangle$ calculated by TDE (b) mean parallel velocity $\langle \boldsymbol{V_z} \rangle$ measured by Mach probe..... 81

Figure 3-6 Onset of up-gradient particle flux. Magnetic fields from 1000G to 1300G. .. 81

Figure 3-7 Cross-correlation coefficient between the Langmuir probe and the fast camera signals. 85

Figure 3-8 Snapshots of camera movies recording light of Ar I emission lines for three different magnetic fields (B = 1000G, 1400G and 2400G). Each pixel is normalized to its standard deviation to enhance contrast. 88

Figure 3-9 Frequency averaged velocity fields obtained from velocimetry of the camera movies shown in streamline plots at (a) B = 1000G and (b) 1300G. The direction of the magnetic field is ⊗. [82]. 90

Figure 3-10 Observation of inward flux by both fast camera and Langmuir probe: (a) Intensity flux $\langle \tilde{I}_c \tilde{V}_r \rangle$ (b) turbulent particle flux $\langle \tilde{n} \tilde{V}_r \rangle$. 92

Figure 3-11 (a) Radial velocity profiles for blobs (blue solid diamond) and holes (red solid diamond). (b) The sum of contribution of blobs and holes with amplitudes larger than one standard deviation to the particle flux (Black solid squares) and total particle flux (Red dash line). B = 1300G. [82]..... 94

Figure 4-1 Time-averaged radial profiles of (a) mean density $\langle \boldsymbol{n_0} \rangle$, (b) floating potential and (c) mean azimuthal velocity$\langle \boldsymbol{V_\theta} \rangle$..... 98

Figure 4-2 Time-averaged radial profiles of (a) turbulent particle flux $\langle \widetilde{\boldsymbol{n}} \widetilde{\boldsymbol{V}}_{\boldsymbol{r}} \rangle$, (b) mean total azimuthal Reynolds work $-\frac{\partial \langle \tilde{V}_r \tilde{V}_\theta \rangle}{\partial r} \langle \bar{V}_\theta \rangle$ and (c) mean total parallel Reynolds work $-\frac{\partial \langle \tilde{V}_r \tilde{V}_z \rangle}{\partial r} \langle \bar{V}_z \rangle$. 101

Figure 4-3 Causality: (a) Cross correlation between azimuthal velocity shearing rate and turbulent particle flux and (b) Cross correlation between mean parallel velocity and turbulent particle flux at r = 4.75cm, B = 1300G. 103

Figure 4-4 Envelope of cross correlation between azimuthal velocity shearing rate and turbulent inward particle flux. 104

Figure 4-5 Cross correlation between azimuthal velocity shearing rate and parallel velocity at r = 4.75cm, B = 1300G..... 105

Figure 4-6 Frequency-resolved turbulent particle flux for B = 1300G at different radial position. (a) *r* = 4.5 cm corresponding to a net inward particle flux location (b) *r* = 6 cm corresponding to the location of the shear layer. 106

Figure 4-7 Radially resolved cross-phase between density and potential for 4-6 kHz fluctuations at B = 1000G and B = 1300G. 107

Figure 4-8 Total net kinetic energy transfer rate for B = 1300G at r = 6cm. Here a negative value means that frequency f is losing energy and a positive value means that it is gaining energy. [82]..... 109

Figure 4-9 Total net kinetic energy transfer rate for B = 1300G at r = 4.5cm. [82] 110

Figure 4-10 Filtered at f = 5 kHz, sequential visible light emissions images at B = 1300G. Radii of r = 3 cm and r = 5 cm are denoted by the two dashed circles. 111

Figure 4-11 Schematic view of energy transfer in *k-space* and turbulent particle flux in configuration space. 113

Figure 5-1 Evolution of frequency spectra and cross-phases with magnetic field: radially resolved frequency spectra obtained from fluctuations of ion saturation current (column 1), floating potential (column 2) and cross-phase between density and potential (column 3). [21] 118

Figure 5-2 Equilibrium profiles used for linear analysis: (a) Density, (b) $\mathbf{E} \times \mathbf{B}$ azimuthal flow velocity from LIF measurement, obtained by fitting a Gaussian to the experimentally measured data. 120

Figure 5-3 Linear growth rates for n=1 modes as a function of azimuthal mode number for B = 1200G with $\boldsymbol{V_{EXB}}$ flow (shown in black line) and without $\boldsymbol{V_{EXB}}$ flow (red line). 121

Figure 5-4 Cross phase of density and potential for n = 1, m = 4 mode with $\boldsymbol{V_{EXB}}$ flow (shown in solid line) and without $\boldsymbol{V_{EXB}}$ flow (dash line). Here a positive value in cross-phase indicates a mean outward flux and negative indicates inward flux. 122

Figure 5-5 Radial profiles of (a) ion temperature $\boldsymbol{T_i}$ measured by LIF and (b) mean density measured by Langmuir probe. 124

Figure 5-6 Ion and electron fluctuation features observed from fast imaging. 125

Figure 5-7 Space–time plots of normalized light fluctuations in an azimuthal circumference at r = 1.7 cm for the magnetic field B = 1600G: (a) unfiltered, (b) high pass zero phase frequency filtered with a cutoff frequency of 25 kHz. 127

Figure 5-8 Eigenfunction for maximum growing modes (m=7-8). 130

Figure 5-9 Type of ion temperature and density profiles leading to the excitation of ion-mixing modes. 131

Figure 5-10 Radial profiles of old CSDX experiments: (a) Equilibrium density profiles; (b) equilibrium electron temperatures. 133

Figure 5-11 Radial profiles parallel flow velocity by LIF measurement. 134

Figure 6-1 (a) I–V –characteristics for two different magnetic fields (b) for the lowest detected values and (c) obtained at the start of exponential increase of electron current. [21] 145

Figure 6-2 Schematic of triple probe measurement. 146

LIST OF TABLES

Table 1-1 Properties of instabilities in a magnetized plasma column. [18,21] 19

Table 5-1 Evidence for ITG modes excited at higher B field from both experimental observation and linear studies. 129

Table 6-1 Relevance of this dissertation to Tokamak physics. [83] 150

ACKNOWLEDGEMENTS

I am feeling truly thankful for people that have helped me in the journey of pursuing my dream, without whom I could never make this far. This is a great opportunity to express my gratitude to all those people who have given me the possibility to complete this dissertation.

First and foremost I thank my advisor Professor George Tynan, for giving me the opportunity to be his student. He is knowledgeable, respectable, generous and always caring for his students. He provided me with an excellent atmosphere and independence for doing research. To me, George is more than a mentor. He not only taught me about plasma physics but also shared with me his experience in academic careers and life in general. I owe my deepest gratitude to George.

I'd like to give my sincere thanks to Dr. Min Xu, who have provided me with a lot assistance and guidance in both research and life in US. He is like a big brother to me, considerate and reliable. There were times when I questioned about myself. Min always encouraged me and gave me lots of invaluable suggestions for life. His patience and support helped me overcome many difficult situations during my PhD.

I also owe deep gratitude to a number of professors and scientists who offered me excellent lectures during the last five years in UCSD, Professor Sergei I. Krasheninnikov, Thomas M. O'Neil and particularly to Professor Patrick H. Diamond, who are well-known for their outstanding intuition in physics and devotion to science. Thank Pat for his guidance of the plasma theory in my research.

I would also like to express my devout thanks to all the scientists and engineers in CSDX and PISCES group, including Russ Doerner, Christopher Holland, Jonathan Yu, Daisuke Nishijima, Leo Chousal, Rolando Hernandez, Ray Seraydarian, Saikat. C. Tharkur, Weiwen Xiao, Payam Vaeri, Arash Ashourvan, Rongjie Hong and all others, who have helped me a lot in innumerable ways.

The UCSD MAE department and CER staff are really helpful and did excellent jobs. In particular I would like to thank Charlotte Lauve, Sandra de Sousa, Linda McKamey, Brandi Pate, Sandy Rosas, and Teresa Johnston for treating me so nicely and kindly all the time.

I am feeling very lucky to have so many amazing friends along with this journey, both in US and in China. My life in San Diego would not have been so nice without all my wonderful friends. You are all very important to me and thank you from bottom of my heart for your support and accompanies.

Most of all, I want to thank my parents, Yikun Cui and Yuhui Li. Their love, unconditional support and encouragement make the way worth it.

Chapter 3 and Chapter 4, in part, has been accepted for publication of the material as it may appear in “Up-Gradient Particle Flux in Drift wave- Zonal Flow Systems”, L. Cui, G. R. Tynan, P.H. Diamond, S.C. Thakur and C. Brandt, Phys. Plasmas, 2015. The dissertation author was the primary investigator and author of this paper.

VITA

2010	B.S., Physics, University of Science and Technology of China, Hefei, China
2010-2015	Graduate Student Researcher, Center for Energy Research, University of California, San Diego, California, USA
2015	Ph.D., Engineering Sciences, University of California, San Diego, California, USA

PUBLICATIONS

L. Cui, G. R. Tynan, P. H. Diamond, S. C. Thakur and C. Brandt, "Up-Gradient Particle Flux in Drift wave- Zonal Flow Systems", Phys. Plasmas **22**, 050704 (2015).

S. C. Thakur, C. Brandt, L. Cui, J. J. Gosselin, A. D. Light, and G. R. Tynan, "Multi-instability plasma dynamics during the route to fully developed turbulence in a helicon plasma", Plasma Sources Sci. Technol. 23 044006 (2014)

S. C. Thakur, C. Brandt, A. Light, L. Cui, J. J. Gosselin, and G. R. Tynan, "Simultaneous use of camera and probe diagnostics to unambiguously identify and study the dynamics of multiple underlying instabilities during the route to plasma turbulence", Review of Scientific Instruments 85, 11E813 (2014)

FIELDS OF STUDY

Major Field: Engineering Sciences (Engineering Physics)

Studies in Plasma Physics

Professor George R. Tynan

ABSTRACT OF THE DISSERATION

Study of Inward Particle Flux in a Multi-instability Plasma System

by

Lang Cui

Doctor of Philosophy in Engineering Sciences (Engineering Physics)

University of California, San Diego, 2015

Professor George R. Tynan, Chair

We report the observation of a *net inward, up-gradient* turbulent particle flux which occurs when a collisional drift waves generate a sufficiently strong radially sheared azimuthal zonal flow in a cylindrical magnetized plasma. At low magnetic fields ($B \leq 1.0$ kG), particle transport is outward at all radii. As the magnetic field is further increased to 1200G, an up-gradient inward particle flux develops between the peak of the velocity shear and the maximum density gradient. The mean density

gradient is also observed to steepen in response to this inward flux. Time-domain and bispectral Fourier domain analysis shows that at the peak of the velocity shear, where the particle flux is outward, the turbulent Reynolds stress acts to reinforce the shear flow. In contrast, in the region of the inward particle flux, the zonal flow drives the fluctuations, and a transient increase in the shearing rate is occurs prior to an increase in the magnitude of the inward flux. The results suggest a hypothesis in which the shear flow is responsible for the up-gradient particle flux and the corresponding steepening in the mean density gradient. However, a linear instability analyses using experimentally measured density and $\mathbf{E} \times \mathbf{B}$ flow profiles in a linear, modified Hasegawa-Wakatani theory model with the coupled potential and density fluctuations failed to reproduce the essential elements of our experimental observations, suggesting some other mechanism is responsible for the inward flux. We summarize recent new experimental results which point towards the possible role of finite ion temperature gradient effects, possibly combined with parallel flow shear, in driving up-gradient particle flux

Chapter 1

Introduction and Background

1.1 Fusion

1.1.1 Fusion reaction

Nuclear fusion is one of the most promising options for generating large amounts of carbon-free energy in the future. Fusion is the process that heats the Sun and all other stars, where atomic nuclei collide together and release energy. To get energy from fusion, gas from a combination of types of hydrogen – deuterium and tritium – is heated to very high temperatures (100 million degrees Celsius). Controlled fusion may be an attractive future energy options. There are several types of fusion reactions. Most involve the isotopes of hydrogen called deuterium and tritium. The typical fusion reactions are given as below:

$$D^3 + D^2 \rightarrow He^2(0.817MeV) + n^1(2.45MeV) \quad (1.1)$$

$$D^2 + D^2 \rightarrow T^3(1.01MeV) + H^1(3.02MeV) \quad (1.2)$$

$$D^2 + T^3 \rightarrow He^4(3.50MeV) + n^1(14.1MeV) \quad (1.3)$$

$$D^2 + He^3 \rightarrow He^4(3.67MeV) + H^1(14.7MeV) \quad (1.4)$$

So far most promising method for fusion achievement is considered to through reaction by Eqn. (1.3) due to the fact that this reaction needs least energy and has largest nuclear cross section. As shown in Figure 1.1, every fusion reaction can provide 17.6 MeV nuclear energy of which 3.5 MeV is carried by α particles (helium nuclei) and the rest is carried by the neutron. Since both deuterium and tritium nuclei are carrying positive charges, we need to heat deuterium and tritium to a sufficiently high temperature (~ 10 keV) in order that thermal velocities of nuclei are high enough to overcome the Coulomb repulsion force to produce the fusion reaction.

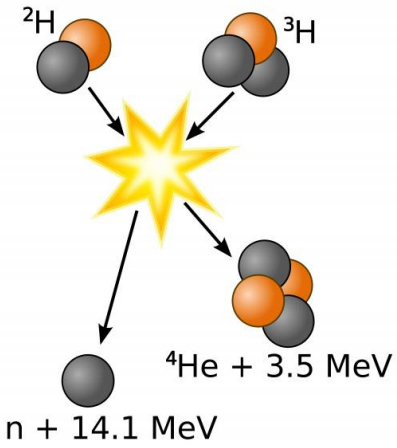

Figure 1-1 The schematic of deuterium-tritium fusion reaction

The conditions necessary for fusion energy gain are given by the famous Lawson criterion [1]:

$$nT\tau_E \geq 5 \times 10^{21} m^{-3} \cdot keV \cdot s \tag{1.5}$$

n is the ion density, and T denotes the temperature of the plasma ions. The product of nT then corresponds to the plasma pressure, and is (usually) limited by magneto-hydro dynamic (MHD) stability for any particular magnetic confinement scheme, showing how good the particles are confined. τ_E is the energy confinement time, measuring the rate of the system loses energy to the environment. Thus there exists a minimum value of the energy confinement time τ_E defined as ratio of the total energy of the plasma W to power loss P_{loss}:

$$\tau_E = \frac{W}{P_{loss}} \tag{1.6}$$

1.1.2 Magnetic Confinement

There are two ways to achieve the temperatures and pressures necessary for hydrogen fusion to take place: Magnetic confinement uses magnetic and electric fields to heat and squeeze the hydrogen plasma. The most promising device for this is the ‘tokamak', a Russian word for a ring-shaped magnetic chamber. The ITER project in France is using this method. Inertial confinement uses laser beams or ion beams to squeeze and heat the hydrogen plasma. Scientists are studying this experimental approach at the National Ignition Facility of Lawrence Livermore Laboratory in the United States.

The magnetically confined controlled fusion approach works at low gas densities and the temperature to values considerably higher than that in the center of the sun. At these high temperatures all matter is in the plasma state, consists of a gas

of charged particles that experience electromagnetic interactions and can be confined by a magnetic field of appropriate geometry. As shown in Figure 1.2, the motion of electrically charged particles is constrained by a magnetic field. When a uniform magnetic field is applied the charged particles will follow spiral paths encircling the magnetic lines of force. The motion of the particles across the magnetic field lines is restricted and so is the access to the walls of the container.

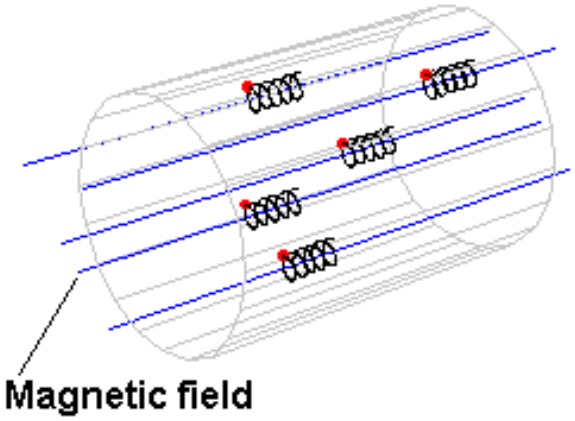

Figure 1-2 The motion of charged particles in a uniform magnetic field**.**

When a single charged particle subject to a force $\vec{F}$ is presented in an externally imposed magnetic field, the charged particle (ion/electron) will gyrate around the magnetic field lines. At the position of the guiding center, the charged particle will drift with a velocity which can be calculated from the fluid momentum equation, $V_D = \frac{\vec{F}\times\vec{B}}{B^2}$. The force can be due to an electric field ($\vec{E}\times\vec{B}$ drift), gravitational field, curvature drift ($\nabla\vec{B}$ drift) .etc. when there is a collection of charged

particles, the force can also be a mean pressure gradient ∇p_0 which can lead the particles to a diamagnetic drift with $V_d = -\frac{\nabla p_0 \times \vec{B}}{qnB^2}$. The diamagnetic drift depends to the sign of the charge the particles carried, thus we expect to find a diamagnetic current $\vec{J} \times \vec{B} = \nabla p_0$ in azimuthal direction and opposing the original magnetic field.

1.2 Drift wave turbulence-Zonal Flow System

1.2.1 Overview of Drift wave turbulence

It is known that drift waves result from the interaction between the dynamics perpendicular and parallel to the magnetic field due to the combined effects of spatial gradients, ion inertia, and electron parallel motion. Here "drift" refers to the diamagnetic drifts (perpendicular to both density gradient and magnetic field) due to dominant pressure gradient with a small finite $k_\perp$ and $k_\parallel$. Derivation of drift wave dispersion relation can be found in many text books and review papers [2-4].

The experimental work performed in this dissertation was considered cool collisional plasma. An assumption is often made that $v_{thi} \ll \omega/k_\parallel \ll v_{the}$, where ω is the drift wave frequency, v_{thi} and v_{the} are the ion and electron thermal speed separately. Since drift waves have finite $k_\parallel$, electrons can move along magnetic field lines establishing a thermodynamic equilibrium among themselves. While the ion motions can be neglected. As a result, Landau damping is negligible. In absent of resonant particles, phase velocity distributions may reach to a fluid description of

electrons and ions. We may apply the 2D fluid model to describe the system. Accounting for the fast gyromotion along magnetic field of the electrons for density n and velocity $\vec{u}$, we have:

$$\frac{\partial n_e}{\partial t} + \nabla \cdot (n_e \vec{u}_e) = 0 \tag{1.7}$$

$$m_e n_e \left(\frac{\partial \vec{u}_\parallel}{\partial t} + \overrightarrow{(u} \cdot \nabla) \vec{u}_\parallel \right) = enE_\parallel + \nabla_\parallel p \tag{1.8}$$

where p is the electron pressure and $\parallel$ denotes the direction parallel to magnetic field. By taking the limit $m_e \to 0$ and $\vec{\mathrm{E}} = -\nabla\phi$, a plane wave solution of the potential, $\phi = \phi_k exp(i\vec{k} \cdot \vec{r} - iwt)$ we can then obtain the *Boltzmann relation* for electrons:

$$\frac{\tilde{n}}{n} = \frac{e\tilde{\phi}}{KT_e} \tag{1.9}$$

where n_0 and T_e are the equilibrium electron density and temperature, $\frac{e\tilde{\phi}}{KT_e} \ll 1$. The schematics showing the physical mechanism of an electron drift wave can be seen in Figure 1.3, where the density perturbation is positive, the potential perturbation is positive. Similarly, where the density perturbation is negative, the potential perturbation is negative. The resulting electric field will cause a $\vec{E} \times \vec{B}$ drift in the x direction. Since there is a gradient ∇n_0 in the x direction, the $\vec{E} \times \vec{B}$ drift will bring plasma of different density to a fixed point. Along with the quasi-neutrality condition $\tilde{n}_e \approx \tilde{n}_i = n$, we can find the drift wave dispersion:

$$\frac{\omega}{k_y} = -\frac{KT_e}{eB_0} \frac{\nabla n_0}{n_0} \tag{1.10}$$

We notice that the drift waves travel with the electron diamagnetic drift velocity. Here the density and potential perturbations are in phase with a zero growth rate. Thus the plasma is stable.

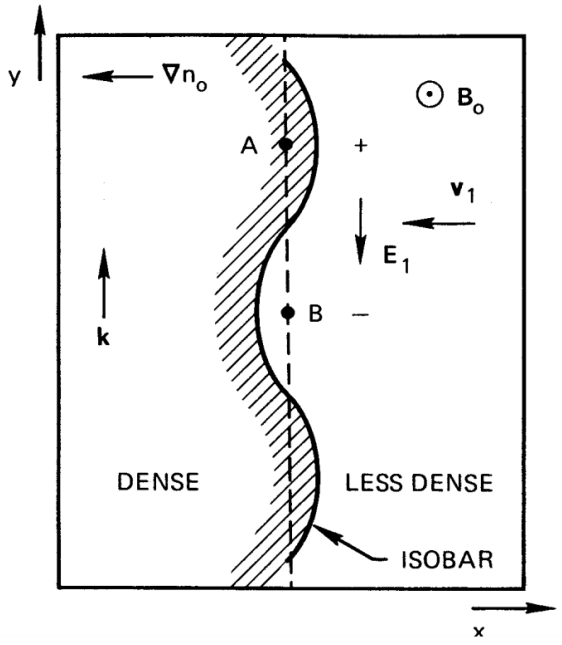

Figure 1-3 Physical mechanism of a drift wave. [2]

The fundamental property of electrostatic plasma turbulence is the drift wave frequency range in the absence of dissipation is often described by the Hasegawa-Mima Equations [5-7]. However, most experimental plasma condition is collisional like ours. Thus we are introducing a collisional drift-wave model described by Hasegawa-Wakatani equations, which derived from the same density continuity equation and electron momentum equation, but includes the electron parallel

dissipation and the modifications of ion-neutral drag [5,8]. In a cylindrical geometry such as our machine, this model is written as two coupled dimensionless equations:

$$\left(\frac{\partial}{\partial t} - \vec{\nabla}\tilde{\phi} \times \hat{z} \cdot \vec{\nabla}\right)\vec{\nabla}_{\perp}^{2}\tilde{\phi} = c_1\left(\tilde{\phi} - \tilde{n}\right) + c_2\vec{\nabla}_{\perp}^{4}\tilde{\phi} \tag{1.11}$$

$$\left(\frac{\partial}{\partial t} - \vec{\nabla}\tilde{\phi} \times \hat{z} \cdot \vec{\nabla}\right)(\tilde{n} + \ln n_0) = c_1\left(\tilde{\phi} - \tilde{n}\right) \tag{1.12}$$

where $c_1 = k_{\parallel}^2 v_{the}^2/\nu_e\omega_{ci}$ is the "adiabatic parameter" and $c_2 = \mu_{ii}/\rho_s^2\omega_{ci}$ is the normalized ion viscosity. We note here the density is normalized with n_0, the potential with $\frac{KT_e}{e}$, time with $1/\omega_{ci}$, distance with $\rho_s = \frac{C_s}{\omega_{ci}}$, gyroradius. Here $k_{\parallel}$ is the wavenumber parallel to magnetic field, ν_e is the electron collision frequency. Typically, the plasma is characterized by the ratio between the spatial scale of the collective modes (ρ_s) and the scale of the plasma (L_n). HW model introduces the two main components to describe a weak drift wave turbulence system: linear instability driving mechanism and nonlinear damping for turbulence saturation.

For $c_1 \gg 1$, parallel collisions are negligible thus the drift waves are linearly stable. Eqn. (1.11) and (1.12) will be reduced to the Hasegawa-Mima model:

$$\frac{\partial}{\partial \mathrm{t}}\left(\tilde{\phi} - \vec{\nabla}_{\perp}^{2}\tilde{\phi}\right) - \left(\vec{\nabla}\tilde{\phi} \times \hat{z} \cdot \vec{\nabla}\right)\vec{\nabla}_{\perp}^{2}\tilde{\phi} + \frac{1}{L_n}\frac{\partial}{\partial y}\tilde{\phi} = 0 \tag{1.13}$$

However, for $c_1 \ll 1$ this model goes to the hydrodynamic limit and reduces to the 2D Euler fluid equations.

Our experiments correspond to the condition $c_1 \approx 1, \frac{\rho_s}{L_n} \approx 0.1 - 0.3, c_2 \approx 0.2 - 0.3$. In the presence of dissipation of the parallel electron motion (electrons can lose momentum to the background plasma as they move parallel to the magnetic field), the corresponding dissipation will cause a finite phase shift between density and potential fluctuations. As a result of the phase shift, the Boltzmann relation is no longer valid with $\delta \neq 0$:

$$\frac{\tilde{n}}{n_0} = \frac{e\tilde{\phi}}{KT_e}(1 - i\delta) \tag{1.14}$$

here the phase shift δ is the key for instability. The dispersion relation becomes:

$$\omega^2 + i\sigma_{\parallel}(\omega - \omega_*) = 0 \tag{1.15}$$

where $\omega^* = -\frac{k_y k_B T_e}{eB_0}\frac{\nabla n_0}{n_0}$ and $\sigma_{\parallel} = \frac{k_{\parallel}^2 \omega_{ce}\omega_{ci}}{k_y^2}$. By solving for ω, we obtain

$$\omega \approx \omega_* + i(\omega_*^2/\sigma_{\parallel}) = 0 \tag{1.16}$$

As we can see from Eqn. (1.16), the growth rate $\mathrm{Im}(\omega(k))$ is always positive for a limited range of wavenumbers. This can be also understood from Fig. 1-3 that the phase shift causes $\vec{E} \times \vec{B}$ drift velocity outwards where the plasma is already shifted outward. Hence the perturbation grows. The dissipation of parallel electron motion can occur via several different processes such as wave-particle interactions and electron-ion Coulomb collisions.

1.2.2 Drift wave-Zonal flow system

The phrase "zonal flow" originally referred to the large-scale quasi two-dimensional atmosphere of rapidly rotating flow. In fusion plasma, zonal flow is observed in tokamaks as the toroidally (predominantly azimuthal) symmetric electric field fluctuations ($k_\theta = k_z = 0$. k_θ and k_z denote the poloidal and toroidal wavenumber) and radially localized (k_r finite. k_r denotes the radial wavenumber). Figure 1-4 illustrates the typical structure of zonal flow [9]. It is clear to see that the variation of the electric field perturbation is in the radial direction. Thus the associated **E** × **B** flow is in the poloidal direction and changes sign with radius. As a consequence, the zonal flow motion cannot tap into the background free-energy source associated with the pressure gradient, and thus the zonal flow is predicted to be linearly stable and generated via a nonlinear kinetic energy transfer from drift waves to large scale sheared flow.

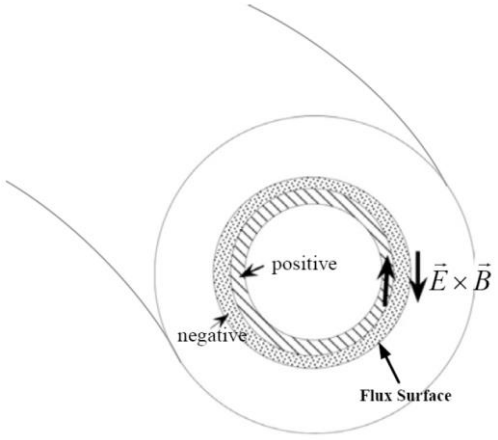

Figure 1-4 Schematic of zonal electric field. The poloidal cross-section is shown here, where the hatched region and dotted region denote the positive and negative charges respectively. [9]

The generation of zonal flows by turbulence is related to the inverse cascade in 2D fluid turbulence [10]. In 2D turbulence the strain field vanishes, i.e., $\frac{\partial V_z}{\partial z} = 0$ (z is along the vortex axis direction). So the vortex stretching does not occur, which leads to a dual cascade of energy and enstrophy. Thus both the kinetic energy and enstrophy are conserved [10]. In contrast, in 3D turbulence, there is a finite strain field $\frac{\partial V_z}{\partial z} \neq 0$ which causes the vortex tube stretch along the vortex axis. This allows both enstrophy and energy transfer to small spatial scales where energy is dissipated by viscosity in a direct energy cascade process [11]. In a strongly magnetized plasma, the dynamics can be considered to be 2D turbulence since turbulence correlation length parallel to B field is much larger than that perpendicular to B field. Thus the zonal flows are generated by the inverse cascade of drift waves via three wave coupling process, which satisfies criteria $\vec{k}_1 + \vec{k}_2 = \vec{k}_{ZF}$. $\vec{k}_1$ and $\vec{k}_2$ are the small-scaled turbulence wavenumbers and $\vec{k}_{ZF}$ is the large-scaled zonal flow wave number. Differ from 2D fluid turbulence, zonal flow formation is a non-local coupling process in wavenumber space.

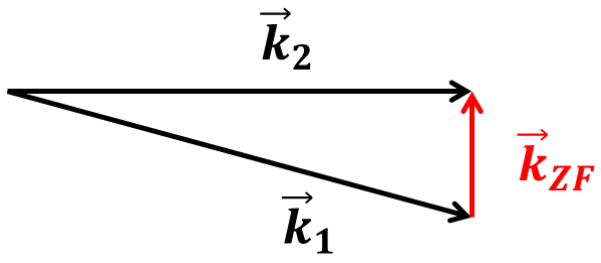

Figure 1-5 Schematics of zonal flow-drift wave interaction for zonal flow with a wave vector $\vec{k}_{ZF}$ and two drift wave vectors $\vec{k}_1$ and $\vec{k}_2$. Here $\vec{k}_1 + \vec{k}_2 = \vec{k}_{ZF}$ with $\vec{k}_1, \vec{k}_2 \gg \vec{k}_{ZF}$.

The physics mechanism of zonal flow generation by turbulence can be described by a simple model in a cylindrical plasma, with a finite flow damping rate μ : [12,13]

$$\frac{\partial \bar{V}_{ZF}}{\partial t} = -\frac{\partial}{\partial r}\langle \tilde{v}_\theta \tilde{v}_r \rangle - \mu \bar{V}_{ZF} \tag{1.17}$$

By taking a spatial Fourier transform of Eqn. (1.17) and multiplying by the complex conjugate $\bar{V}_{ZF}{}^*(\vec{k}_{ZF})$, we can have a new equation. Add this new equation to Eqn. (1.17), we can find the power spectrum evolution as,

$$\begin{aligned} &\frac{\partial \left|\bar{V}_{ZF}(\vec{k}_{ZF})\right|^2}{\partial t} + Re \sum_{\vec{k}_1,\vec{k}_2,\vec{k}_1+\vec{k}_2=\vec{k}_{ZF}} \langle\, \tilde{v}_\theta{}^*(\vec{k}_{ZF})\tilde{v}_\theta(\vec{k}_1)\tilde{v}_r(\vec{k}_2)\rangle \\ &\qquad = -\mu \left|\bar{V}_{ZF}(\vec{k}_{ZF})\right|^2 \end{aligned} \tag{1.18}$$

The third order quantity $\langle\, \tilde{v}_\theta{}^*(\vec{k}_{ZF})\tilde{v}_\theta(\vec{k}_1)\tilde{v}_r(\vec{k}_2)\rangle$ reveals the nonlinear transfer of kinetic energy in k space across spatial scales shown in figure 1-5. Energy is conserved in this process, leading to the ZF extracting energy from turbulence and thereby reducing turbulence amplitude.

The time averaged product of slowly varying and fluctuating components $\langle \tilde{v}_\theta \tilde{v}_r \rangle$ is known as the turbulent Reynolds stress, which is the flux of turbulent momentum. The radial gradient of turbulent Reynolds stress is the poloidal component of Reynolds force:

$$F_\theta = -\frac{\partial}{\partial r}\langle \tilde{v}_\theta \tilde{v}_r \rangle \tag{1.19}$$

It is clear to see that the poloidal (azimuthal) flow can be accelerated if the turbulent Reynolds stress $\langle \tilde{v}_\theta \tilde{v}_r \rangle$ is nonzero and has a radial gradient as it is shown in figure 1-6. As it is already know that the rate of Force *F* doing work is called power. Thus we can define the rate of work done by turbulent Reynolds stress on zonal flow as:

$$P_\theta = F_\theta \bar{V}_{ZF} = -\frac{\partial \langle \tilde{v}_\theta \tilde{v}_r \rangle}{\partial r} \bar{V}_{ZF} \tag{1.20}$$

P_θ is the so-called turbulent Reynolds work. Here a positive value of Reynolds work indicates a turbulent-driven shear flow, while a negative value shows the fluctuations are extracting energy from the flow.

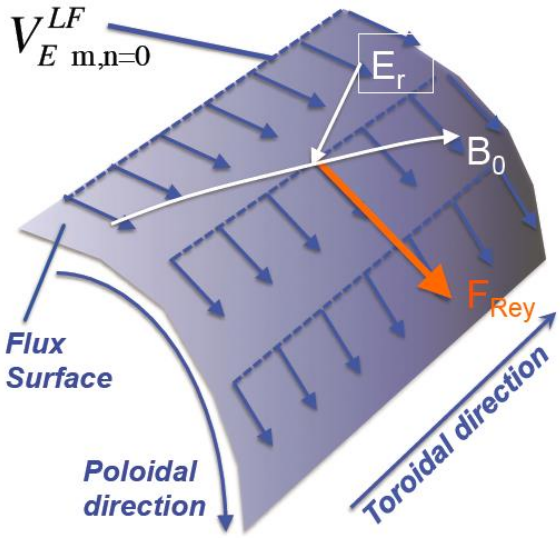

Figure 1-6 Schematics of turbulence work on zonal flow.

The most important reason why zonal flow is important for fusion plasma physics is due to the essential role zonal flow plays in the reduction and regulation of turbulence. Experimentally has been studied that zonal flow suppressed the turbulent transport in two mechanisms [14]. The first is the stretching and decorrelation shown in figure 1-7(a). In the case of a smooth, mean shear flow, the shearing tilts turbulent eddies, narrowing the radial extent and elongating them. Thus the energy is transferred from the turbulent eddies to the zonal flow. The breaking up of eddies does not cause further energy transfer to the zonal flow, but it reduces the step size of turbulent diffusion and therefore should reduce transport. The second is the vortex thinning mechanism as shown in figure 1-7(b), which results in the smaller eddies coiled up by the zonal flow instead of breaking apart. In this process the entire energy of the eddy can be transferred to the zonal flow and additional energy is taken out of the fluctuations which drive the turbulent transport.

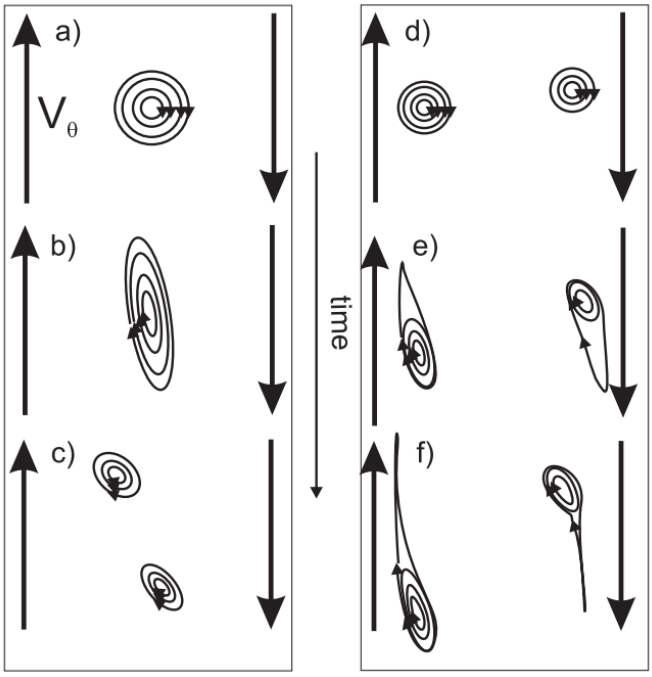

Figure 1-7 (a)-(c) The stretching and decorrelation mechanism: eddies are torn apart. (d)-(f) The vortes thinning mechanism: the eddies are taken over by the zonal flow. [14]

Based on the above discussion, we can clearly see that drift wave turbulence and zonal flows are closely coupled: on the one hand drift turbulence can generate large scale zonal flows through the typical three-wave interaction, in which small-scale turbulent eddies nonlinearly transfer their kinetic energy and momentum into a large-scale zonal structure to maintain it against damping; on the other hand zonal flows can actively shear turbulent eddies into smaller ones, at which scale the dissipation of kinetic energy and enstrophy of those smaller eddies are stronger. Both of the generation and shearing processes of zonal flows can effectively reduce the

turbulence intensity and the resulting turbulent energy and particle transport, thus will lead to a better plasma confinement. Also note that both the mean shear flow and the zonal flow can reduce the transport by altering the wave-particle interaction time, which determines the "cross-phase", even for fixed turbulence intensity. Due to this feedback loop between zonal flows and turbulence, plasma turbulence now can be regarded as a combination of drift waves and zonal flows, which interact with each other and self-regulate to reach an equilibrium state, are often referred to as drift wave-zonal flow turbulence. This process is schematically shown in Figure 1-8 [9,15,16].

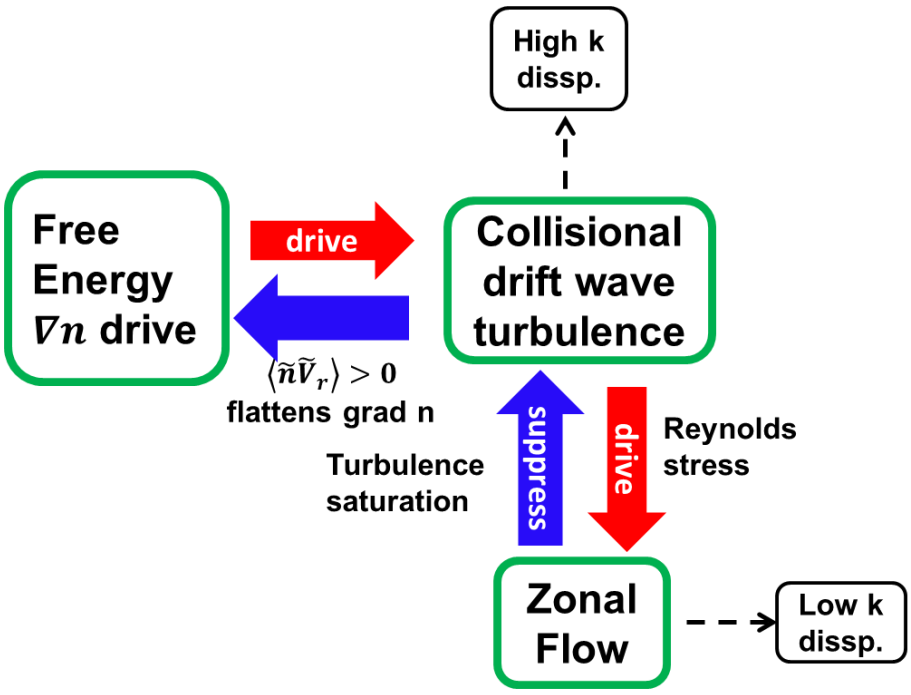

Figure 1-8 The paradigm of drift wave-zonal flow system for plasma turbulence.

Density or temperature gradients generate turbulence, which causes an enhanced turbulent transport. And the generated turbulence also nonlinearly transfer their energy and momentum to zonal flows, in which process reduces the turbulence intensity. Zonal flows will also give a back-reaction on turbulence to further reduce its intensity by either shearing or trapping. Due to their symmetry, zonal flows do not contribute to transport, and therefore serve as benign reservoir of free energy in the system.

1.2.3 Electrostatic plasma instabilities

In a drift wave-zonal flow system, in addition to drift wave instability the presence of shear in the flow of neutral fluids and plasmas can give rise to instability of the sheared layer, i.e., the Kelvin-Helmholtz (K-H) instability and stabilization of other instabilities, such as the interchange mode (Rayleigh-Taylor (R-T) instability) [17]. In magnetized cylindrical plasma devices with strong radial potential and density gradients, by linearizing the ion continuity and electron momentum equations, we have the reduced single linear ordinary differential equation for the radial displacement of particle guiding centers [18]:

$$\frac{d}{dr}\left\{nr^3(\omega-\omega_E)(\omega-\omega_E-\omega_D)\frac{d\psi}{dr})\right\}$$
$$-\frac{m^2-1}{r^2}nr^2(\omega-\omega_E)(\omega-\omega_E-\omega_D)\psi$$
$$+i\frac{2\Sigma nr^3}{a^2}\frac{(\omega-\omega_E)(\omega-\omega_E-\omega_D)}{\omega-\omega_E+i\Sigma}\psi \qquad (1.21)$$
$$-ina^2r^2(\omega+\omega_D-\omega_E)\nabla_\perp^4(r\psi)=0$$

where a is the ion gyroradius, $\omega_E=-mcE/rB$ and $\omega_D=-\frac{mckT}{eBr}n^{-1}\frac{dn}{dr}$. The resulting equation contains four terms that may act as free energy sources of plasma instability. The first two terms $\sim\left|\frac{d\Omega(r)}{dr}\right|$ where $\Omega(r)=v_\theta/r$ [19], present a velocity shear from which the K-H instability may arise. The second term $\sim\left\{-\frac{1}{n}\frac{\partial n}{\partial r}\right\}^{1/2}$ [20] presents a centrifugal effect due to plasma strong rotation that can act as a free energy source for R-T instability. The fourth term $\sim i\frac{\omega_{DW}^2}{\sigma_\parallel}$ characterizes the primary instability-Drift wave instability that arises from electron parallel resistivity. A table of experimental signatures derived from the radial wave equations given in Ref. [18] have previously been used to identify the instabilities in a cylindrical rotating plasma column like our machine, which is shown in Table 1-1.

Table 1-1 Properties of instabilities in a magnetized plasma column. [18,21]

Property	Resistive Drift wave	Kelvin-Helmholtz	Rayleigh-Taylor
localization	$Max(\omega_{dia,e})$	$Max(\omega_{E\times B})$	$Max\left\|\frac{1}{n}\frac{dn}{dr}\right\|$
$\tilde{\phi}/T_e\big\vert/\vert\tilde{n}/n\vert$	$\lesssim 1$	$\gg 1$	> 1
Cross-phase $\alpha(\tilde{n},\tilde{\phi})$	$< 45^{\circ}$	$90^{\circ}-180^{\circ}$	$45^{\circ}-90^{\circ}$
Parallel wavelength	$k_{\parallel} > 0$	$k_{\parallel} \approx 0$	$k_{\parallel} \approx 0$

1.3 Turbulent Particle Transport

1.3.1 Anomalous particle transport

Particle transport is a key issue in magnetically confined fusion plasmas since the fusion power increases with density. A peaked density profile is attractive to improve the fusion rate, which is proportional to the square of the density, and to self-generate a large fraction of non-inductive current required for continuous operation [22]. The energy losses observed in magnetic confinement devices are much greater than predicted by neoclassical transport theory and usually attributed to the presence of small-scale plasma turbulence. As was discussed above, the spatial gradients in the plasma lead to collective modes called drift waves, which have wave numbers in the range of the observed density fluctuations. The magnetized plasma will $\mathbf{E}\times\mathbf{B}$ convect

around the maximum and minimum of density variations. Figure 1-9 shows in schematics of the resulting dynamics in the "adiabatic" limit. The parallel motion of the particles allows the potential fluctuations in phase with density fluctuations. Due to the low-frequency feature of the drift waves, the ions and electrons will move along the magnetic field to establish the local thermodynamic equilibrium Boltzmann relation. Thus the resulting motion of the particles does not give rise to a net density convection that is integrated across a given radial surface.

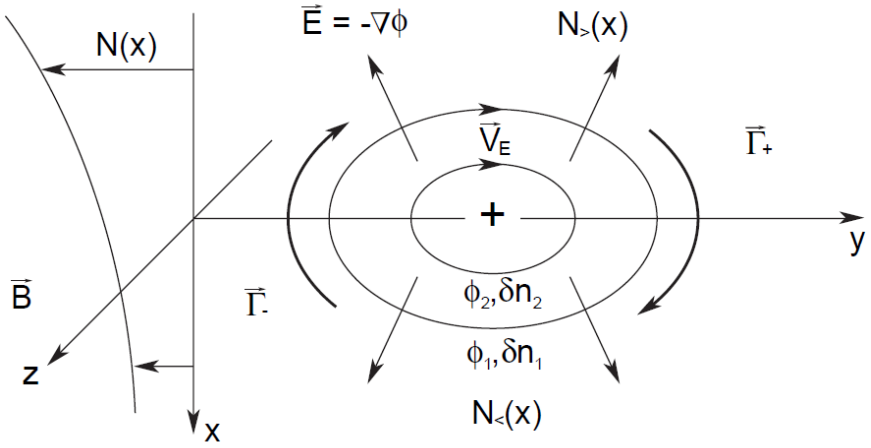

Figure 1-9 Drift wave mechanism showing E × B convection [23]

However, in more general situations, the electron density fluctuation is not in phase with the potential fluctuation such as in the case with consideration of finite dissipation of parallel electron momentum. Transport associated with the "non-adiabatic" behavior of the electrons is usually called anomalous transport. Due to the phase shift of the density from the potential, the time-averaged product of the

fluctuating density and E × B velocity does not vanish and will lead to a net particle transport moving down the density gradient. The Figure 1-10 illustrates the development of a turbulent particle flux in the collisional plasma.

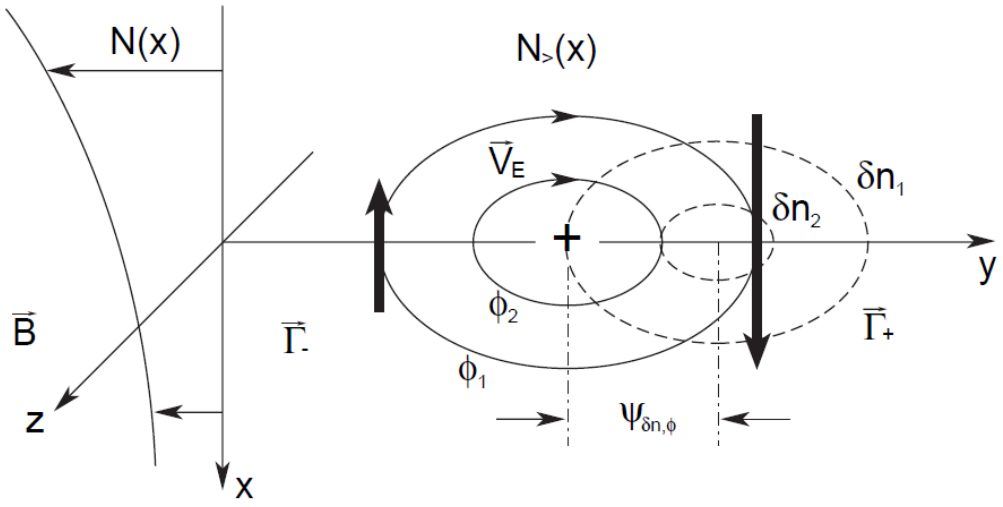

Figure 1-10 The general case where the drift wave density fluctuations are shifted in phase from the potential fluctuations. This results in a net flux of density down the density gradient when the particle flux is integrated over a fixed radial surface. [23]

When calculating the time-averaged cross-field flux Γ, which has the following expression:

$$\langle \tilde{n}\tilde{V} \rangle = \langle \tilde{n}\tilde{E} \rangle / B_0 \tag{1.22}$$

Where $\tilde{n}$ and $\tilde{E}$are the fluctuating density and electric field separately. B_0denotes the static magnetic field and $\langle \cdots \rangle$ denotes averaging by time. In cylindrical geometry like

our machine, we can make associations with $\tilde{V} \sim \tilde{V}_r$, $\tilde{E} \sim \tilde{E}_\theta$, and $B_0 \sim B_{0z}$. To rewritten Eqn. (1.17) in the spectral domain, we use the fast Fourier transform method (will be introduced in next Chapter) to represent density and potential fluctuations and assume $\tilde{E} = -\nabla\tilde{\phi}$:

$$\tilde{n}(\boldsymbol{r}, t) = \int_{-\infty}^{\infty} N_0(\omega) e^{-i(\boldsymbol{k}(\omega)\cdot\boldsymbol{r}-\omega t)} d\omega \tag{1.23}$$

$$\tilde{\phi}(\boldsymbol{r}, t) = \int_{-\infty}^{\infty} \phi_0(\omega) e^{-i(\boldsymbol{k}(\omega)\cdot\boldsymbol{r}-\omega t)} d\omega \tag{1.24}$$

$$\tilde{E}(\boldsymbol{r}, t) = -\nabla\tilde{\phi}(\boldsymbol{r}, t) = \int_{-\infty}^{\infty} -i\boldsymbol{k}(\omega)\phi_0(\omega) e^{i(\boldsymbol{k}(\omega)\cdot\boldsymbol{r}-\omega t)} d\omega \tag{1.25}$$

The new turbulent particle flux becomes: [24]

$$\Gamma_{turb} = <\tilde{n}\tilde{V}_r> = \frac{<\tilde{n}\tilde{E}_\theta>}{B_z} = \frac{2}{B}\int_0^{\infty} k_\theta(\omega)\left|P_{n\phi}(\omega)\right|\sin[\theta_{n,\phi}(\omega)]d\omega \tag{1.26}$$

where k_θ is the poloidal wave number of fluctuations, $P_{n\varphi}(\omega)$ is equal to the cross-power spectrum between density and potential fluctuations, $\theta_{n,\phi}$ is the phase of the potential fluctuations minus the phase of the density fluctuations. Multiplying and dividing Eqn. (1.21) by $\left[P_{nn}(\omega)P_{\phi\phi}(\omega)\right]^{1/2}$:

$$\Gamma_{turb} = <\tilde{n}\tilde{V}_r> = \frac{<\tilde{n}\tilde{E}_\theta>}{B_z}$$

$$= \frac{2}{B}\int_0^\infty k_\theta(\omega)\left|\gamma_{n\phi}(\omega)\right|\sin\left[\theta_{n,\phi}(\omega)\right]\left[P_{nn}(\omega)P_{\phi\phi}(\omega)\right]^{\frac{1}{2}}d\omega \quad (1.27)$$

Here $\left|\gamma_{n\phi}(\omega)\right|$ denotes the coherence between the density and potential fluctuations with a value between 0 and 1, which equals to $\frac{S_{n,\phi}}{\sqrt{S_{n,n}S_{\phi,\phi}}}$. Eqn. (1.22) reveals that there are three main components that will modify the turbulent particle flux: (1) turbulence amplitude, the auto power densities of the fluctuations ($P_{nn}(\omega)$, $P_{\phi\phi}(\omega)$); (2) coherence of density and potential fluctuations; (3) the cross-phase $\theta_{n,\phi}$.

1.3.2 Experimental observations of inward particle flux

Up-gradient, inward transport processes play a critical role in maintaining non-equilibrium conditions across a wide-range of systems in many physics fields. For example, in biophysics eukaryote cells transport of Na+/K+ ions across the cell membrane occurs via the active transport mechanism in which the hydrolysis of the ATPASE molecule releases chemical potential energy, which then allows work to be done on the Na+/K+ ions thereby moving them across the membrane and up their concentration gradient [25]. Similar mechanisms govern the transport of molecules (e.g. glucose) critical to metabolism as well. In open fluid thermodynamic systems that are driven out of equilibrium by heat input, up-gradient transport can occur as in e.g.

the convective planetary boundary layer [26] and in carefully constructed experimental systems [27].

In magnetically confined plasmas, up-gradient transport mechanisms have been invoked to explain the observed time-averaged plasma density and temperature profiles in astrophysical and near-Earth space plasmas [28-32] and in controlled fusion confinement experiments [22,33-37]. Theory usually attributes such transport fluxes to the combined effects of density and temperature gradients, acting to give rise to a turbulent pinch which counteracts the normal down-gradient diffusive transport that is also thought to be operative.

Inward turbulent particle flux has been observed on different plasma devices [38-41]. It could be responsible for sustaining high confinement in controlled fusion experiments. For fusion systems, inferred transport fluxes are often decomposed into a turbulent pinch and down-gradient diffusive transport components [22],

$$\Gamma_{turb} = -D\nabla n + V_{pinch} n \tag{1.28}$$

where n is the mean density profile, D is the diffusive coefficient and V_{pinch} is the pinch velocity. The first diffusive term is the anomalous particle flux introduced in Chap 1.3.1, which will lead an outward particle transport going down the density gradient. The second term is the convective flux. In quasilinear theory, the pinch, which has in the past been attributed to the temperature and density gradients, can yield an inward flux component that then partially counteracts the outward diffusive transport.

In a few cases, direct measurements of net inward turbulent particle fluxes have been reported during or shortly after the formation of transport barriers associated with the formation of a suitably strong **E**×**B** shear layer or during the application of an externally forced **E**×**B** shear flow. On DIII-D tokamak, inward particle transport has been observed during the Low-to-High confinement (L-H) transition in ECH heated helium plasma [38]. Experiments were performed by using plunging probe into an evolving ELM-free H-mode. The basic parameters were $n_0 = 3.2 \times 10^{19} m^{-3}$, $I_p = 1.3\ MA$, and $B_{\varphi 0} = -1.8T$. The integral form of the particle continuity equation is shown as [38],

$$\partial_t \langle N \rangle(\psi) + \oint_{\partial \mathrm{V}} d^2\sigma \cdot \langle \Gamma \rangle = \int_{\partial \mathrm{V}} d^3x \langle S_n \rangle \tag{1.29}$$

where the first term is the total particle number enclosed in a volume V. The second term, which approximately equals to $2\pi R L_{eff} \langle \tilde{n} \tilde{v}_p \rangle$, is the transport term showing the particle numbers that been transported out of (or into) the volume V. The turbulent particle flux profile is shown in Figure 1-11(b). For $\psi \lesssim 0.99$, the particle transport is directed inward. While for $\psi > 1.01$, it is directed outward. As we can see from Figure 1-11(a), the time-averaged density profiles are peaked and the gradient becomes steepened after L-H transition. It is believed that the inward particle transport is somehow related to the pedestal formation.

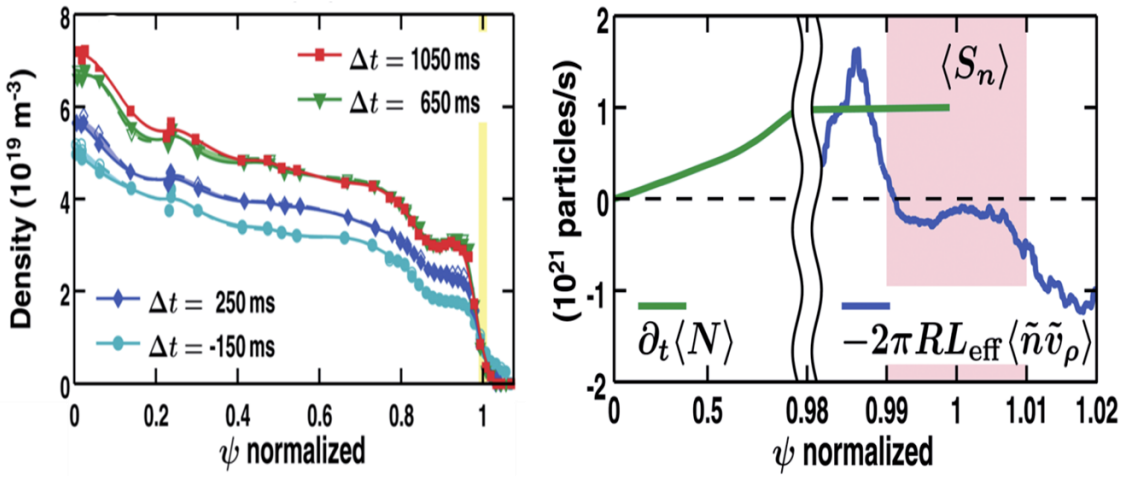

Figure 1-11 (a) Density profile evolution in ECH heated plasmas. (b) The measured profile of the turbulent particle transport $\langle \tilde{n}\tilde{v}_\rho \rangle$, extrapolated to the whole flux surface, and a main ionization source $\langle S_n \rangle$ in the region of $0.99 \lesssim \psi \lesssim 1.01$. [38]

Direct observation of inward particle flux during L-H transition is also obtained in H-1 stellarator [41]. The H-1 stellarator is a flexible heliac configuration and, for the experiments reported here, was operated in a shearless magnetic configuration with B = 0.05 - 0.15 T, and a radio frequency heating power of up to 100 kW at the frequency of 7 MHz. Central electron density is about 10^{18} m^{-3}, the electron temperature in argon discharges is in the range from 8 to 20 eV, and the ion temperature is about 40–50 eV in the low confinement mode. The transition to improved confinement leads to the significant increase in the electron density over a significant portion of the plasma radius, as shown in Figure 1-12(a) and to the reversal of the fluctuation-induced particle transport shown in Figure 1-12(b). Negative values

of fluctuation-induced particle flux Γ_{fl} correspond to outwardly directed particle flux. As we can see, after the transition the sign of Γ_{fl} changes to positive, indicating inwardly directed flux.

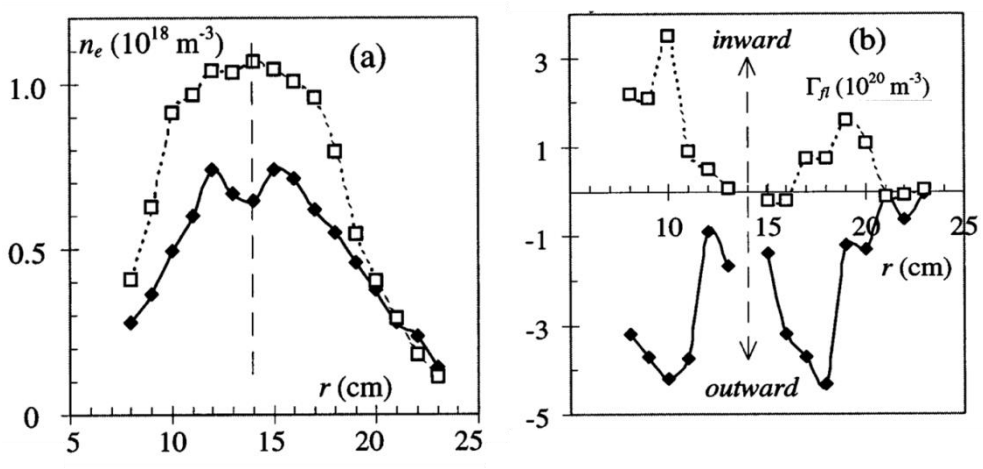

Figure 1-12 (a) the fluctuation-induced particle flux (b) before (diamonds) and after (squares) the transition from low to the fluctuating high confinement mode. (Right panel) [41]

Recently this inward turbulent particle flux has also been observed in the linear machine (LAPD [42]) when a strong externally applied E×B shear flow was induced. The experiments were performed in the upgraded Large Plasma Device (LAPD). Flows are driven through biasing the vacuum chamber wall relative to the plasma source. By increasing bias to above ~ 100V, they found the density gradient scale length decrease significantly indicating a transition in radial particle confinement [43]. Figure 1-13(a) shows the radial profile of azimuthal flow velocity for several bias values. Azimuthal flow is driven at the edge of LAPD. As the bias is increased beyond

threshold (100V), a strong flow shear develops and increases with bias value. Figure 1-13(b) shows the radial profile of turbulent particle flux for four different bias voltages. It is observed that below threshold (~110V) the turbulent particle flux is reduced with bias voltages. As the bias in further increased to 175V, a reversal in the measured particle flux is observed which indicates the particles transport inward.

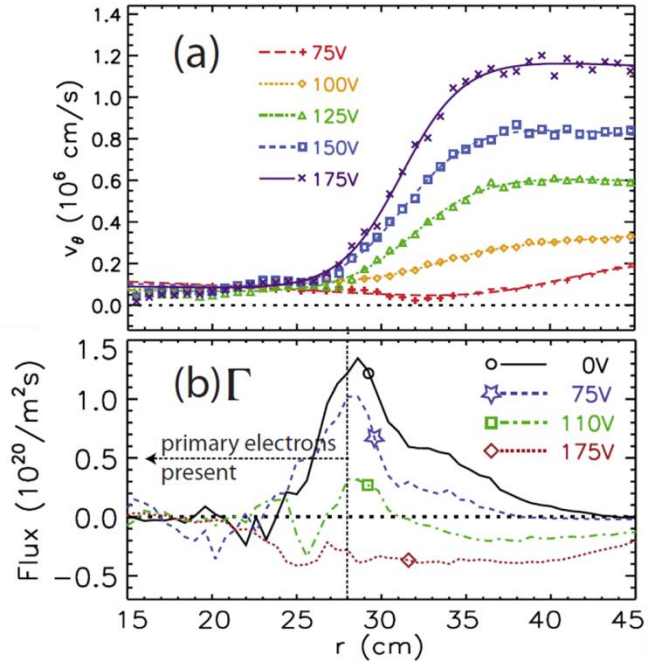

Figure 1-13 For several bias values: (a) Radial profile of azimuthal velocity, with fit. (b) Radial profile of turbulent particle flux. [43]

There are many other different plasma devices reporting the observations of inward particle flux, including TORPEX [44], a simple toroidal plasma device, and PANTA [45], a linear helicon plasma device and so on. However, the origin of the net

inward flux in these works has not been identified and the key role that velocity shear plays in driving such inward pinches has not been addressed.

1.4 The aim of this dissertation

Previous studies on CSDX have shown that at moderate magnetic fields the plasma develops coherent, finite amplitude collisional drift wave fluctuations in the region around the density gradient maximum. As the magnetic field is increased further, the plasma develops two velocity shear layers that sit on either side of the density gradient maximum [21,46]. At the outer shear layer the turbulent stress does work on and sustains the shear flow against dissipation, consistent with earlier results [47-51] and under some conditions, in the region between the maximum density gradient and outer shear layer, a net inward flux is observed [21].

Based on the limitations of the existing experimental results and our previous work on Controlled Shear Decorrelation Experiment (CSDX) we perform this study on upgraded CSDX (CSDX-U) through three primary avenues: The first avenue is to directly investigate statistical properties of fluctuation-induced particle flux in CSDX-U using fast imaging and Langmuir probes diagnostics, giving a more complementary experimental picture of the development of an inward particle flux. The high correlation between probe signal and light intensity signal and the low plasma temperature allow us to compare the results using these two independent diagnostics. The two independent diagnostic techniques see the development of an inward particle flux and the mean density gradient steepens in response to this inward flux. Also we

take a further look into intermittent turbulent structure dynamics by using a conditional averaging method.

It is particularly remarkable that these observations are made in a simple plasma system described by the Hasegawa-Wakatani model of the drift wave turbulence-zonal flow system. At the outset of this work there were only two known free energy sources in this experiment. The first one is the mean density gradient, which will give rise to a diffusive particle transport down the gradient. The other one is the strong velocity gradient. Thus the obvious question arises: what is the underlying physics mechanism for the net inward particle transport.

This question leads to the second avenue of the dissertation. Time-domain and bispectral Fourier domain analysis shows that at the peak of the shear layer, where the particle flux is outward the turbulent stress acts to nonlinearly reinforce the shear flow. Between the shear layer and the peak density gradient, the azimuthal flow nonlinearly drives the fluctuations which give rise to the inward particle flux. Correlation studies show that a transient increase (decrease) in the shear flow results in a subsequent increase (decrease) in the inward flux, demonstrating the causal relationship between flow shear and up-gradient flux. Finally, when the up-gradient flux occurs the time-averaged density profile steepens. Clearly then drift turbulence not only can generate a sheared flow that acts to regulate the rate of cross-field transport [52], but under some conditions the shear flow can be a source of turbulence that surprisingly can cause an up-gradient particle flux that enhances the density gradient, thereby forming a new feedback loop in the regulation of time-averaged density and velocity gradients by the coupled drift turbulence-sheared flow system.

These results then lead to the next question: Can we reproduce the similar experimental findings with simple linear studies. This then leads to the third avenue of the dissertation. By doing linear instability analysis and a simple eigenvalue study, we find that a simple 2-field modified Hasegawa-Watani model cannot produce an inward flux, which suggests that there is some other mechanism other than flow shear that are acting as a driving source. And we summarized the recent studies of possible mechanism for inward flux.

This thesis is organized as follows: In chapter 2 we describe the basic experimental setup for CSDX-U, hardware arrangements and summarize the various analysis methods we use for this study. In chapter 3 the identification of the up-gradient inward particle flux using a combination of probe based measurements and fast-framing camera is extensively discussed. In chapter 4 we discuss the possible link between flow and inward flux. In chapter 5 we test our hypothesis from experimental results with linear stabilities analyses. Lastly in chapter 6 we summarize our results and suggest several recommendations for the future work.

Chapter 2

Experimental set up and methods of analysis

In this chapter we will describe the basic mechanical and electrical hardware used in our experiments, and give an overview of the various methods utilized for our data analysis.

2.1 CSDX linear plasma machine

Controlled Shear Decorrelation Experiment (CSDX) is a cylindrical magnetized linear plasma device as shown in Figure 2-1. The total length is 2.8m and the vacuum vessel diameter is 0.2m. A uniform magnetic field is generated by 28 solenoidal current coils. The field lines terminate on insulated plates on both ends of the machine, which ensure that there is no current running through the end plates. Previous studies have shown that the transition to drift wave turbulence and the formation of low frequency zonal flows can be either suppressed with conducting boundaries or enhanced with insulating boundaries [53]. This device is operated with a 13.56MHz 5 kW RF helicon wave source. A digitizer with up to 96 channels sampling at 500 kHz and anti-aliasing filters are used to record the data. The resulting Nyquist frequency is 250 kHz, well above the observed fluctuation frequency. A RF matching

circuit is adjusted such that less than 30 W of power is observed reflected. A more detailed description of the RF source characteristics can be found in Ref. [54]. A calibrated MKS mass flow controller is used to introduce the working gases at the first port available downstream of the antenna (see figure 2-1). The effective pressure in the chamber can also be controlled by a manually operated butterfly valve located in front of the turbomolecular pump. The chamber pressure is measured by two Baratron gauges, one located at the port of the gas feed and the other located just in front of the butterfly valve at the end of the chamber. Plasmas are typically created at neutral pressures of 1 to 10mTorr.

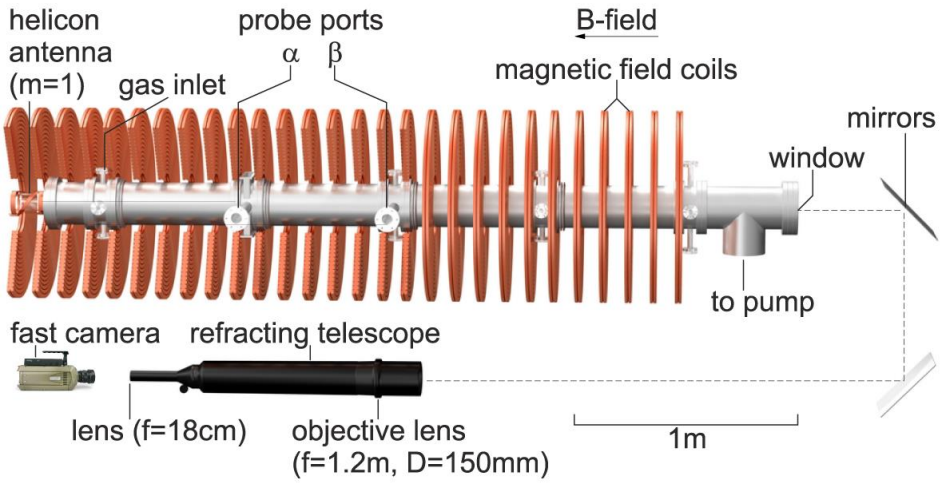

Figure 2-1 Schematic of the CSDX linear plasma device including setup of Langmuir probe and camera diagnostic. [21]

Figure 2-2 Picture of the Controlled Shear De-correlation Experiment.

2.2 Upgraded CSDX

The experiments were carried out in the Upgraded CSDX (CSDX-U). We upgraded CSDX in the following two aspects: one is we increased the source radius from the previous 5 cm value to a value of 7.5 cm and the other is we upgraded the power supply for achieving higher magnetic field. In addition, the antenna was changed from an azimuthally symmetric m=0 configuration to a helical m=1 antenna. The reasons come from both theoretic and experimental considerations. In the theory of gradient-driven instabilities such as collisional drift waves, the ratio $\frac{\rho_s}{L_n} = \frac{\sqrt{m_i T_e}}{(eB)L_n}$ is usually assumed to be small for a better comparison against Hasegawa-Wakatani

model. In previous experiments, the plasma the plasma diameter was ~10cm and the maximum magnetic field was ~1kG which made the ratio $\frac{\rho_s}{L_n} \sim 0.5$. While in our experiments on upgraded CSDX, the plasma size is ~ 15cm and the maximum magnetic field is 2.4kG which significantly decreased the $\frac{\rho_s}{L_n}$ by a factor of 4. Figure 2-3 show the comparison of time-averaged radial profiles between previous CSDX experiments (left panel; B = 1kG) and CSDX-U (right panel; B = 1.3kG) for: (a) time averaged density (b) gradient of the time-averaged density $-\partial\langle n\rangle/\partial r$ and (c) time-averaged azimuthal velocity. In previous experiments, the locations of the maximum density gradient and velocity shear gradient were very close to each other (< 1cm; see left panel [55]). A larger separation between the location of birth of vortex and the velocity shear would help to us to achieve a better understanding of interaction between turbulent eddies and shear flow. The time-averaged profiles of density and azimuthal velocity from the CSDX-U shown in (right panel) reveal a larger spatial separation between the two gradients ~ 3.5 cm. This then allows for a more detailed study of the interaction between density gradient driven and velocity shear driven turbulence dynamics.

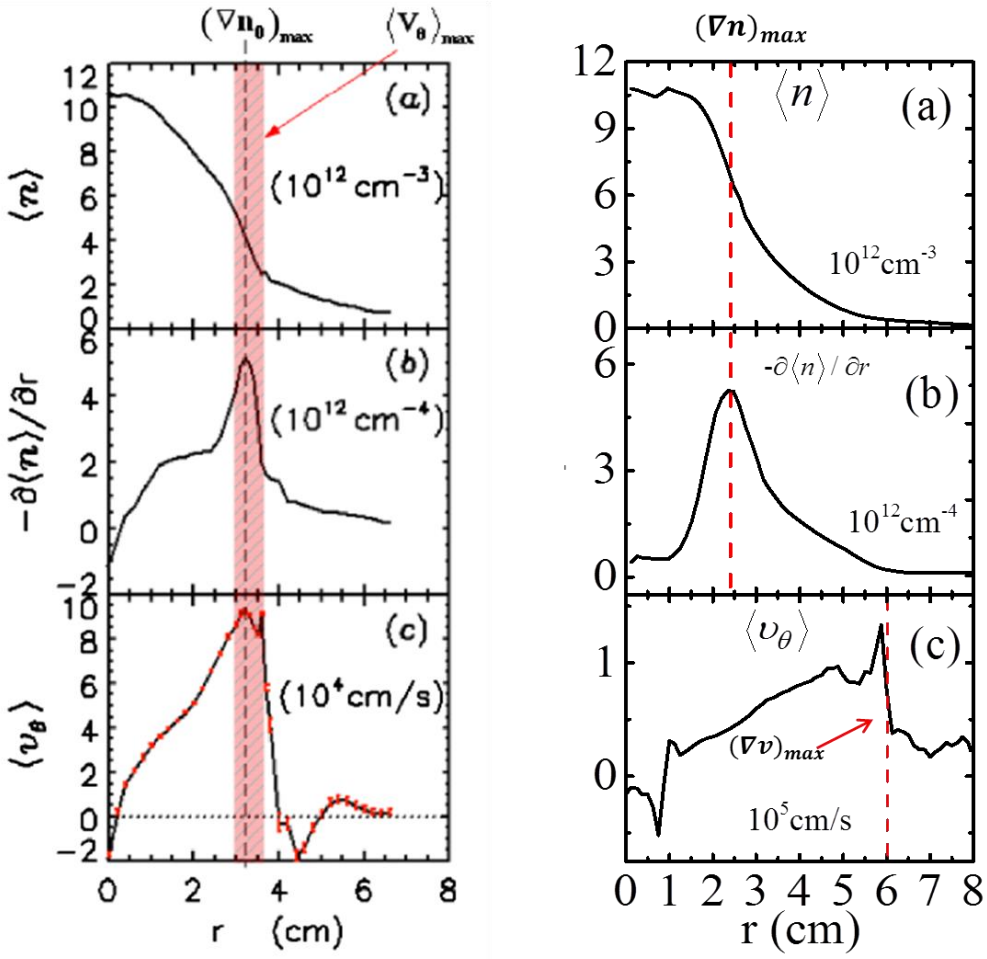

Figure 2-3 Comparison of time-averaged radial profiles between previous CSDX experiments (left panel; B = 1kG) and CSDX-U (right panel; B = 1.3kG). (a) Time averaged density $\langle \boldsymbol{n_0} \rangle$. (b) Gradient of the time-averaged density $-\frac{\partial \langle n \rangle}{\partial r}$. (c) Time-averaged azimuthal velocity $\langle \boldsymbol{v_\theta} \rangle$.

2.3 Plasma Diagnostics

2.3.1 The dual 3×3 Langmuir probe

The plasma produced is relatively cold and the moderate heat fluxes to the probes allow taking long sets of data for better statistics. Measurements of mean plasma profiles, the fluctuating density, potential, and electric fields along with the resulting turbulent particle flux are made by both an 18-tip Langmuir probe inserted radially in a port located ~1m downstream from the source (port α in Figure 2-1). The 18 tips are arranged as dual 3×3 arrays, which are shifted with respect to each other along the B field direction by 1.5 mm. The electrical circuit is shown in figure 2-5. The radial displacement of the probe tips is 1.5mm and the azimuthal displacement is 2.5mm. Each tungsten tip is 0.33mm in diameter and 1mm in length. One 3×3 array connecting to 100 kΩ resistor measures floating potential and the other array biased by −100 V DC voltage measures ion-saturation current. Detailed description about the 18-tip Langmuir probe can be found elsewhere [7,16].

In the absence of strong electron temperature fluctuations the floating potential fluctuations are interpreted as plasma potential fluctuations. Similarly, the measured ion saturation current fluctuations are interpreted as density fluctuations. Thus the arrangements of the probe tips in both radial and azimuthal directions allow the measurements of the electric field from floating potential by $\vec{E} = -\nabla\phi$. The 3×3 probe array also allows the measurements of bispectrum analysis, which will be introduced in next section.

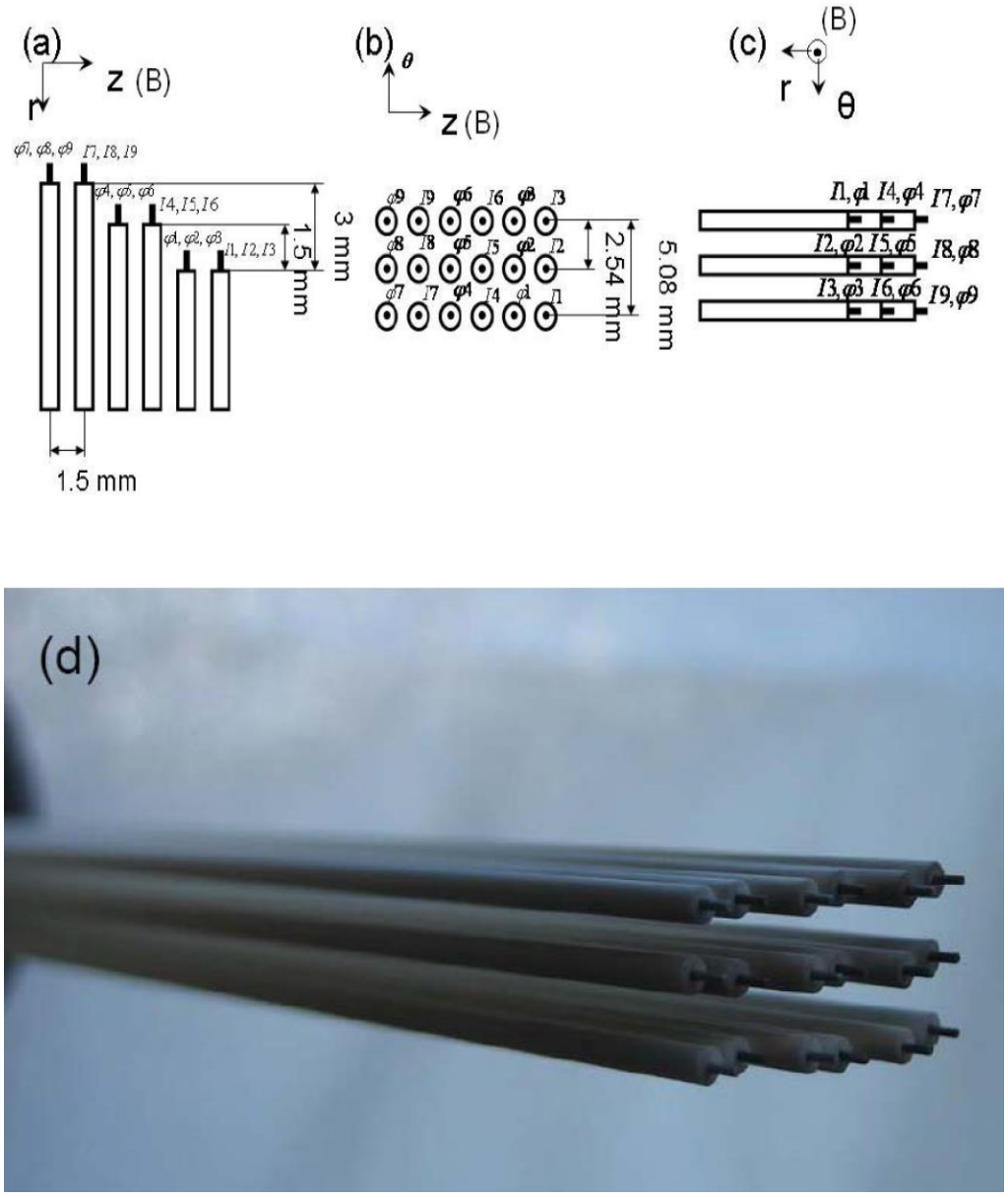

Figure 2-4 Dual 3x3 Langmiur probe array, of which one 3x3 array (9 channels) is for floating potential and anther 3x3 array is for ion saturation current (or density). These two arrays shift in the axial direction by 1.5 mm [7,16].

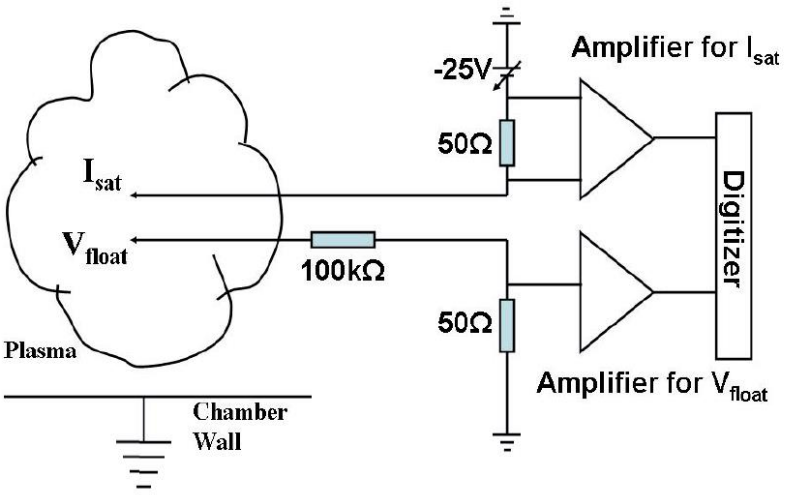

Figure 2-5 A circuit schematic of density and potential measurements. [7]

2.3.2 The 4-tip turbulent Reynolds stress Langmuir probe

To confirm the observation of inward particle flux is independent of probe configurations and probe location, we used a fast scanning we used a fast scanning 4-tip Reynolds stress probe array located 1.7m downstream from the source (port β in figure 2-1) for turbulent particle flux measurement, shown in figure 2-6. One of the 3 short tips is for ion saturation current and the rest (two short tips and one long tip) are for floating potential. Both two probes have shown similar experimental results.

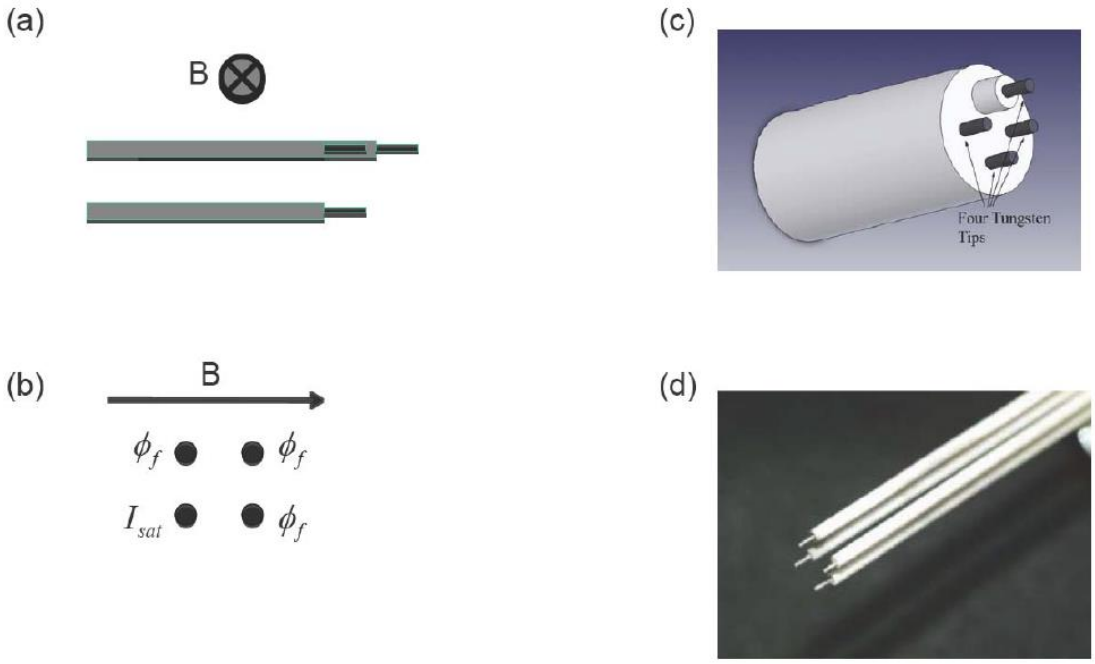

Figure 2-6 The 4-tip turbulent flux probe array. (a) and (b) shows the position relative to the magnetic field line. (c) is a 3D sketch and (d) is a picture of the Langmiur probe array. One of the 3 short tips is for ion saturation current, and the rest (two short tips and one long tip) are for floating potential, as indicated in (b). [16]

Figure 2-7 shows the radial profiles of equilibrium density and turbulent particle flux from two Langmuir probes. The two probe measurements show the similar behavior that the density gets steepened and the particle transport changes from outward to inward as we increase magnetic field. Later on, results shown in this dissertation are mainly from 18-tip probe, since we can gain the bispectral from 18 tips.

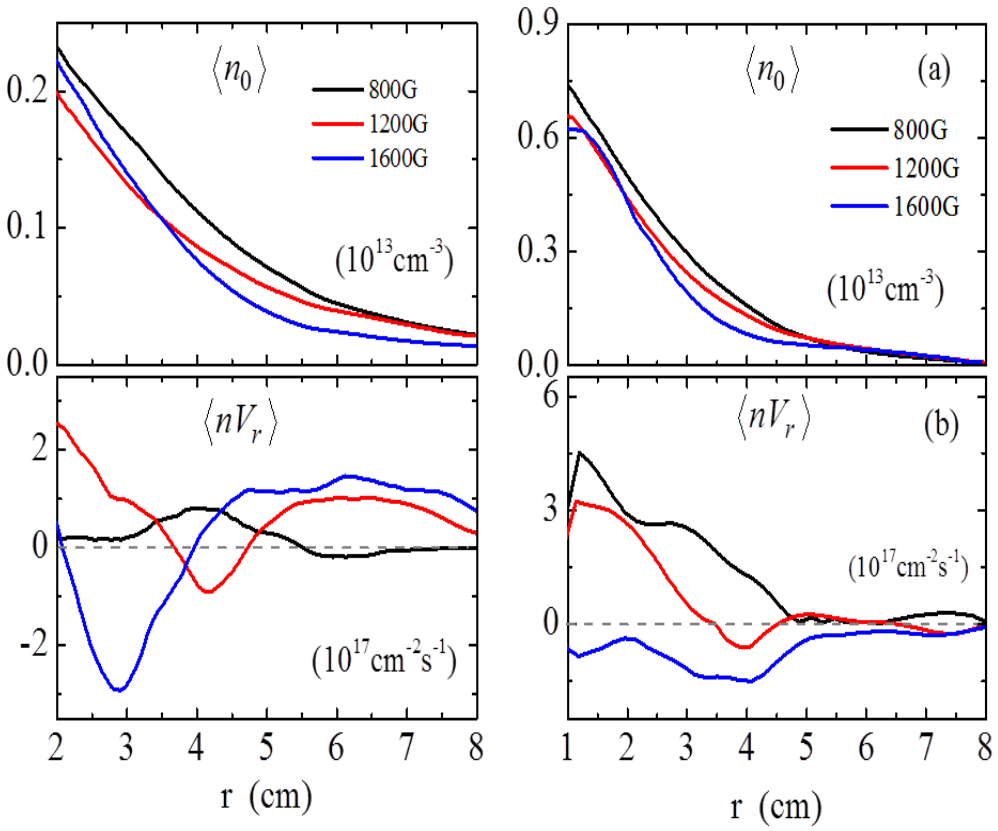

Figure 2-7 Comparison between 18-tip probe (left panel) and 4-tip probe (right panel). Radial profiles of (a) mean density (b) turbulent particle flux.

2.3.3 Mach probe

In addition, a 4-tip Mach probe is used to measure the parallel flow velocity shown in Figure 2-8. The two sets of tips, placed symmetrically around the probe axis separated by insulators, one of which are biased negatively to collect ion saturation currents and the other set are measuring the floating potential.

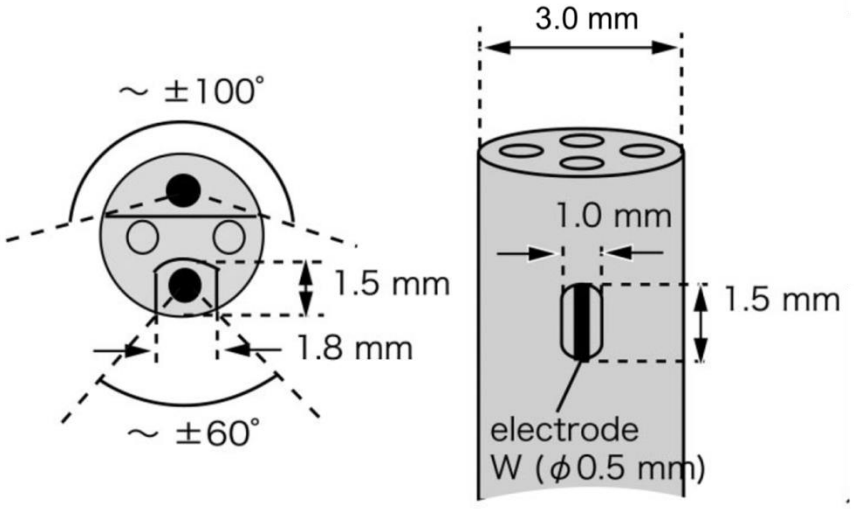

Figure 2-8 Schematic view of Mach probe.

The flows are interpreted based on j_M, the ratio of the ion saturation currents collected by 180° opposite probe tips. The measurements are then fitted to the equation [56]:

$$j_M = \frac{I_{sat1}}{I_{sat2}} = \exp[(K \sin(\delta\alpha)/\delta\alpha) M_{\parallel} \cos\theta] \tag{2.1}$$

$$V_z = M_{\parallel} * C_s \tag{2.2}$$

where δα is the acceptance angle of each probe tip (~0.532 in our probe design), K = 1.34, (using Hutchinson's model of ion collection [57]) and θ is the angle between the probe normal direction and the downstream direction (90^o in our experiments). By measuring I_{sat1} and I_{sat2} from Mach probe, we can calculate $M_{\parallel}$ according to Eqn. (2.1). Thus we can get the parallel flow velocity V_z. Figure 2-9 shows the evolution of the radial profiles of the parallel ion fluid velocity measured by Mach probe. Positive V_z represents plasma flowing away from source In the parallel direction the V_z profiles show that the inner plasma flows away from the source toward the pump end of the machine while it seems to reverse direction at the edge.

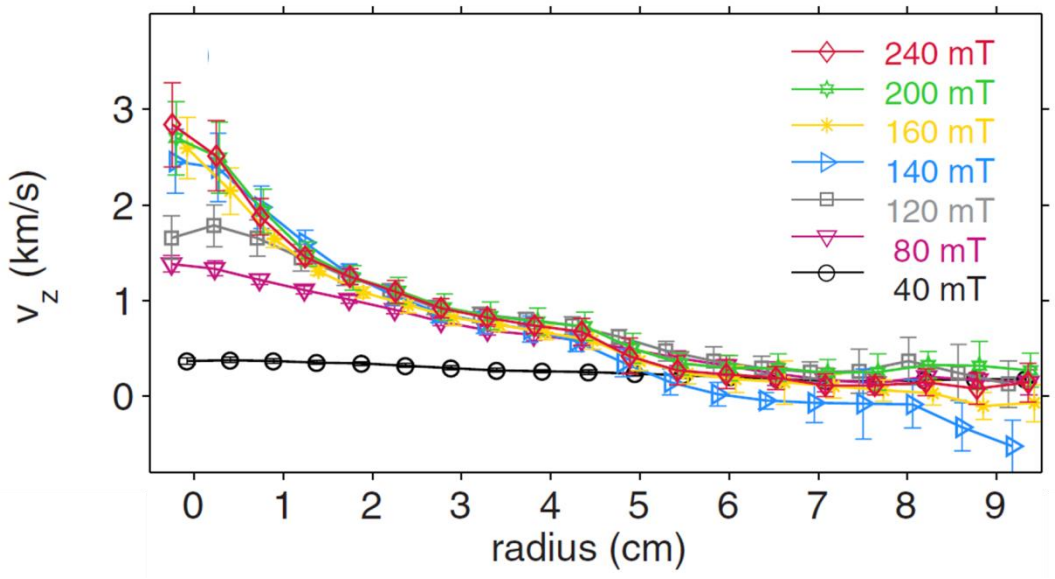

Figure 2-9 Evolution of parallel flow velocity measured by Mach probe. [21]

2.3.4 Data acquisition system

For the density measurements the voltage across the 50 Ω resistor passes through an AC coupled amplifier, which has 50 Ω input impedance and 1MHz band width, and is recorded by a 16 bit 96 channel digitizer with 500 kHz sampling rate (D-TACQ ACQ196CPCI). The resulting Nyquist frequency is 250 kHz well above the electrostatic fluctuation frequency. For equilibrium density measurements the voltage across the 50 Ω resistor passes through a DC-coupled differential amplifier (Lecroy DA1855A-PR2) and connects to the digitizer which has 1M Ω input impedance (a 50 Ω resistor is parallel to the digitizer for impedance match). For the floating potential measurements the voltage passes through a DC coupled amplifier (50 Ω input impedance and $\geq$ 2MHz band width) with a gain of A = ×28 for the high impedance output. A million samples (2sec) are usually obtained for the fluctuation data at each radial location, allowing for low-variance estimation of the fluctuation statistics. [7]

2.3.5 Laser induced fluorescence

Laser induced fluorescence (LIF) is employed in our experiments to measure Doppler resolved velocity distribution functions (VDF). The full width at half maxima of the VDF gives us the average temperature of the distribution and the shift of the peak of the distribution from a standard reference line gives the ion fluid velocity, from which we can calculate the relatively accurate velocity. In our experiments, we use LIF on argon ions to measure radial profiles of the azimuthal $\mathbf{E} \times \mathbf{B}$ velocity, the ion temperature of CSDX plasma and also the parallel flow velocity.

The LIF set used for our experiment is shown in Figure 2-10, where 1 is the wavemeter, 2. laser beam steering optics, 3. laser beam injection mirror, 4. plasma chamber, 5. LIF volume, 6. laser beam dump, 7. collection optics, 8. interference filter, 9. photo-multiplier tube (PMT), 10. Toptica laser, 11. mechanical chopper, 12. laser controller, 13. lock-in amplifier, 14. data acquisition card, 15. laptop PC, 16. LIF signal (intensity vs. wavelength) for real time monitoring. Detailed description for LIF diagnostics can be found in Ref. [58].

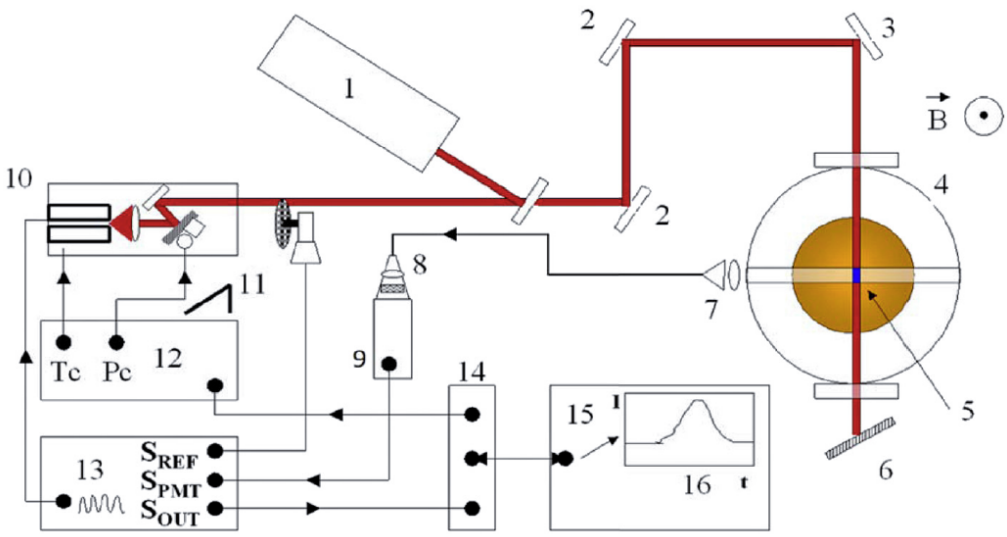

Figure 2-10 Schematic of the LIF setup on CSDX. [58]

2.3.6 High-speed imaging diagnostics

Langmiur probe arrays mentioned above can offer high temporally resolved signals but for the spatial resolution is inadequate to track the 2-dimensional turbulent evolution. In addition, high-speed imaging data provides a better comparison to probe data due to the possibility of temperature fluctuations and other complications in probe data interpretation. For imaging the dynamics in the azimuthal cross-section of the plasma column we use a fast framing camera to record the light intensity. A Phantom V 710 high speed camera is placed at the end of the machine to capture the motion of the plasma visible light emission. For this experiment, image sequences of 5000 frames were recorded at 210500 frames/s with an exposure time of 1 ~ 2 μs with 128×128 image resolution, and a Pentax 50 mm f / 1.4 lens is used in the experiments. The optical setup of the fast imaging system can be seen in Figure 2-1. Detailed description can be found in Ref. [7,16]. The light intensity fluctuations are considered to be proportional to the ion saturation current and thus a proxy for density fluctuations [59,60]. Visible light from the plasma is steered using two large mirrors on to a Celestron C6-RGT telescope placed about 7 meters away from the focal plane using a 180mm, f/4 lens as the objective. As recently discussed in detail elsewhere [61], detailed statistical properties and dispersion relations can be determined from the fast imaging data, and can be related to plasma instabilities thought to be operative in the experiment.

From basic spectroscopy studies in argon helicon plasma in CSDX, it is known that the light emitted is dominated by singly ionized argon (Ar II) emission in the

range 420–520 nm and neutral argon emission (Ar I) which is in the range 650–850 nm. Hence in this work we use commercially available filters to look at the ion emission (FWHM from 410–490 nm) and the neutral emission (long-pass filter for wavelength >650 nm) separately. We also used narrow-band filters (at 488 nm for Ar II and 750 nm for Ar I) in previous experiments [44] to collect only one dominant argon ion or neutral transition, but the collected light intensity was smaller and had to be integrated for a longer time to get any reliable measurement, thus reducing the time resolution. To calculate the light intensity fluctuations, we take the raw imaging data and subtract the mean average light intensity, thus we obtain the fluctuating light intensity for further calculation. Figure 2-11(a) shows a frame of raw movie data taken at 1300G, which we observe a strong mode of mean light intensity in the center region. By subtracting the mean average light intensity shown in Figure 2-11(b), we observe two kinds of turbulent structures; one is with high-mode numbers in the center and the other is with low-mode numbers in the outer region.

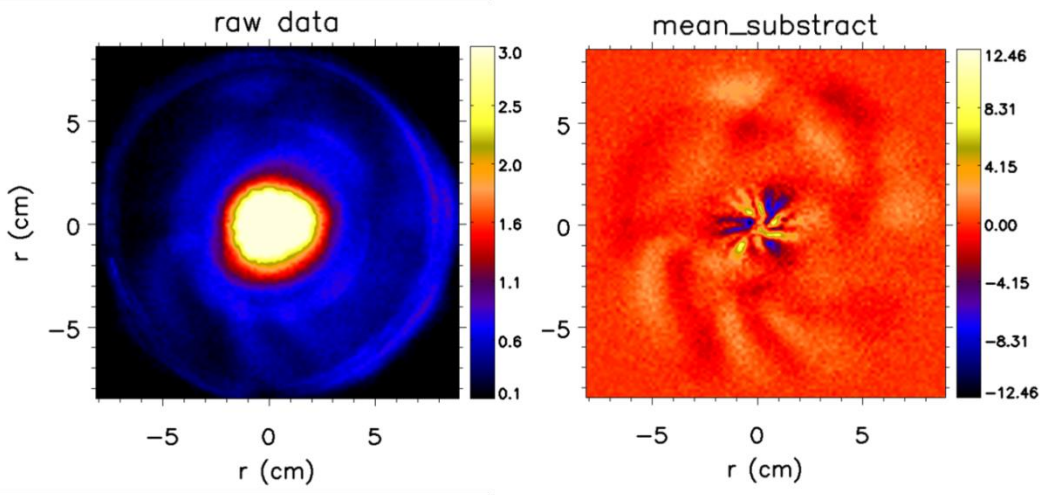

Figure 2-11 (a) raw imaging data (b) mean subtracted fluctuating light intensity

Figure 2-12(a) shows the raw ion saturation current fluctuations from Langmiur probe and light intensity fluctuations from fast imaging. In Figure 2-12(b), we plot the cross-correlation coefficient computed between the Langmuir probe ion saturation current I_{sat} and the camera fluctuating visible light intensity fluctuation I_c. The cross-correlation was calculated at r ~ 3 cm. The results show that $Corr(I_{sat}, I_c)$ reaches values as large as 0.75 with a zero delay time. The decay time of this cross-correlation is larger than 10ms reflecting a high correlation level for times much longer than turbulent correlation time or azimuthal rotation times. Thus the Langmiur probe and fast imaging signals also present very similar statistical properties, which also validate the interpretation of light intensity fluctuations as density fluctuations.

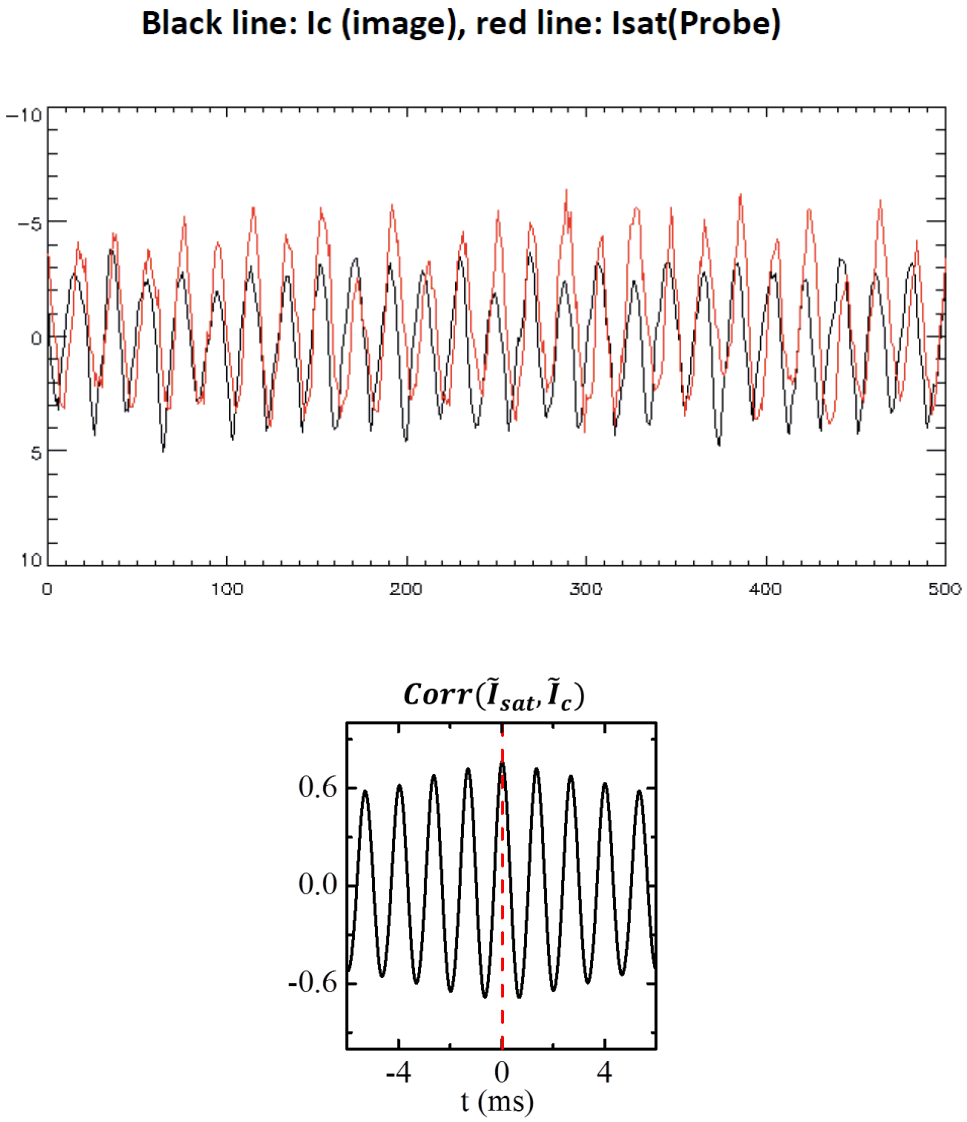

Figure 2-12 (a) Raw ion saturation current signal from Langmiur probe (black line) and light intensity fluctuation from fast imaging (red line) as a function of time. (b) Cross-correlation between ion saturation current and light intensity fluctuations.

2.4 Methods for data analysis

2.4.1 General statistical analysis techniques

Most turbulent fluctuations data such as density, potential and light intensity are suitable for statistical analysis. The main statistical analysis methods used in this dissertation include computing the auto-power spectrum $S_{xx}(f)$, cross-power spectrum $S_{xy}(f)$, cross-correlation $C_{xy}(f)$ and cross-phase $\alpha_{xy}(f)$. The definitions of the above quantities are described as below:

$$S_{xx}(f) = \langle X(f)X^*(f)\rangle \tag{2.3}$$

$$S_{xy}(f) = \langle X(f)Y^*(f)\rangle \tag{2.4}$$

$$C_{xy}(\tau) = \int_0^T x(t)y(t-\tau)dt \tag{2.5}$$

$$\alpha_{xy}(f) = \tan^{-1}[\mathrm{Im}(S_{xy}(f))/\mathrm{Re}(S_{xx}(f))] \tag{2.6}$$

where $X(f)$ and $Y(f)$ are the Fourier transform of time series $x(t)$ and $y(t)$ respectively, $\langle\cdots\rangle$ denotes the ensemble average and $*$ indicates the complex conjugate. τ is the time lag between $x(t)$ and $y(t)$. Here time series $x(t)$ and $y(t)$ can be the density or potential fluctuations that be measured from the Langmuir probe or fast camera.

Windowed FFT (Fast Fourier Transform) is used for computing spectra. In Fourier domain, the frequency resolution is determined by length of each window and limited by the sample rate. The total spectra in Eqn. (2.3) and (2.4) are the ensemble

average of all windows (denoting the number of windows with M). Suppose the total length of time series $x(t)$ is T seconds and we divide the T seconds into N windows. For each window the minimal frequency resolution is $\Delta f = 1/NT$ and the highest frequency can be resolved is the Nyquist frequency $f_{Nyq} = 1/2t_s$. Since the spectrum is an averaged value over N windows, the variance level will be a factor of $1/\sqrt{N}$ lower Therefore, Thus we can see that the windowed Fourier transform offers convergent spectrum with a lower noise level at the cost of frequency resolution.

In turbulence plasmas, many kinds of outstanding intermittent or transient phenomena have been observed to occur, such as transition to improved confinement, saw-tooth crashes, blob generation and so on. In our experiments, we find that the particle transport is dominated by intermittency when magnetic field is increased above to 1200G. Figure 2-13 shows the 50ms time series of density fluctuations at three different radial locations for B = 2400G [21]. Here for large magnetic fields, we observe the intermittent signals of density depletions near the center (r < 2 cm) shown in Figure 2-13(a) and intermittent bursts of enhanced density at the edge (r > 5 cm) shown in Figure 2-13(c). The evolution of such intermittent turbulent structure can be investigated by applying a conditional sampling analysis method, assuming that an average over many repeated condition of the phenomena of interest provides an explicit physical interpretation [62]. When the instantaneous fluctuating positive density excursion $\tilde{n}$ (often referred to as "blobs") exceeds one standard deviation σ_n at time τ, an event is considered to have been triggered. Meanwhile, a time window with length of $\Delta\tau$ (~ 64 microseconds, chosen to be larger than the typical turbulence

fluctuation correlation time, but smaller than the average time between events) is selected around τ, and the corresponding data associated with this positive fluctuating event is selected. This process is then repeated to yield a set of independent positive going density events fluctuations large enough to trigger the events will survive, while smaller amplitude fluctuations neighboring the event will then be averaged away. The same technique was performed for the negative fluctuation events (negative density excursions, or "holes") with a trigger of one negative standard deviation $-\sigma_n$.

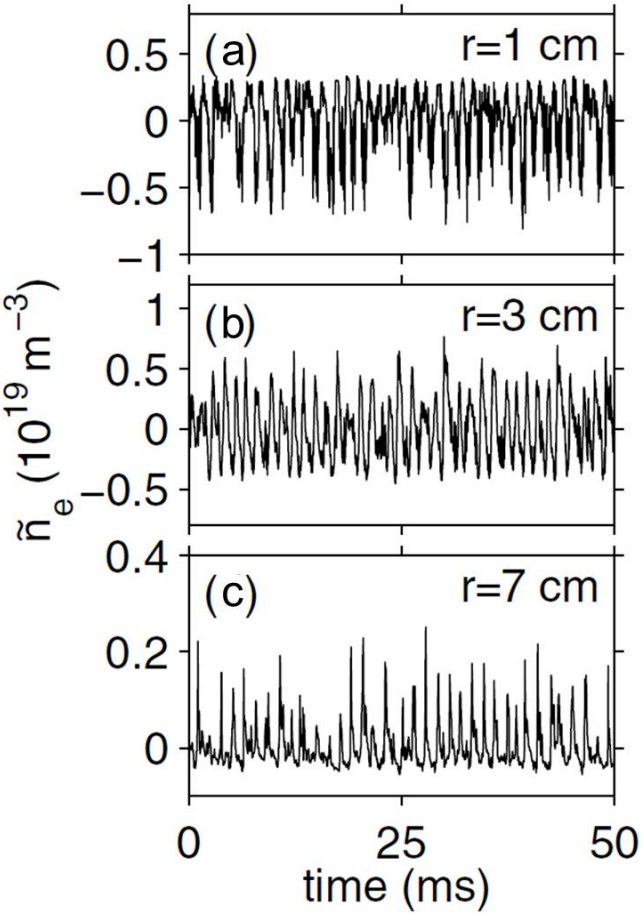

Figure 2-13 Time series of density fluctuations at three different radial locations for B = 2400G. [21]

2.4.2 Bispectral analysis

Bispectral statistics are Fourier transforms of a triple-point correlation that is similar to the power spectrum obtained from two-point correlation. We define the auto-bispectrum $S_f(f_1, f_2)$ of a signal $X(f)$ as follows,

$$S_f(f_1, f_2) = \langle X(f)X^*(f_1)X^*(f_2)\rangle = \frac{1}{M}\sum_{i=1}^{M}[X(f)X^*(f_1)X^*(f_2)] \tag{2.7}$$

here i indicates the i^{th}window. The bicoherence $b_f(f_1, f_2)$ is defined as,

$$b_f(f_1, f_2) = \frac{|X(f)X^*(f_1)X^*(f_2)|}{\sqrt{\langle|X(f)|^2\rangle}\sqrt{\langle|X(f_1)X(f_2)|^2\rangle}} \tag{2.8}$$

We note that f should satisfy the matching condition: $f = f_1 + f_2$.

In a 3-wave interaction discussed in Chap 1.2.2, two small scaled waves nonlinear coupling with each other will give rise to a third, large scale wave. The above second order spectral analysis techniques methods generally characterize the linear properties of these waves but way nothing about these important nonlinear processes. For study of nonlinear processes involved, we use bispectral analysis techniques in the frequency domain described by two fields, density and potential. By performing a Fourier transform on the ion momentum equation Eqn. (1.8), we obtain

$$\begin{aligned}\left\langle \frac{1}{2}\frac{\partial\left|\nabla_{\perp}\phi_f\right|^2}{\partial t}\right\rangle &= \left\langle -Re\sum_{f_1}\left(\hat{z}\times\nabla_{\perp}\phi_f^*\right)\cdot\left[\left(\hat{z}\times\nabla_{\perp}\phi_{f-f_1}\cdot\nabla_{\perp}\right)\left(\hat{z}\times\nabla_{\perp}\phi_{f_1}\right)\right]\right\rangle \\ &+ \left\langle \frac{\mu_{\perp}}{\Omega_{ci}\rho_s^2}Re\left[\left(\hat{z}\times\nabla_{\perp}\phi_f^*\right)\cdot\nabla_{\perp}^2\left(\hat{z}\times\nabla_{\perp}\phi_f\right)\right]\right\rangle \\ &+ \left\langle -\frac{\nu_{i-n}}{\Omega_{ci}}\left|\nabla_{\perp}\phi_f\right|^2\right\rangle,\end{aligned} \tag{2.9}$$

where $f = f_1 + f_2$,flow velocity is approximated by $\boldsymbol{u} \approx -\frac{\nabla_{\perp}\phi\times\boldsymbol{B}}{B^2}$, $\mu_{\perp}$ is the ion viscosity and ν_{i-n} is the ion-neutral collision rate. The LHS term is the rate of change in the $\mathbf{E}\times\mathbf{B}$ velocity fluctuation energy at one radius. The first term on RHS is called the kinetic energy transfer term T_u, which determines how much energy is nonlinearly transferred into or out of the frequency f. The second term on RHS shows the rate of energy being damped due to ion viscosity. The third term on RHS is the flow damping term due to ion-neutral collisions.

Expanding Eqn. (2.9) for a cylindrical plasma with uniform magnetic field in z direction, the kinetic energy transfer term T_u can be rewritten as [63]:

$$T_u = \langle -Re \sum_{f_1} \left(\hat{z} \times \nabla_\perp \phi_f^*\right) \cdot \left[\left(\hat{z} \times \nabla_\perp \phi_{f-f_1} \cdot \nabla_\perp\right)\left(\hat{z} \times \nabla_\perp \phi_{f_1}\right)\right] \rangle$$

$$\approx \langle Re \sum \left[\frac{\partial \phi_f^*}{\partial x} \frac{\partial \phi_{f-f_1}}{\partial y} \frac{\partial^2 \phi_{f_1}}{\partial x^2} - \frac{\partial \phi_f^*}{\partial x} \frac{\partial \phi_{f-f_1}}{\partial x} \frac{\partial^2 \phi_{f_1}}{\partial x \partial y} \right. \tag{2.10}$$

$$\left. + \frac{\partial \phi_f^*}{\partial y} \frac{\partial \phi_{f-f_1}}{\partial y} \frac{\partial^2 \phi_{f_1}}{\partial x \partial y} - \frac{\partial \phi_f^*}{\partial y} \frac{\partial \phi_{f-f_1}}{\partial x} \frac{\partial^2 \phi_{f_1}}{\partial y^2} \right] \rangle$$

where x and y denote radial and azimuthal direction respectively. By splitting Eqn. (2.10) into parts, we can obtain four different three-field cross bispectral terms defined in Eqn. (2.7):$\sum_{f_1} \left[\frac{\partial \phi_f^*}{\partial x} \frac{\partial \phi_{f-f_1}}{\partial y} \frac{\partial^2 \phi_{f_1}}{\partial x^2} \right]$, $\sum_{f_1} \left[\frac{\partial \phi_f^*}{\partial x} \frac{\partial \phi_{f-f_1}}{\partial x} \frac{\partial^2 \phi_{f_1}}{\partial x \partial y} \right]$, $\sum_{f_1} \left[\frac{\partial \phi_f^*}{\partial y} \frac{\partial \phi_{f-f_1}}{\partial y} \frac{\partial^2 \phi_{f_1}}{\partial x \partial y} \right]$ and $\sum_{f_1} \left[\frac{\partial \phi_f^*}{\partial y} \frac{\partial \phi_{f-f_1}}{\partial x} \frac{\partial^2 \phi_{f_1}}{\partial y^2} \right]$. The bispectral terms determine the rate and direction of the nonlinear energy transfer. A detailed description of applying bispectral analysis method to study three-wave coupling interaction can be found in Ref. [64]. All the derivatives used in calculating bispectrum can be obtained from experiments using the 18-tip Langmuir probe that has the spatial layout shown in Figure 2-4.

2.4.3 Velocity measurements

In this section, we will introduce two main analysis methods used for velocity field in this dissertation

2.4.3.1 1D TDE technique using Langmuir probe

The time-delay estimation (TDE) technique is mainly used for calculating mean fluctuating velocity field [65]. For calculating mean azimuthal flow velocity by using Langmuir probes, we select two probe tips aligned in azimuthal direction with a distance of Δx, which is less than the turbulent correlation length. When a turbulent structure passes one probe tip at time t and passes another probe tip after some later time $\Delta\tau$, then we can estimate the turbulent velocity as $v_\theta = \frac{\Delta x}{\Delta \tau}$. The time delay $\Delta\tau$ is the time lag calculated from the peaked correlation $C_{xy}(\tau)$ (Eqn. (2.5)). It is noted that we make the assumption that the unfeatured turbulent structure is moving in the azimuthal direction, which is satisfied in our machine that the average azimuthal flow is in the electron diamagnetic direction.

Another alternation method to estimate the mean flow velocity is to calculate phase delay in Fourier domain instead of time delay, which was first introduced by Beall et al. [66]. First we take FFT for the two probe signals in azimuthal direction. By applying Eqn. (2.6), we can calculate the cross-phase between the two signals $\alpha_{xy}(f)$. Thus is effective wavenumber can be estimated by $k(f) = \frac{\alpha_{xy}(f)}{\Delta x}$. The frequency resolved velocity $v(f)$ equals $\frac{f}{k(f)}$. By averaging $v(f)$ over all frequency and weighted

with their cross-power $S_{xx}(f)$ (Eqn.(2.3)), we can obtain a time-averaged azimuthal flow velocity.

2.4.3.2 2D TDE technique using high-speed imaging camera

Due to the limitation of configuration, we can only gain a 1D velocity profile via Langmuir probe measurements. However, the high-speed imaging camera can provide a 2D flow velocity field of the plasma cross-section. The algorithm is similar to the 1D TDE technique except that instead of computing the cross-correlation in only one direction, we compute the cross-correlation in a 2D area with a series of time lag from $\tau = 0$ increasing by every $\delta\tau$, for example a 2D 11×11 grid shown in Figure 2-14. Detailed description of this 2D TDE technique, please refer to [7].

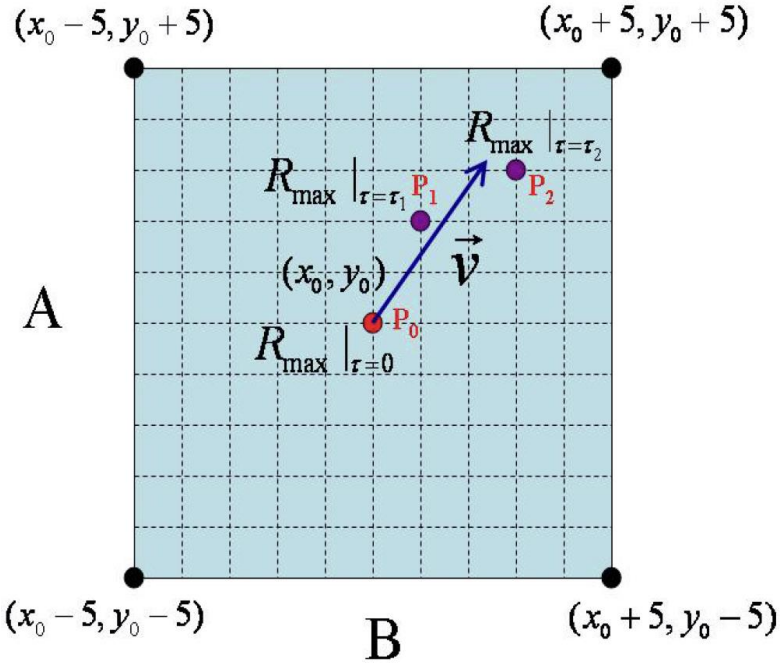

Figure 2-14 2D time-delay estimation (TDE) technique. [7]

2.4.4 Estimation of turbulent quantities in CSDX

The plasma discharge in CSDX is highly stable and repeatable, which provides us a long sequence of data to get statistically converged values when estimating plasma parameters from fluctuations such as auto-spectra, Reynolds stress, and mean fluctuating velocities. The current CSDX 96-channel data acquisition system can store up to 10 seconds of data at a sample rate of 500 kHz for one shot. Because CSDX plasma is stable and all shots taken under the same discharge conditions (magnetic field, gas pressure, etc.) are with the same statistical properties, we can take as many shots as needed to compute the statistics to the desired convergence. Typically for each channel about 7 seconds (~ 3.5 million sample points) of probe data were taken, and they were divided into more than 1000 realizations to compute ensemble averages. Therefore the corresponding statistical uncertainties of the estimated parameters are very small and typically are within the thickness of the produced curves.

2.5 Previous CSDX experimental research in the drift wave-zonal flow system

In order to study feedback loop between drift wave turbulence and shear flow, it is important to demonstrate a detailed description of the in drift-wave-zonal-flow system, especially the transition to drift wave turbulence and the generation of zonal flow. In previous work, this transition has been approached by increasing the magnetic field B, which decreased the normalized gyro-radius according to $\frac{\rho_s}{L_n} = \frac{\sqrt{m_i T_e}}{(eB)L_n}$. Thus we can get a better approach to HW model (refer to Chap 1.2.1). Figure 2-15 shows the radial profiles of standard deviation of density and potential. It is noted that the fluctuation amplitudes for both quantities increase with increasing B field and peak at $r = 3$ cm (location of maximum density gradient). But the radial distributions are different. The potential fluctuation profile appears to contain relatively high levels of fluctuation activity for $r > 4$ cm (outside of shear layer). From the power spectrum of potential fluctuation (Figure 2-16), it clearly shows a transition from linear eigenmode to weakly broadband drift wave turbulence [46]. A two-point technique [66] has also been applied to show the frequency and local wave-number power spectra. Figure 2-17 shows the normalized two-point $S(k_\theta, f)$ spectra for the potential fluctuations at B =1000G at r ~ 3cm [46]. We observed a built-up in k-spectra, indicating the development of the DW turbulence.

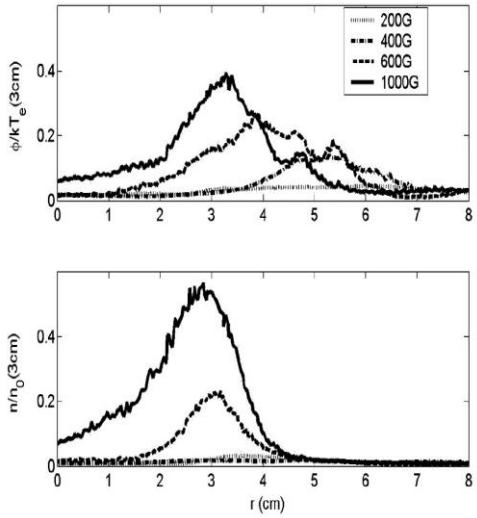

Figure 2-15 Radial profiles of the normalized standard deviations of potential (top panel) and density (bottom panel). [46]

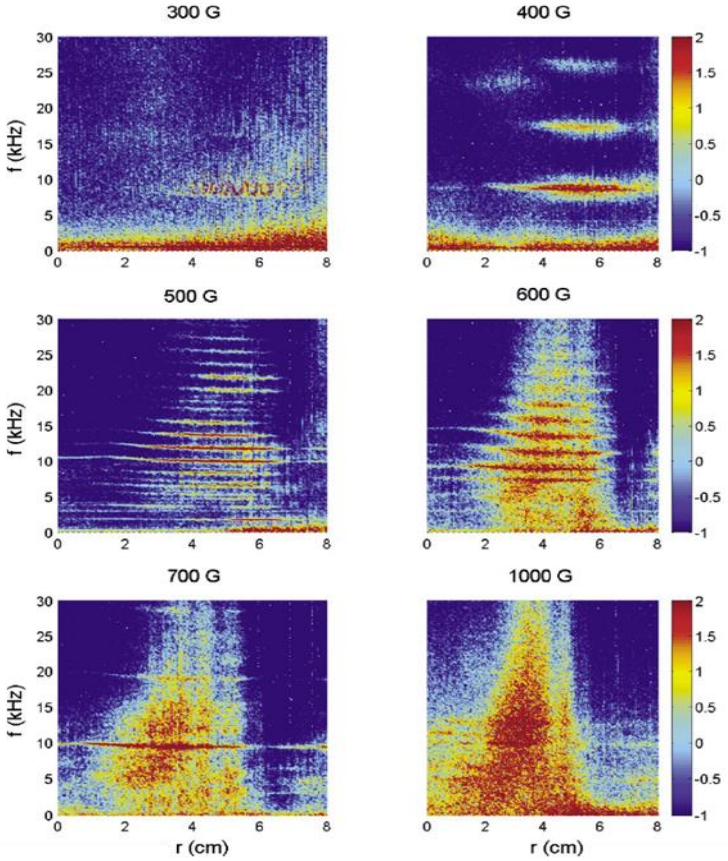

Figure 2-16 Radial profiles of potential fluctuation power spectrum with B filed. [46]

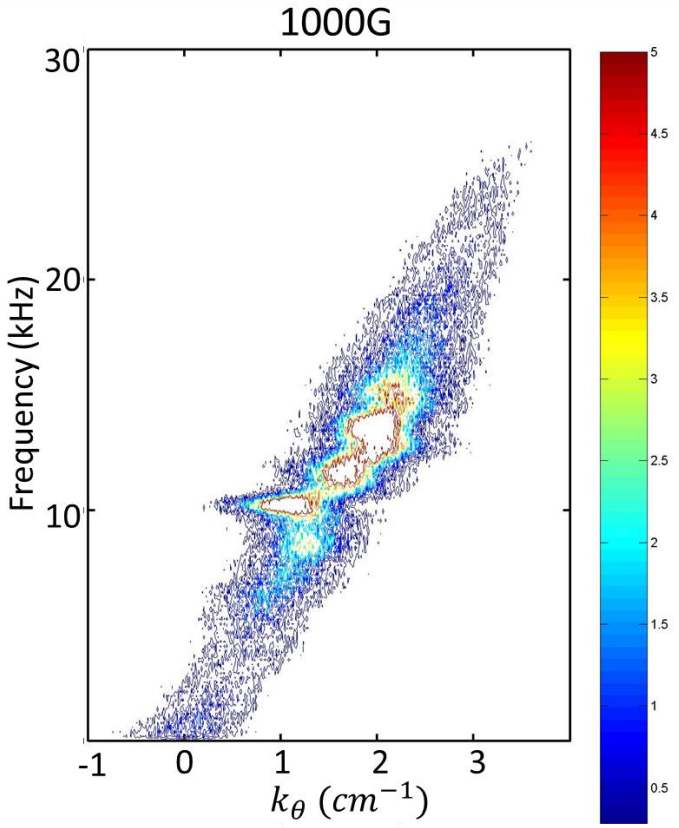

Figure 2-17 Built-up in local k-spectra at 1000G. [46]

As we increase the magnetic field, in addition to observe a broadband turbulence, we observe a strong azimuthal sheared flow develops with B field shown in Figure 2-18. During this transition, the fluctuation energy at low poloidal wavenumbers ($k_\theta \rho_s \leq 0.5$) is linearly stable and sharply increasing over a factor of 100 and the energy contained in linearly unstable fluctuations increases by only a factor of 2-3, which suggests that the energy transfer from turbulence into large azimuthal scale fluctuation is via a nonlinear process, as shown in Figure 2-19.

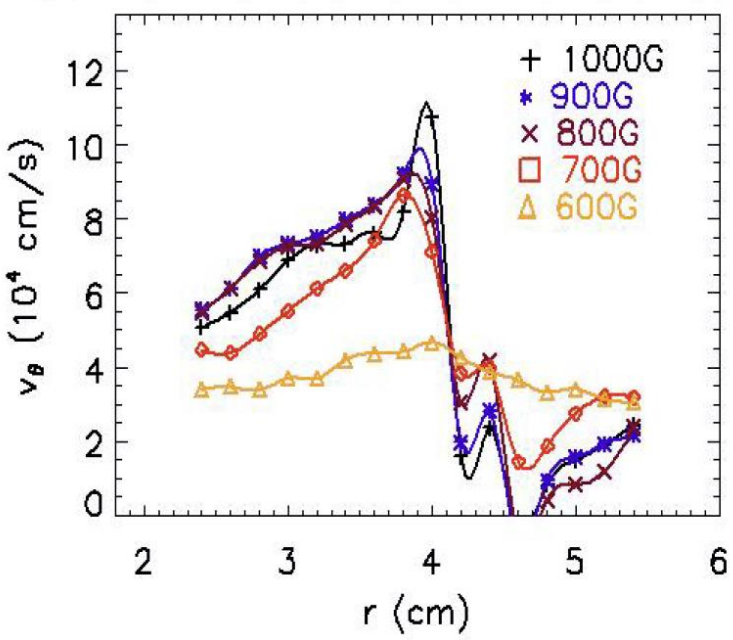

Figure 2-18 Evolution of azimuthal flow with B field [51]

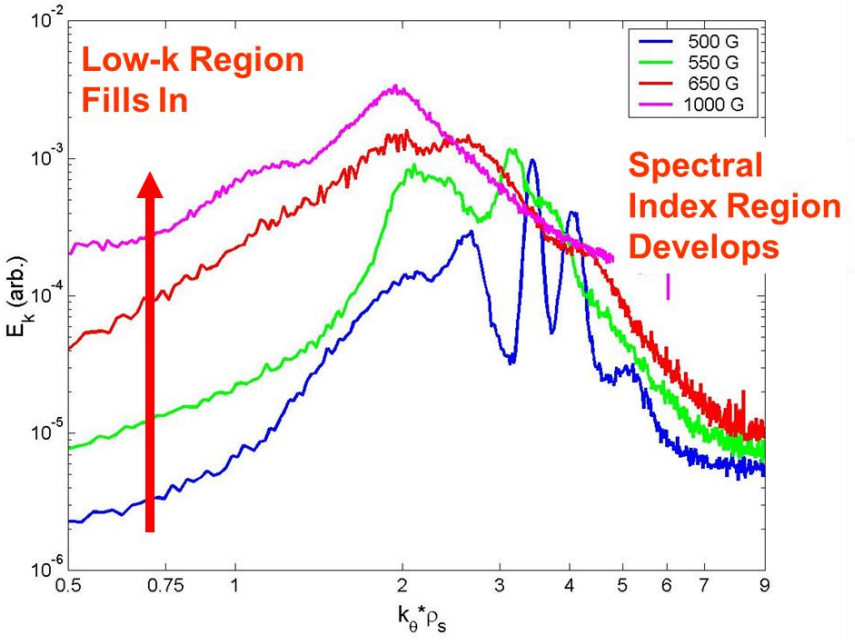

Figure 2-19 Evolution of azimuthal energy wave-number spectrum $\boldsymbol{E(k_\theta)}$ with magnetic fields. [77]

It has found that the plasma spontaneously rotates in azimuthal direction without any external momentum input. In addition, an azimuthally symmetric radially sheared flow has always been demonstrated by probe measurements shown in Figure 2-20. Through azimuthal momentum conservation analysis we found this strong sheared flow is sustained against dissipation by Reynolds stress. The azimuthal component of time-averaged ion momentum equation is given as: [47]

$$\frac{1}{r^2}\frac{\partial}{\partial x}(r^2\langle\tilde{v}_r\tilde{v}_\theta\rangle) = -\nu_{i-n}\langle\tilde{v}_\theta\rangle + \mu_{ii}[\frac{1}{r}\frac{\partial}{\partial r}\left(r\frac{\partial\langle\tilde{v}_\theta\rangle}{\partial r} - \frac{\langle\tilde{v}_\theta\rangle}{r^2}\right)] \qquad (2.11)$$

where $\tilde{v}_r\tilde{v}_\theta$ is the turbulent Reynolds stress, ν_{i-n} is ion-neutral collision rate and μ_{ii} is the ion viscosity. Turbulent Reynolds stress, which is also the turbulent momentum flux can be approximated by floating potential measured from Langmuir probes. $\tilde{v}_r$ and $\tilde{v}_\theta$ are the $\mathbf{E}\times\mathbf{B}$ drift velocities in radial and azimuthal direction separately. By assuming viscosity and neutral damping rate profile for CSDX plasma, we can solve Eqn. (2.9) to obtain the time average azimuthal velocity profile shown in Figure 2-20 by black solid line. As we can see, the result from momentum balance equation agrees well with experimental measurements, indicating the fact that the azimuthal shear flow is generated by turbulent Reynolds stress against viscous damping.

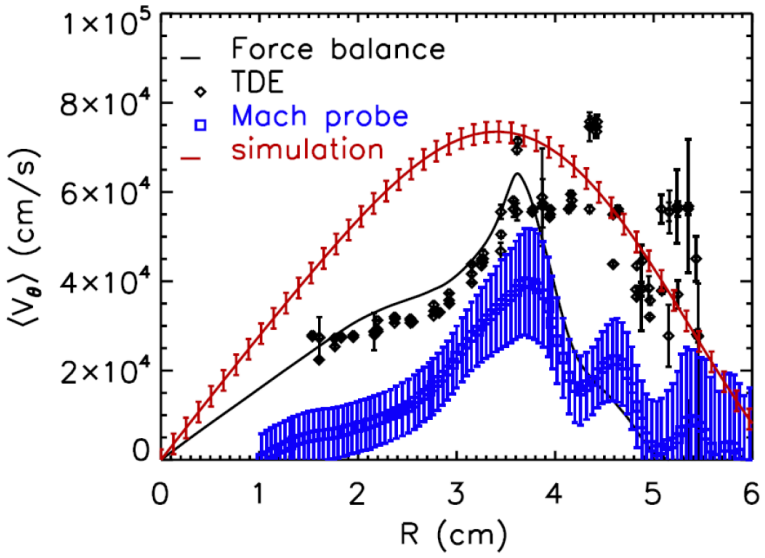

Figure 2-20 Radial profile of azimuthal velocity field measured from different methods. Blue curve: Mach probe data; Black diamonds: TDE inferred azimuthal velocity; black solid line: velocity from turbulent momentum conservation analysis; red curve: two-field turbulence simulation [12].

In a self-regulating system with no external momentum input, where does this net azimuthal momentum come from? Studies on CSDX suggest that the residual stress plays a crucial role in a non-diffusive turbulent momentum transport [49]. The turbulent Reynolds stress can be written as [67]:

$$\langle \tilde{v}_r \tilde{v}_\theta \rangle = -\chi_\theta \frac{\partial \langle \tilde{v}_\theta \rangle}{\partial r} + V_r^{eff} \langle \tilde{v}_\theta \rangle + S_{r\theta}^{res} \tag{2.12}$$

where χ_θ is the turbulent diffusivity, V_r^{eff} is the convective pinch velocity and $S_{r\theta}^{res}$ is the residual stress. In the absence of collisional viscosity and ion-neutral flow dissipation, the turbulent azimuthal momentum balance equation is given as:

$$\frac{\partial \langle P_\theta \rangle}{\partial t} = -\frac{\partial}{\partial r}\left(\langle n \rangle \langle \tilde{v}_r \tilde{v}_\theta \rangle\right) = -\frac{\partial}{\partial r}\left\{-\chi_\theta \langle n \rangle \frac{\partial \langle \tilde{v}_\theta \rangle}{\partial r} + V_r^{eff} \langle \tilde{v}_\theta \rangle \langle n \rangle + S_{r\theta}^{res} \langle n \rangle\right\} \tag{2.13}$$

It is clear that the only way for plasma to obtain a net azimuthal momentum requires a finite $S_{r\theta}^{res}$ at the edge of plasma column. Thus we can calculate $S_{r\theta}^{res}$ from Eqn. (2.10) by estimating χ_θ from turbulent correlation time $\langle \tilde{v}_r^2 \rangle \tau_c$. The corresponding results are shown in Figure 2-21, that the residual stress profile peaks at the plasma edge. When combined with a no-slip boundary condition in the outer regions (r>5cm or so) due to strong flow damping by neutral gas in this region, this turbulent stress then gives rise to a net plasma fluid rotation in the observed direction. [49]

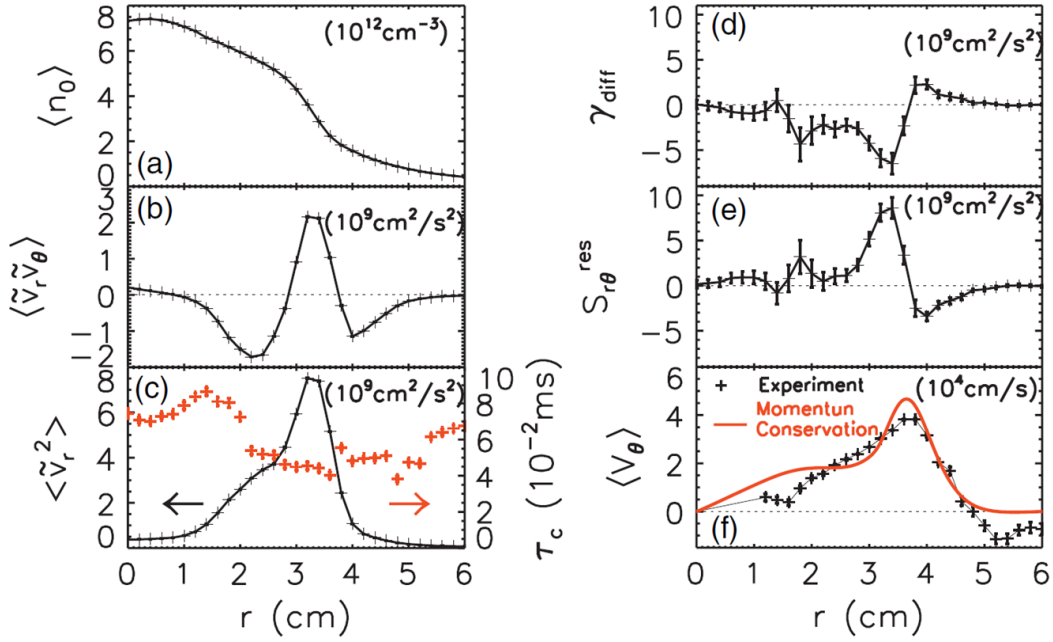

Figure 2-21 Radial profiles of (a) mean density, (b) turbulent Reynolds stress, (c) mean square of turbulent radial velocity (d) diffusive turbulent transport term, (e) residual stress and (f) mean azimuthal velocity. [49]

This shear flow generation process was studied in the Fourier domain using bispectral analysis techniques discussed above [48]. As we can see from Figure 2-22, the plasma at 1000 G is weakly turbulent with some coherent modes. Both the density (Figure 2-21(a)) and potential spectra (Figure 2-21(b)) are peaked around 5 kHz and 10 kHz, which has been identified as collisional drift waves [46]. While there is another peak at very low frequencies ($f \leq 1.5$ kHz) A peak in the potential and velocity fluctuation spectra is also seen at very low (Figure 2-21(c)) spectra but not in

the density spectra. These low frequency fluctuations are due to the slow evolution of the azimuthal sheared flow and are predicted by theory. [51].

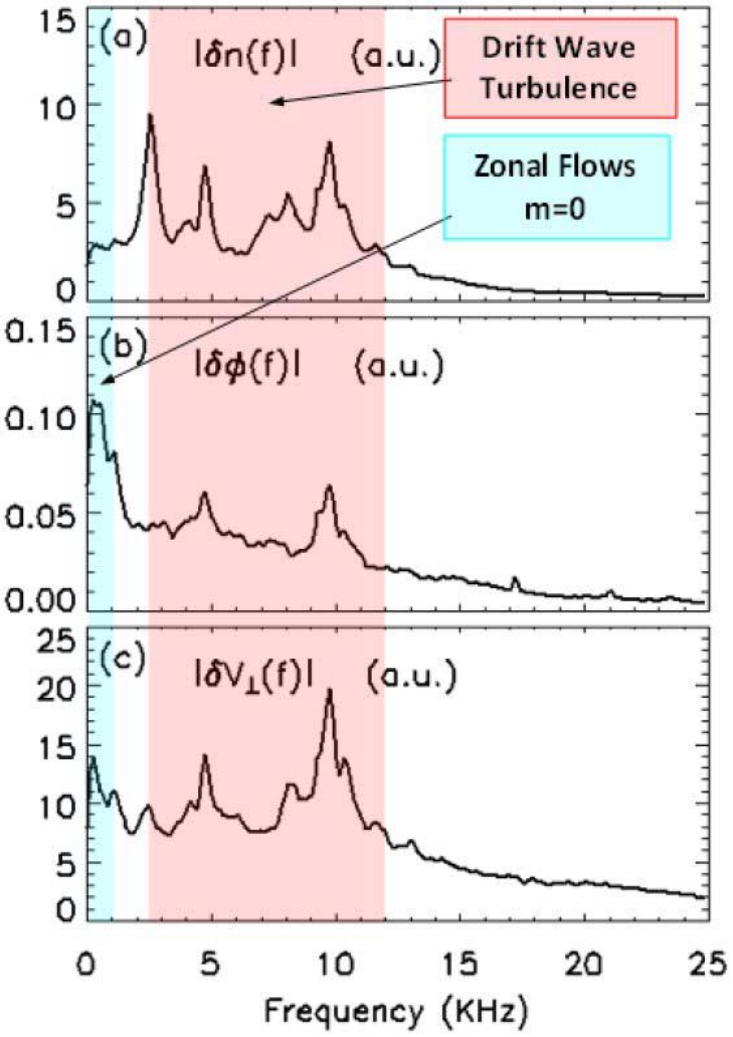

Figure 2-22 Auto-spectra profiles (a) density, (b) potential and (c) azimuthal velocity for the weakly turbulent plasmas in CSDX (B = 1000G). [48]

By performing the bispectral analysis in Fourier domain, we gain an insight of nonlinear kinetic energy transfer between drift wave turbulence and shear/zonal flow. Here the positive value of nonlinear kinetic energy transfer rate $\boldsymbol{T_u(f)}$ indicates fluctuations at frequency $\boldsymbol{f}$ are gaining energy and negative value indicates losing energy. It is clear to see that the drift wave frequency region (red color region in Figure 2-23) loses energy to very low frequency region. While the zonal flow region (blue color region in Figure 2-23) gains energy from drift wave turbulence.

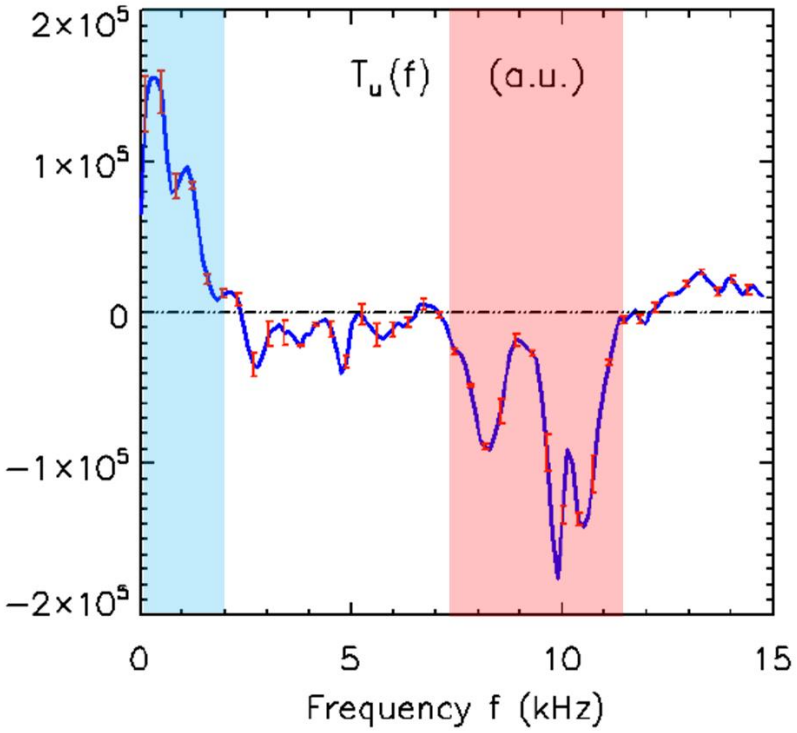

Figure 2-23 Frequency Resolved Net Kinetic Energy Transfer. Red shadow area indicates zonal flow frequency region and blue shadow area indicates the drift wave turbulence frequency region. [48]

Further study has been performed to look into the underlying dynamics for drift wave turbulence and zonal flow. Figure 2-24 provides sequential snapshots from fast camera showing how the small scale eddies interact with a large scale shear flow. The structures were born at the inner dashed circles r ~ 3cm and propagating outwards to the outer dashed circle (r ~ 3.5cm; shear layer) in a spiral trajectory. The snapshots clearly show the turbulent structures tilt and gradually absorbed by the shear layer, which is also described as a "tile-stretch-absorption" process.

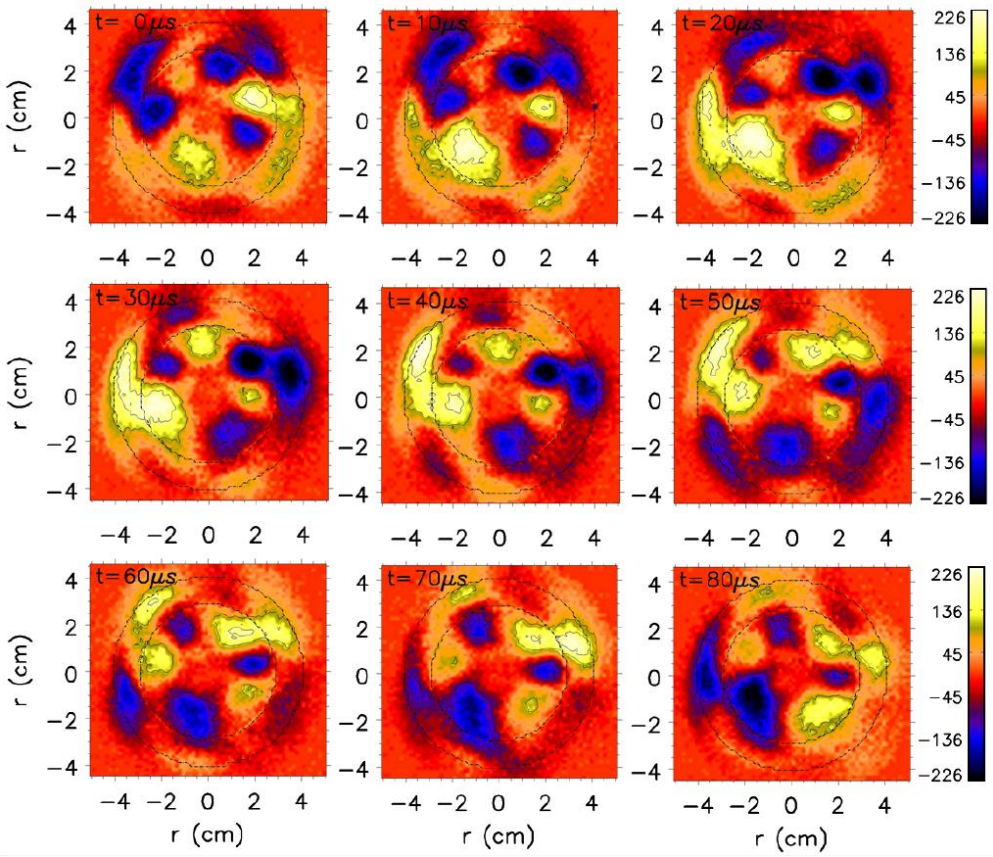

Figure 2-24 Sequential snapshots showing the birth, evolution, and death of vortex-like structures at weakly turbulence plasma state [55].

Previous experimental and theoretic studies on CSDX provide a good understanding of a self-consistent drift wave-zonal flow system. The zonal flow is generated by drift wave turbulence, but also regulates and suppresses turbulence. For reasons unknown, the helical m=1 geometry antenna that we used in our experiments couples effectively at magnetic fields of up to 2400G, which reveals more interesting physics phenomenon. This dissertation focuses on investigate a novel phenomenon, the up-gradient inward particle transport in drift wave-zonal flow system.

Chapter 3

Development of an up-gradient turbulent particle flux in a linear plasma device

3.1 Introduction

In this chapter, we report on the experimental observations of an up-gradient inward turbulent particle flux in CSDX, giving a detailed experimental picture of the development of an inward particle flux using two diagnostics: fast imaging camera and Langmuir probe.

Flow and flow shear can modify turbulence and transport through a number of processes. First, the shear can lead to radial decorrelation or "shearing apart" of turbulent eddies, reducing their radial extent and therefore their transport effectiveness [42]. Second, by the nonlinear transfer of energy from the fluctuations to the shear flow, the saturated level of the turbulence can be reduced. These mechanisms can give rise to a reduction in the rate of cross-field transport, but cannot reverse the sign of the particle flux (since they all affect positive definite quantities that yield outward transport). The phase shift between density $\tilde{n}$ and poloidal electric filed $\tilde{E}_\theta$

fluctuations can result in a change in the direction or sign of the turbulent particle flux, which is given as [24]:

$$\Gamma_{turb} = <\tilde{n}\tilde{V}_r> = \frac{<\tilde{n}\tilde{E}_\theta>}{B_z} \tag{3.1}$$

$$= \frac{2}{B}\int_0^\infty |n(\omega)||E_\theta(\omega)|\gamma_{n,E_\theta}(\omega)\cos[\theta_{n,E_\theta}(\omega)]d\omega$$

Here, electrostatically driven particle transport is dependent on the correlation between density and electric field fluctuations in low frequency turbulence (where $E \times B$ is the dominant particle response). Flow and flow shear can modify both the cross-phase and cross-coherency between density and potential fluctuations, leading to a reduction of the flux in the absence of amplitude reduction; under the right conditions the phase shift can also lead to a negative or inward flux as well. Furthermore, the flow shear itself can act as a free-energy source, leading to a Kelvin-Helmholtz (KH) instability. Finally, in our cylindrical plasma, strong azimuthal rotation also leads to an effective radial gravity term that can destabilize interchange (Rayleigh-Taylor, or RT) instabilities. Both KH and RT instabilities can have very different cross-phase than found in collisional drift waves [68] and thus may lead to very different turbulent particle transport.

Our results show the gradual, simultaneous development of a radially sheared azimuthal flow that grows and reaches it maximum in the region where the turbulence does work on the flow via the turbulent Reynolds stress. At the same time, an inward particle flux also gradually develops just inside the region of peak shear flow. At this

location the sheared flow does work on the finite frequency fluctuations, consistent with a shear flow-driven instability that is spatially localized to the region located between the density gradient maximum (which has been shown to drive collisional drift wave turbulence [46,51]) and the maximum flow shear. The inward flux therefore appears to be associated with the existence of spatially separated and distinct free-energy sources that drive the fluctuations, consistent with the fundamental picture of off-diagonal transport coefficients summarized above. The results here show that a total net negative particle flux can develop as a result of a spontaneously generated shear flow (i.e. in a flow which is not driven externally), suggesting that such processes could be an important transport process in confinement experiments with self-driven sheared E×B flows [69].

3.2 Experimental Setup

For these experiments, CSDX was operated with a 13.56 MHz, 5 kW RF radio frequency helicon wave source equipped with a helical m=1 15 cm diameter antenna. A digitizer with up to 96 channels sampling at 500 kHz and anti-aliasing filters are used to record probe data. The resulting Nyquist frequency is 250 kHz, well above the observed fluctuation frequency. A RF matching circuit is adjusted such that less than 30 W of power is observed reflected. Measurements of mean plasma profiles, the fluctuating density, potential, and electric fields along with the resulting turbulent particle flux are made by both an 18-tip Langmuir probe inserted radially in a port located 1m downstream from the source (port α in Figure 3-1) and a 4-tip Langmuir

probe located 1.7m downstream from the source (port β in Figure 3-1). The configurations for 18-tip Langmuir probe can be found in Figure 2-4 and for 4-tip probe in Figure 2-6. The 18 tips are arranged as dual 3×3 arrays, which are shifted with respect to each other along the B field direction by 1.5 mm. One 3×3 array measures floating potential and another one measures ion-saturation current, biased by −100 V. In the absence of strong electron temperature fluctuations the floating potential fluctuations are interpreted as plasma potential fluctuations. Similarly, the measured ion saturation current fluctuations are interpreted as density fluctuations. Both two probes have shown similar experimental results. In this paper, we are focused on the experimental results with 18-tip probe.

A Phantom V 710 high speed camera is placed at the end of the machine to capture the motion of the plasma visible light emission. For this experiment, image sequences of 5000 frames were recorded at 210500 frames/s with an exposure time of 1 ~ 2 μs with 128×128 image resolution, and a Pentax 50 mm *f* / 1.4 lens is used in the experiments. We use two mirrors to increase the optical path length, as shown schematically in Figure 3-1. The light intensity fluctuations are considered to be proportional to the ion saturation current and thus a proxy for density fluctuations [59,60]. Visible light from the plasma is steered using two large mirrors on to a telescope placed about 7 meters away from the focal plane using a 180mm, f/4 lens as the objective. Detailed description about fast camera can be found at [21]. As recently discussed in detail elsewhere [61], detailed statistical properties and dispersion relations can be determined from the fast imaging data, and can be related to plasma instabilities thought to be operative in the experiment.

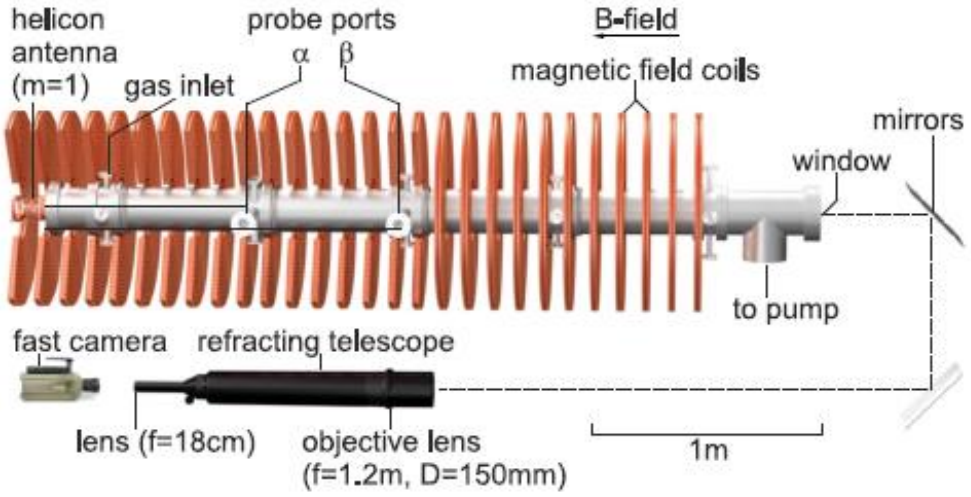

Figure 3-1 Schematic of CSDX (include the layout of Langmuir probe and camera diagnostic at the experiment)

The development of an up-gradient inward particle flux in a system with spontaneously generated sheared E×B flows in a simple magnetic geometry provides the opportunity to perform a detailed study of modifications of turbulence and turbulent transport in a system free from complications associated with toroidal systems (e.g., field line curvature, poloidal asymmetry, trapped particles). Good diagnostic access to CSDX provides for detailed measurements of the spatial and temporal characteristics of the turbulence. The development of the particle flux and shear layer profiles somehow was documented in earlier work where azimuthally symmetric m=0 RF antenna were used and suggested that higher magnetic fields seem to lead to the development of inward particles fluxes and strong shear layers. There

observations motivated further study of the evolution of these behaviors at even higher magnetic fields. For reasons that are not understood so far, the m=0 antenna geometry was found to have difficulty in maintaining a stable RF matching condition at higher magnetic fields. We found that a radius of 7.5 cm, m=1 helical antenna does in fact couple RF power into the plasma effectively at magnetic fields of up to 2400G. Thus the work reported here has used this source geometry. Experiments have been carried out across a range of parameters (argon fill pressure remains 3.20 mTorr): (1)1.6 kW source power input with 20sccm flow rate; (2) 1.6 kW source power input with 25sccm flow rate; (3) 1.8 kW source power input with 15sccm flow rate; (4) 1.8 kW source power input with 20sccm flow rate; (5) 1.8 kW source power input with 25sccm flow rate, and they all show very similar plasma characters. We observe plasma dynamics from nonlinearly-coupled but distinct eigen-modes at low magnetic fields (400G ~ 1100G) followed by a very sharp transition (1200G ~ 1600G) to a centrally peaked density with stiff profiles and very bright blue core mode [21]. The profiles shown here are from experiments carried out at 3.20mTorr Argon fill pressure with 15sccm flow rate and 1.8kW rf source power input. We only show data taken for r>2cm from plasma center since the probe tips start arcing when they get close to the core.

3.3 Experimental results

3.3.1 Motivation

As the magnetic field is scanned in the upgraded CSDX, we see the transition to broadband fully developed turbulent features [refer to Figure 2-16 in Chapter 2]. Detailed studies of this transition can also be found in Ref. [21,46]. Under some conditions (increasing magnetic field above to a critical value), we observe a net inward up-gradient flux. Figure 3-2 shows the evolution of radial profiles of turbulent particle flux. For low magnetic fields, the particle flux is positive at all radii that indicate the plasma propagates outward to the larger radii. This observation is qualitatively consistent with a picture of turbulent diffusive transport down the density gradient. As we increase magnetic field to $B \geq 1200G$, the particle flux becomes negative, corresponding to up-gradient transport, for radii between $3 < r < 5$ cm. In the following sessions, we will give a detailed description of the development of the inward flux, focused in the transition region ($1000G \leq B \leq 1300G$) by independent diagnostics, including Langmuir probes and high-speed imaging camera.

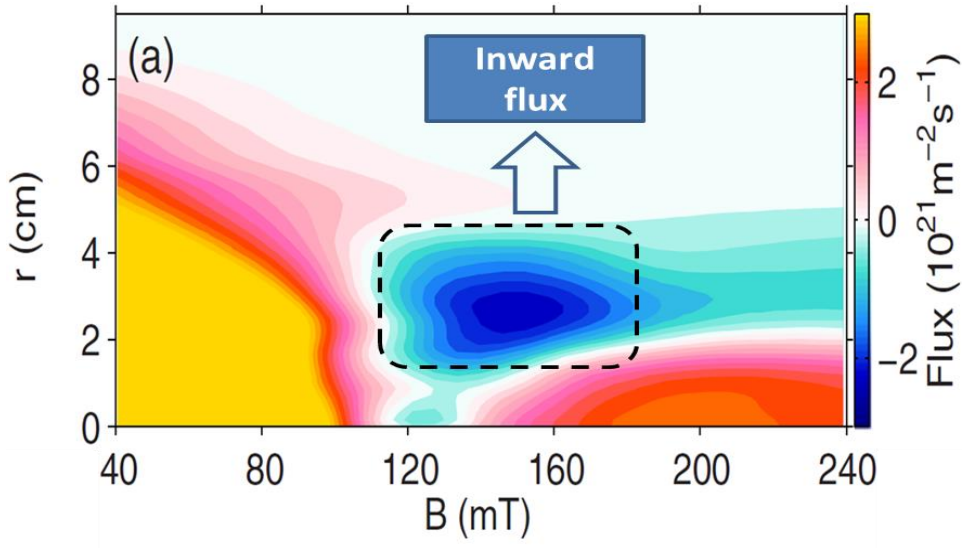

Figure 3-2 Evolution of turbulent particle flux. [21]

3.3.2 Mean profiles

The radially-resolved profile of equilibrium density with 1mm spatial resolution/100msec duration time are averaged for several different magnetic fields shown in Figure 3-4. Heat input from the RF source sustains a centrally peaked plasma density [Figure 3-4(a)]. The electron temperature profile shown in Figure 3-3 is obtained from calculation of the inflection point near the electron saturation regime of the standard I–V (current versus voltage) curves of a swept rf compensated Langmuir probe. We note that the density profile becomes steeper at r = 2.5cm as we increase the magnetic field to 1300G. Figure 3-4(b) provides the density fluctuation amplitude normalized to the equilibrium density. The density fluctuation amplitude increases with the magnetic field and peaks around the region of maximal density gradient.

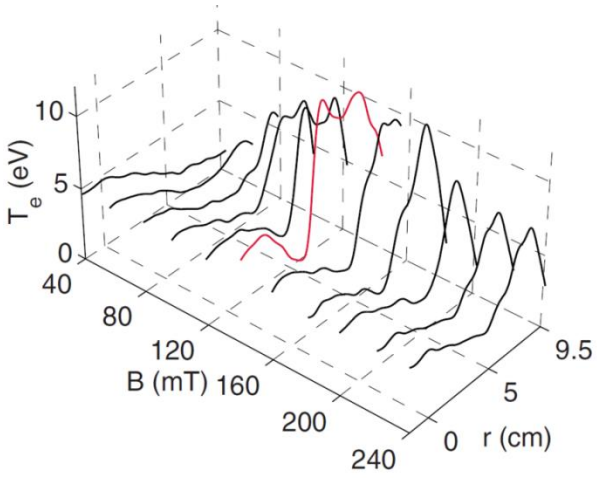

Figure 3-3 Radial profile of electron temperature. [21]

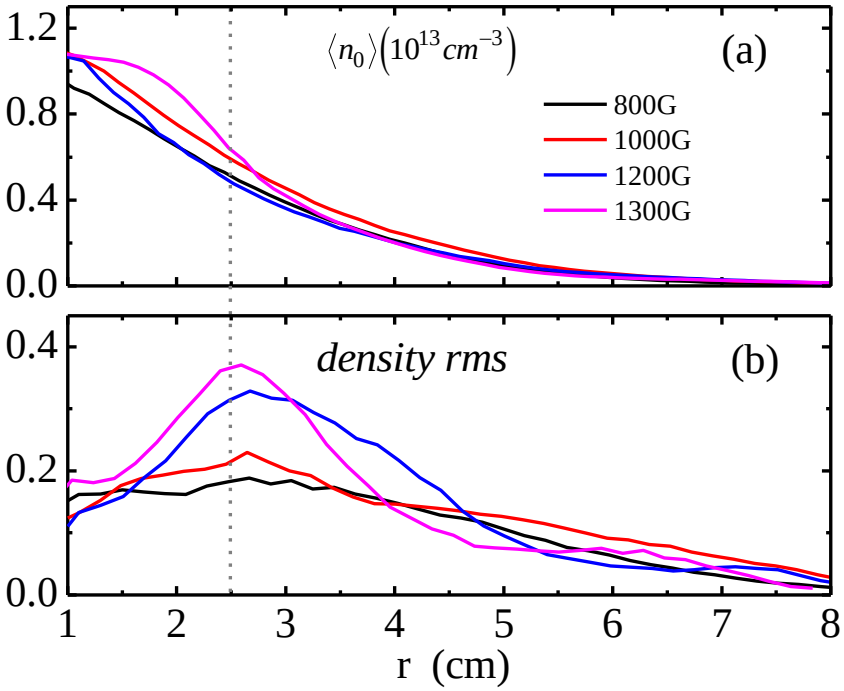

Figure 3-4 Time-averaged radial profiles of (a) mean density $\langle n_o \rangle$ calculated from ion saturation current (b) RMS amplitudes of density fluctuations, normalized by the equilibrium density.

Figure 3-5(a) shows the radial profiles of the time-averaged azimuthal velocity computed using a time-delay estimate (TDE) technique applied to imaging data as the magnetic field is increased from 800G to 1300G. A radially sheared azimuthal flow in the ion diamagnetic drift direction is observed near the center of the plasma (r < 2cm) and another azimuthally symmetric sheared flow in the electron drift direction located at r ~ 6cm develops as we increase the magnetic field. These two shear regions at r = 1-2cm and r ~ 6cm straddle the location of maximum density gradient at r ~2.5cm. Between the two shear layers the flow approximates solid body rotation in that the azimuthal velocity increases linearly with distance. Figures 3-5(b) shows the evolution of the radial profiles of the axial ion fluid velocities $\boldsymbol{V_z}$ as measured by the Mach probe. In the parallel direction the $\boldsymbol{V_z}$ profiles show that the inner plasma flows away from the source toward the pump end of the machine while it seems to reverse direction at the edge. The central axial velocity is small for low magnetic fields (~0.3 km/s for B = 400G) and seems to monotonically increase to ~1.8 km/s at B = 1300G. Figure 3-6 shows the development of inward turbulent particle flux in the transition region 1100G ≤ B ≤ 1400G.

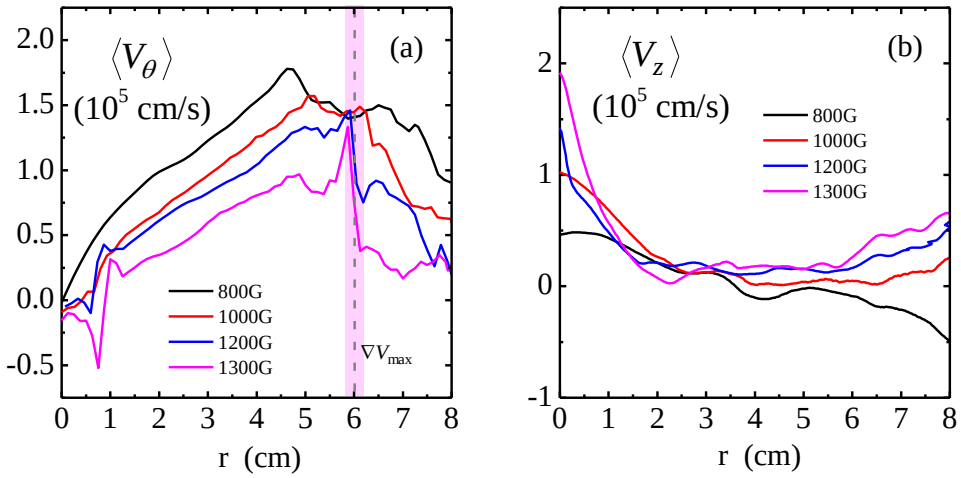

Figure 3-5 Time-averaged radial profiles of: (a) mean azimuthal velocity $\langle \bar{V}_\theta \rangle$ calculated by TDE (b) mean parallel velocity $\langle \bar{V}_z \rangle$ measured by Mach probe.

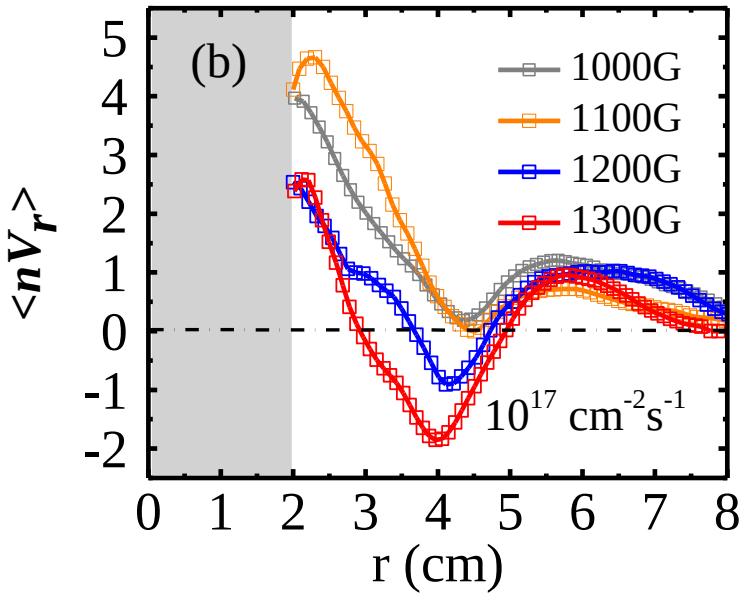

Figure 3-6 Onset of up-gradient particle flux. Magnetic fields from 1000G to 1300G. [82]

To estimate the significance of radial transport in the global particle balance, we use the measured turbulent radial particle flux. We focus our attention on the position near r =2.5cm, since this is the radial location where we see the density gradient gets steepened. Thus we made an estimation of particle loss due to radial and parallel transport.

For B = 1000G, r = 2.5cm (location of density gradient steepening), particle loss due to radial transport is calculated as follows. The effective area for radial transport is the surface area of a cylinder bounding the r=2.5cm radius:

$$A_{\perp} = 2\pi r_{pl} L_{\parallel} = 2 \times 3.14 \times 2.5 \times 300 \sim 5 \times 10^{3}\ cm^{2} \tag{3.2}$$

At 1000G, at a condition just below the development of an inward particle flux, we find that the outward radial particle flux has a value

$$\Gamma_r = \langle \tilde{n}\tilde{V}_r \rangle \sim 10^{17} cm^{-2} s^{-1} \text{ (from experimental measurements)} \tag{3.3}$$

We can then estimate the rate of particle loss from this cylinder in the central portion of the plasma due to radial transport to be given as $\Gamma_r A_{\perp} \sim 5 \times 10^{3} \times 10^{17} \sim 5 \times 10^{20}\ s^{-1}$.

The particle loss through the bounding end-plate area with radius r=2.5cm due to parallel transport is calculated next. The area of the bounding endplate is given as

$$A_{\parallel} = \pi r_{pl}^{2} = 3.14 \times 2.5 \times 2.5 \sim 20\ cm^{2} \tag{3.4}$$

For the parallel velocity that we used for estimation, it is calculated by M $* C_s$ where M is the Mach number measured by a Mach probe. $C_s \sim 10^6 \sqrt{\frac{T_e}{m}}$ and take Te = 4 eV for Cs calculation. Thus $V_\parallel$ is about the order of $10^5 cm/s$. The parallel particle flux arising from the steady-state plasma flow along B is estimated as:

$$\Gamma_\parallel \sim n_0 V_\parallel \sim 5 \times 10^{12} \times 10^5 \sim 5 \times 10^{17} cm^{-2} s^{-1} \tag{3.5}$$

$$\text{Thus, } \Gamma_\parallel A_\parallel \sim 8 \times 10^{17} \times 20 \sim 2 \times 10^{19}\ s^{-1} \tag{3.6}$$

As we can see at B = 1000G, r = 2.5 cm, $\Gamma_r A_\perp$ is about one order of magnitude larger than $\Gamma_\parallel A_\parallel$. Thus a large reduction, or even vanishing, of the radial transport should have a measurable effect on the mean density profiles. In particular, when we increase the magnetic field to 1300G, the radial particle transport in the region around the peak density gradient changes sign, and has a location where it vanishes. Thus from a global particle balance, we should expect to see a steepening in density gradient and an increase in $V_\parallel$ which then carry the particles out of the plasma. Both of these changes in the time-averaged equilibrium of the plasma are observed in the experiment in qualitative agreement with these expectations. Thus we can conclude nonetheless that the observed changes in the plasma equilibrium radial profiles and parallel flow are at least qualitatively consistent with the observed changes in cross-field transport. A more quantitative comparison would require a measurement of the absolute particle source rate including recycling from the walls, which is not currently available.

3.3.3 Observations of up-gradient particle flux using fast-speed camera

As mentioned previously, inward particle transport has been observed at different source configurations and probe configurations, indicating that this phenomenon is independent of the details of the plasma source. However, the probe measurements of the particle flux ignore effects like Te fluctuations, which in principle could affect the measurement of the fluctuating azimuthal electric field, and thus the resulting radial component of the fluctuating $\mathbf{E} \times \mathbf{B}$ velocity. Thus in order to provide independent confirmation of the up-gradient flux observations, we have also used high speed imaging to track the motion of turbulent structures.

In order to do this, we first show that the camera can observe density fluctuations. In Figure 3-7, we show the cross-correlation coefficient computed between the Langmuir probe ion saturation current I_{sat} and the camera fluctuating visible light intensity sign I_c. The results show that $Corr(I_{sat}, I_c)$ reaches values as large as 0.75 with a zero delay time. The decay time of this cross-correlation is larger than 10ms reflecting a high correlation level for times much longer than turbulent correlation time or azimuthal rotation times.

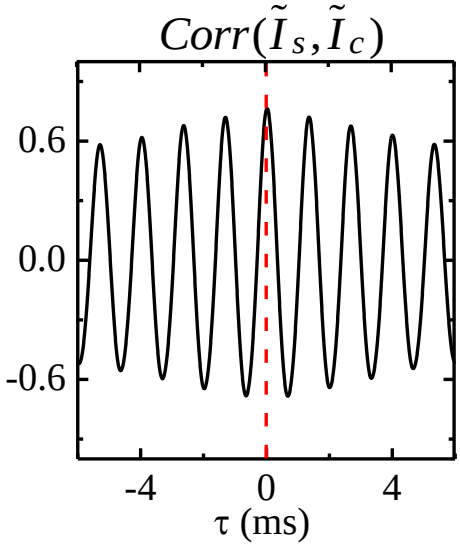

Figure 3-7 Cross-correlation coefficient between the Langmuir probe and the fast camera signals.

It is known that the electron temperature gradient may give rise to temperature fluctuations which could affect the interpretation of probe and imaging data. The observed normalized density fluctuation amplitude $\frac{\delta n}{n}$ is slightly smaller than the mixing length estimate $\frac{\delta n}{n} \sim \frac{\nabla n_0}{n_0} \cdot L_r^{corr} \sim 0.5$ (here n_0 is the background density and L_r^{corr} ~1cm is the radial turbulent correlation length) indicating that this estimate gives a reasonable upper bound for fluctuation amplitude. In the region of inward flux, the electron temperature gradient scale length is ~5 times larger than the density gradient length [21] and thus we expect $\frac{\delta T}{T} < \frac{1}{5} \frac{\delta n}{n}$ ~0.1. This value is too small to cause $\frac{\delta T}{T}$ to dominate the probe I_{sat} fluctuations and thus the I_{sat} fluctuations are primarily caused by density fluctuations. Thus, since the Isat fluctuations are due primarily to density

fluctuations, we can then conclude that the large value for $Corr(I_{sat}, I_c)$ then indicates that light intensity fluctuations I_c are also due primarily to density fluctuations.

Having established that the visible light fluctuations are due primarily to density fluctuations, we next examine the dynamics of the light fluctuations. Figure 3-8 shows the snapshots of camera movies recording light of Ar I emission lines for three different magnetic fields (1000G, 1400G and 2400G). At B = 1000G [Figure 3-8 (a-d)] in the cross-section from r ≤ 5 cm (inside red circle) the eigenmodes m = 1 and m = 5 are dominant and superimposed. The waves propagate clockwise in the electron diamagnetic drift direction. In the edge region (r > 5 cm) low amplitude fluctuations are present and are due to the dim light emission close to the signal-to-noise ratio. Figure 3-8 (f-i) demonstrate the dynamics at B = 1400G. An m=2 fluctuation that bears a strong resemblance to an m=2 linear drift wave eigenmode can be seen in the region inside r = 3cm (inside blue circle), while the dynamics outside of this region are now dominated by growing, azimuthally propagating, and merging structures that do not have any clear cylindrical eigenmode-like characteristics. Inside of r = 2cm we observe a quasi-coherent structure with radially elongated "fingers" that have a much higher azimuthal mode number m ≈ 10 − 15. For the 1400G condition, structures located in the region 2cm < r < 4cm spiral radially *inward* towards a barrier at r~2cm where the radial motion ceases. At radii larger than r > 4 cm the structure motion is dominated by radial-azimuthal outward spirals, indicative of outward transport in this region. For magnetic fields larger than 1400G, the structures propagate with lower azimuthal velocities. The dynamics changes to intense vortex structures which form in the outer plasma region (r > 4-5cm) and which slowly spiral inwards towards the

central plasma which is rotating more rapidly in the electron diamagnetic direction. Above 1400G, the amplitude of the vortices and the intensity of the dynamics further increases with B. At magnetic field of 2400G [Figure 3-8 (k-n)] the snapshots show the creation, propagation, merging and decay of vortex structures in the edge region and bright azimuthally elongated arms spiraling from the edge ($r \sim 6$ cm) into the center at $r \sim 2$ cm.

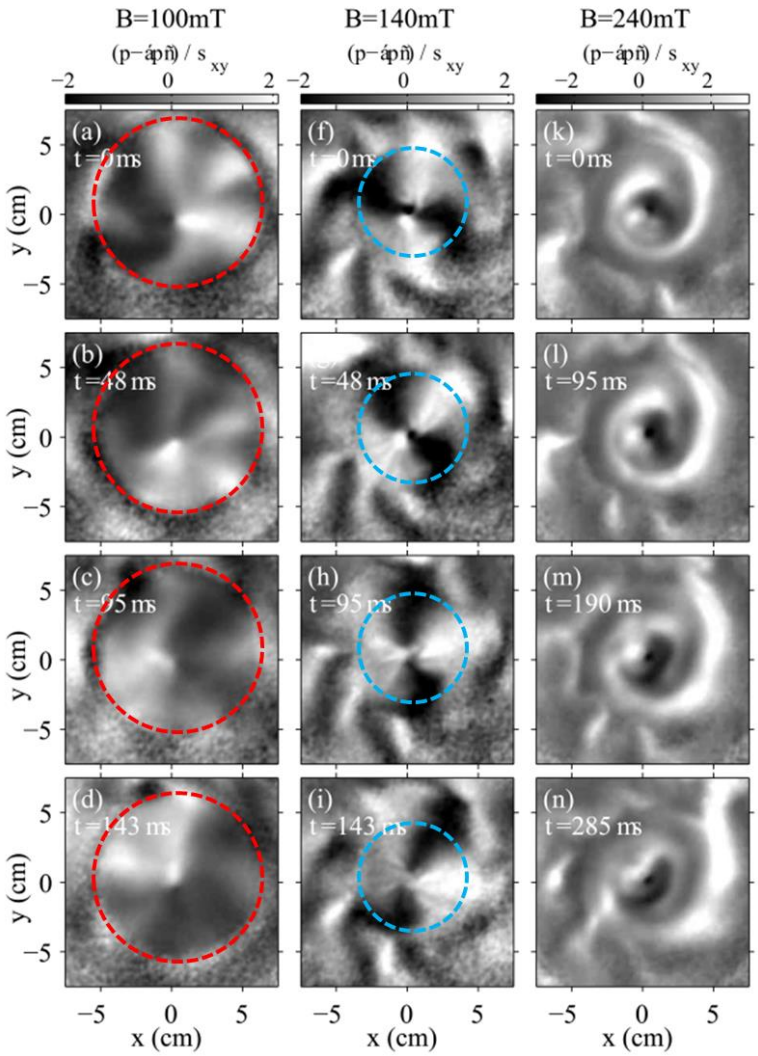

Figure 3-8 Snapshots of camera movies recording light of Ar I emission lines for three different magnetic fields (B = 1000G, 1400G and 2400G). Each pixel is normalized to its standard deviation to enhance contrast. [21]

We can more clearly illustrate this behavior by constructing a two-dimensional velocity field using the 2D TDE technique described in Chapter 2, and then use this field to construct trajectories which are everywhere tangent to the flow field. These will then correspond to turbulent flow streamlines associated with the turbulent light

intensity structure motion (which as shown above is essentially equivalent to the motion of turbulent density structures). The results [Figure 3-9(a)] clearly reveal that at B=1000G, positive density structures anywhere in the plasma cross-section tend to spiral radially outward and move azimuthally in the electron diamagnetic drift direction. The net result is then an outward flux of light intensity (and thus of density) across the plasma column. In contrast, the velocity field at B = 1300G [Figure 3-9(b)] shows a very different behavior; *that streamlines launched from the region exhibiting a net inward particle flux measured by the Langmuir probes, spiral inwards.* This inward motion stops at a closed surface located at r ~2cm, forming an effective *barrier* through which the fluctuations do not penetrate. At radii larger than r ~ 4cm the velocity field is dominated by radial-azimuthal outward spirals, indicative of outward transport in this region. Again, this behavior is consistent with the observations of outward particle flux in the outer region of the plasma as seen in the probe data.

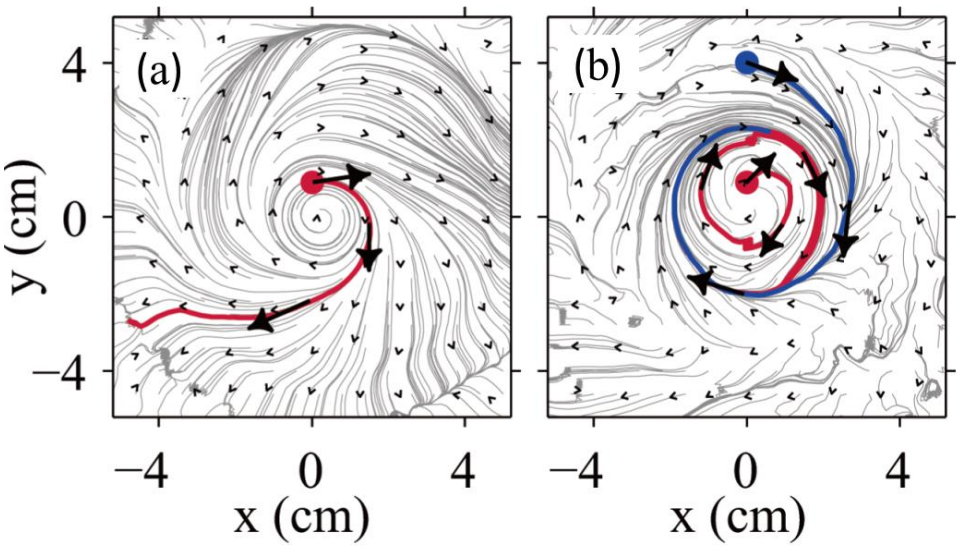

Figure 3-9 Frequency averaged velocity fields obtained from velocimetry of the camera movies shown in streamline plots at (a) B = 1000G and (b) 1300G. The direction of the magnetic field is ⊗. [82]

3.3.4 Comparison between the flux estimates from probes and imaging

As it is already shown that these light intensity fluctuations from camera are highly correlated with ion saturation current fluctuations from Langmuir probe, indicating that the light fluctuations are essentially density fluctuations. Furthermore our 2D TDE velocimetry allows us to determine the spatiotemporally resolved structure velocity. We can then use these results to construct an independent measure

of the turbulent particle flux and compare that with the probe measurements of the cross-field particle flux. Figure 3-10(a) shows the radial profiles of radial light intensity flux defined as $< \tilde{I}_c \tilde{V}_r >$ averaged which is averaged over the poloidal coordinate at each radius. Figure 3-10(b) shows the radial profiles of turbulent particle flux by Langmuir probe for comparison. The results show that the radial light intensity flux and turbulent particle flux profiles exhibit a similar behavior. In particular, they both show an outward-transport fluxes at low magnetic fields (Below 1200G) and the gradual development of an inward-transport fluxes as we increase magnetic field to higher magnetic fields. Also this inward fluxes locate at the same radial location 3 < r <5 cm in both profiles. We note that at lower magnetic fields the probe and imaging do not show a strong agreement. This might be due to the finite $k_\parallel$ of drift waves which dominate the fluctuations at 1000G, and the fact that, as discussed later in this dissertation, there is likely a Kelvin-Helmholtz instability (which has $k_\parallel = 0$) at higher B field. As a result, we have $\frac{k_\parallel}{k_\perp}\Big|_{1300G} < \frac{k_\parallel}{k_\perp}\Big|_{1000G}$. Since the camera integrates the light intensity over a depth-of-field of $\delta z \sim 10$ cm, at the lower magnetic field the more pronounced helical nature of the fluctuations will then cause them to be partially blurred by the line-integration process, which will in turn begin to cause difficulties with inferring the intensity flux $\langle \tilde{I}_c \tilde{V}_r \rangle$ under these conditions. However this conjecture needs to be explored in future work. Regardless of this issue, it is clear that for higher magnetic fields conditions, two independent diagnostic techniques see the development of an inward particle flux, and the mean density gradient steepens in response to this inward flux. Thus two independent

diagnostic techniques see the development of an inward particle flux and the mean density gradient steepens in response to this inward flux.

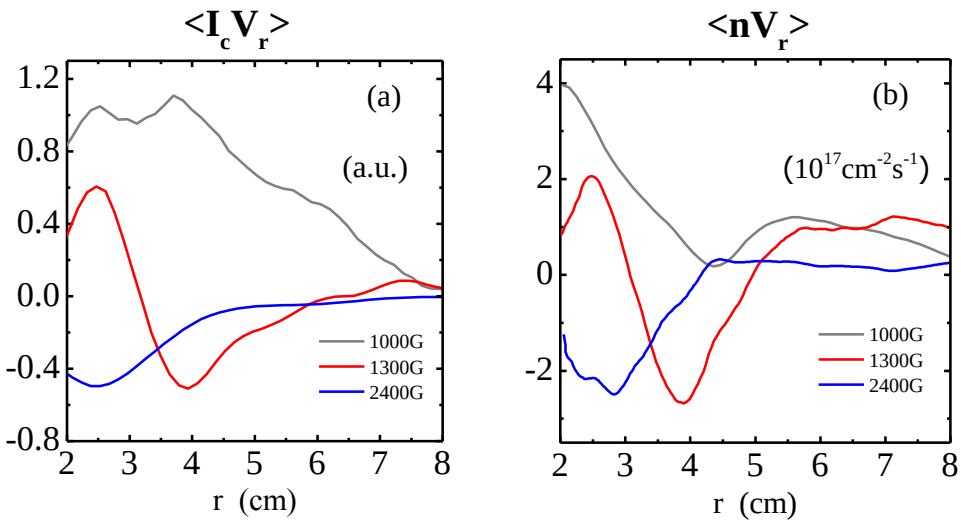

Figure 3-10 Observation of inward flux by both fast camera and Langmuir probe: (a) Intensity flux $\langle \tilde{I}_c \tilde{V}_r \rangle$ (b) turbulent particle flux $\langle \tilde{n} \tilde{V}_r \rangle$.

3.3.5 Motion of turbulent structures

To gain additional insight into the origin of the up-gradient flux we use a conditional averaging approach to analyze probe data. When the instantaneous fluctuating positive density excursion $\tilde{n}$ exceeds one standard deviation σ_n at time τ, a *positive density fluctuation* event is considered to have been triggered. Similarly, the *negative density fluctuation* events are with a trigger of one negative standard deviation $-\sigma_n$. We record the fluctuating azimuthal electric field of each event, and

then compute the radial profile of the average effective radial E×B propagation velocity V_r^{eff} of the sampled positive and negative fluctuation events. The results, radial velocity profile for positive (negative) density fluctuation events are shown in Figure 3-11(a) for B = 1300G. As we can see in the region of up-gradient particle flux (denoted by the red shaded region in Figure 3-11) we observe *positive density fluctuation propagate inwards*, against the density gradient. While *negative density fluctuation propagate outwards*, down the gradient across the region of $3 < r < 5$cm, where the total net fluctuation-driven particle flux [red dash line in Figure 3-10(b)] is negative. This structure motion is precisely opposite to the expectation for blob/hole dynamics associated with density gradient relaxation [70], and is only observed when and where the turbulent flux is inward. For locations and conditions where we observe outward average fluxes we find the usual blob/hole relaxation dynamics expected from theory [71,72]. The ratio between the sum of the flux carried by the density fluctuations with amplitudes larger than one standard deviation [black solid squares in Figure 3-11(b)] and the total particle flux measured directly by probes [red dash line in Figure 3-11(b)] can be as large as 80%, showing that these structure dynamics are clearly material to the total turbulent flux and results in a steepening of the mean density gradient which has been observed in Figure 3-4(a). Clearly then the inward flux is associated with some a driving force that affects the dynamics of turbulent structures in the intermediate region $3< r < 5$ cm. In the next chapter, we take up a study of what mechanism might lead to this behavior.

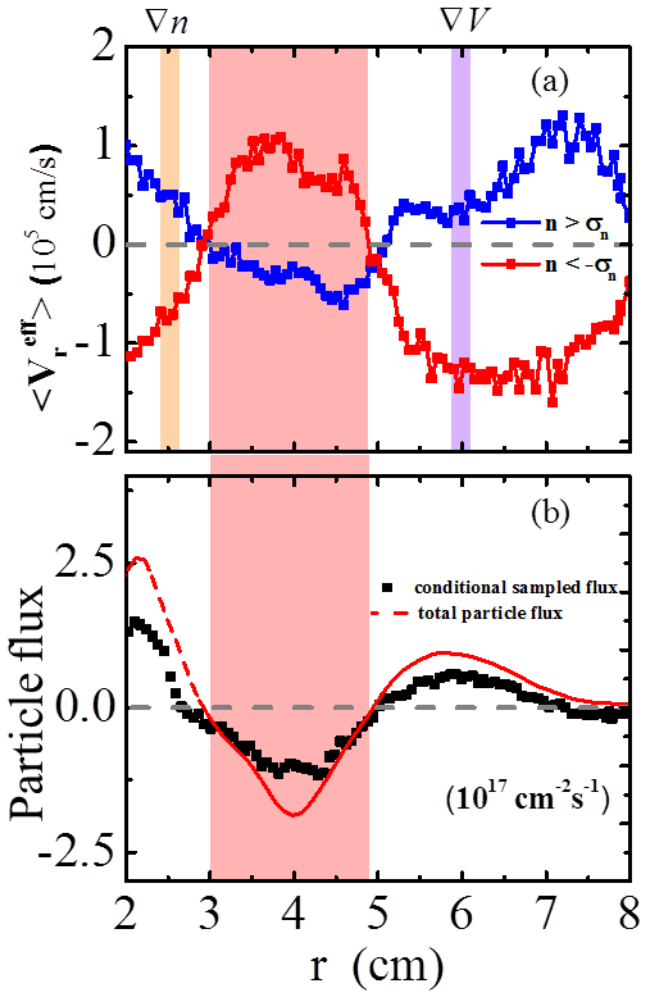

Figure 3-11 (a) Radial velocity profiles for blobs (blue solid diamond) and holes (red solid diamond). (b) The sum of contribution of blobs and holes with amplitudes larger than one standard deviation to the particle flux (Black solid squares) and total particle flux (Red dash line). B = 1300G. [82]

3.4 Summary and Discussion

The above experimental results confirm the existence of the up-gradient inward particle flux using two independent diagnostic measurements the Langmuir probes and imaging. From Langmuir probes, it has been observed that as the magnetic field is increased, the plasma develops two velocity shear layers that sit on either side of the density gradient maximum, and in the region between the maximum density gradient and outer shear layer, a net inward flux is observed to develop. Conditional averaging analyses show that the bulk (80%) of the up-gradient flux is carried by large amplitude (exceeding one standard deviation) positive (negative) density perturbations that move up (down) the density gradient, which is not expected according to blob/hole dynamics associated with density gradient relaxation. Correlation analysis between ion saturation current and intensity fluctuations shows that the light intensity fluctuations are associated with plasma density fluctuations. As seen in high-speed camera movies, in the region where we observe an inward particle flux from probe measurements the high intensity fluctuation structures (which correspond to turbulent density structures) propagate inwards in both radial and azimuthal directions. In addition, for a better comparison we calculated the intensity flux which presents the time-averaged total light intensity fluctuations moving in radial direction, similar to the turbulent particle flux measured by probes. As a result, the intensity flux and particle flux evolution with magnetic fields show a nice agreement on inward flux at high magnetic fields.

In the usual picture of the collisional drift wave-zonal-flow system, the mean density gradient is considered to be the only free energy source and leads an outward particle flux trying to flatten the gradient. The shear flow, which in such a system is driven by the fluctuations, acts to extract energy from the drift waves and thus plays a role in the nonlinear saturation of the fluctuation amplitude. However, the shear flow itself is not considered as a possible free energy source. In the experiments reported here, the inward flux seems to be associated with the development of a sufficiently strong velocity shear as the magnetic field is increased, suggesting possible link between the flow and inward flux. Motivated by these observations, we take up a detailed study of the relationship between the sheared flow and the turbulent inward particle flux in the next chapter.

Chapter 3, in part, has been accepted for publication of the material as it may appear in "Up-Gradient Particle Flux in Drift wave- Zonal Flow Systems", L. Cui, G. R. Tynan, P.H. Diamond, S.C. Thakur and C. Brandt, Phys. Plasmas, 2015. The dissertation author was the primary investigator and author of this paper.

Chapter 4

Examination of the link between flow shear and the development of inward particle flux

4.1 Introduction

Both Langmuir probes measurements and fast imagining camera measurements show the onset of an up-gradient inward turbulent particle flux in a cylindrical plasma device when density-gradient driven collisional drift waves generate a sufficiently strong radially sheared azimuthal zonal flow in a cylindrical magnetized plasma. Previously published results have shown that at moderate magnetic fields the plasma develops coherent, finite amplitude collisional drift wave fluctuations in the region around the density gradient maximum. Then, as the magnetic field is increased further, the plasma develops two velocity shear layers that sit on either side of the density gradient maximum [21,46]. At the outer shear layer the turbulent stress does work on and sustains the shear flow against dissipation, consistent with earlier results [47-51,55,69,73] and under some conditions, in the region between the maximum density gradient and outer shear layer, a net inward flux

is observed. Figure 4-1 shows the mean radial profiles of (a) equilibrium density, (b) floating potential and (c) azimuthal velocity.

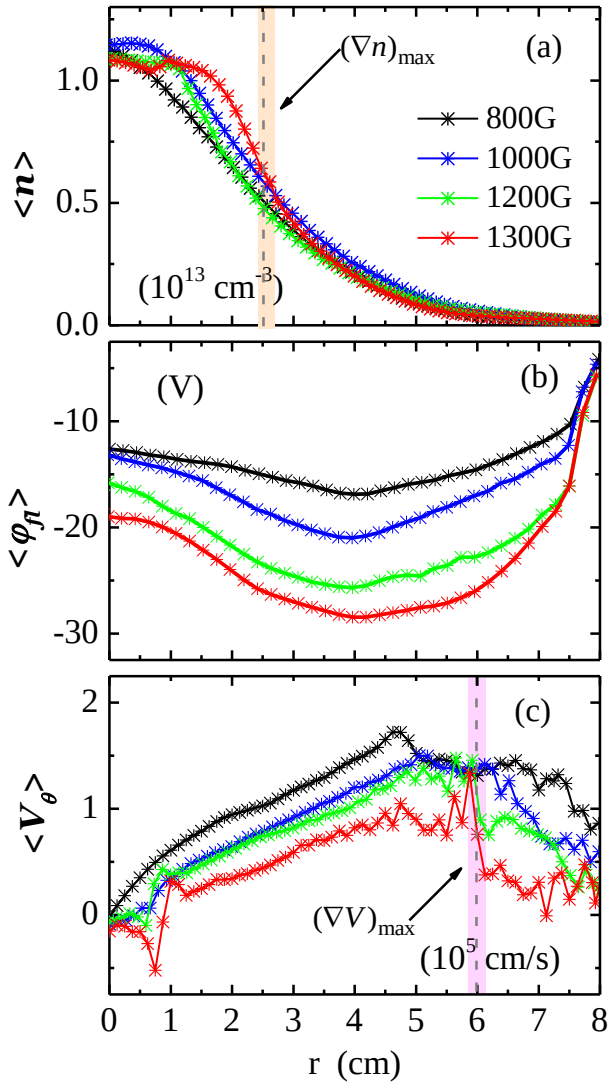

Figure 4-1 Time-averaged radial profiles of (a) mean density $\langle \boldsymbol{n_o} \rangle$, (b) floating potential and (c) mean azimuthal velocity $\langle \overline{\boldsymbol{V}}_{\boldsymbol{\theta}} \rangle$.

4.2 Experimental studies of the relationship between shear flow and inward flux

4.2.1 Fluctuation-flow energy transfer reverses

The obvious question then arises: what drives the particles go against the density gradient? In our machine, one of the free energy sources is the mean density gradient, which will lead a diffusive particle transport down the gradient; the other is the strong velocity gradient. The measurements suggest a link between the zonal flow and the up-gradient particle flux.

In order to determine if there is a link between the shear flow and up-gradient flux, we examined the rate of work done by the turbulence on the azimuthal flow and parallel flow given by the poloidal Reynolds work done by turbulence on the azimuthal flow, which is defined by Eqn. (1.20), $P_\theta = F_\theta \bar{V}_{ZF} = -\frac{\partial \langle \tilde{v}_\theta \tilde{v}_r \rangle}{\partial r} \bar{V}_{ZF}$ and the Reynolds work done by the parallel flow, which is given by $P_\parallel = F_\parallel \bar{V}_{ZF} = -\frac{\partial \langle \tilde{V}_r \tilde{V}_z \rangle}{\partial r} \langle \bar{V}_z \rangle$. Here a positive value of turbulent Reynolds work indicates that the fluctuations are driving the large-scale flow, while a negative value shows the fluctuations are extracting kinetic energy from the large-scale, low-frequency flow. An examination of the radial profile of the Reynolds work provides a key insight into the origin of the inward particle flux. Figure 4-2 (a) shows the radial profiles of turbulent particle flux from 1000G to 1300G. Figure 4-2 (b) shows the radial profile of azimuthal Reynolds work. As shown in Figure 4-2 (b), at the outer shear layer region 5

$< r <$ 6.5cm, the fluctuations do work on the shear flow, consistent with an interpretation in which the turbulence drives a zonal flow as described in earlier work [9,47]. However, in conditions and locations where the inward turbulent particle flux is observed we find that the Reynolds work is negative, indicating that the shear flow is driving the higher frequency fluctuations at this location. Thus the up-gradient flux occurs when and where the shear flow drives the fluctuations. Similar evolution of parallel Reynolds work has been observed in Figure 4-2 (c), that in the condition and radial location where the inward flux is observed, the parallel Reynolds work is negative which indicates the parallel flow is driving the fluctuations. We also notice that the parallel Reynolds work is nearly an order of magnitude smaller than the azimuthal Reynolds work. Thus the azimuthal sheared flow appears to dominate the drive of high frequency fluctuations in the regions and conditions when the up-gradient flux is observed. This result provides further support for the conjecture made in the previous chapter that the shear flow is associated with the up-gradient particle flux.

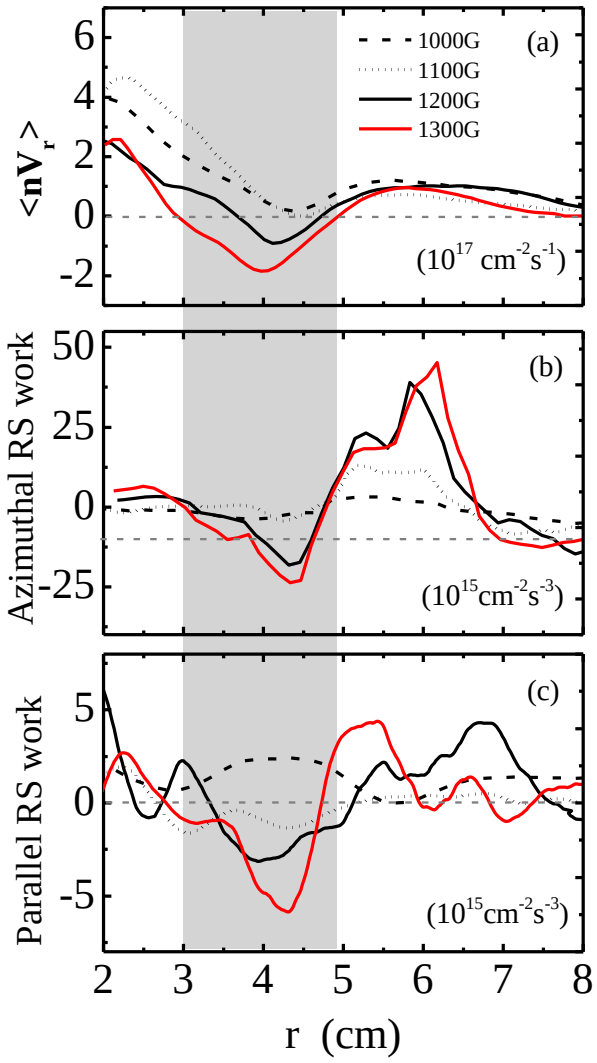

Figure 4-2 Time-averaged radial profiles of (a) turbulent particle flux $\langle \tilde{n}\tilde{V}_r \rangle$, (b) mean total azimuthal Reynolds work $-\frac{\partial \langle \tilde{V}_r \tilde{V}_\theta \rangle}{\partial r} \langle \overline{V}_\theta \rangle$ and (c) mean total parallel Reynolds work $-\frac{\partial \langle \tilde{V}_r \tilde{V}_z \rangle}{\partial r} \langle \overline{V}_z \rangle$.

4.2.2 Examination of causality

The results above show that there is a spatial correlation between the region where the flow does work on the fluctuations and the region of inward particle flux, as well as a correlation in the condition for an up-gradient flux suggesting a link between flow shear and inward flux. However, this alone is not sufficient to demonstrate that the shear flow is responsible for, or causes, the up-gradient flux. To test if there is such a causal link between the sheared azimuthal flow, the parallel flow and the inward flux, we examine if there is a statistical relationship between the fluctuations of the azimuthal and parallel flow velocities and the fluctuations in the inward up-gradient flux. We have done this by computing the cross-correlation between fluctuations in the azimuthal shearing rate and turbulent particle flux, $\mathrm{Corr}\left(\bar{V}_\theta', \Gamma_{particle}\right)$ and the correlation between the parallel velocity and turbulent particle flux $\mathrm{Corr}\left(\bar{V}_z, \Gamma_{particle}\right)$ at r = 4.8 cm, located in the outermost region of the zone of up-gradient flux. The results [Figure 4-3 (a) and (b)] show that indeed both azimuthal sheared flow and parallel flow are correlated with inward particle flux (peak correlation of ~ 0.3, well above the noise level of ~ 0.05) with a finite time delay (~ 18 μs), indicating that a transient increase in the azimuthal and axial shear flow rates is followed by a subsequent increase in the inward-directed fluctuation-driven particle flux. If we plot an envelope of the cross correlation between azimuthal velocity shearing rate and turbulent particle flux shown in Figure 4-4, we'd find the width of the envelope of the correlation function is about 0.3 ms. This 0.3-ms envelope gives a characteristic timescale of a few kHz, which as we show below is consistent with the

time-scale of the fluctuations associated with the up-gradient particle flux as we observed. Thus a causal relationship exists between the velocity flow shear and up-gradient particle flux and based upon the rates of Reynolds work estimated above, the azimuthal flow would appear to be predominantly responsible for the up-gradient flux.

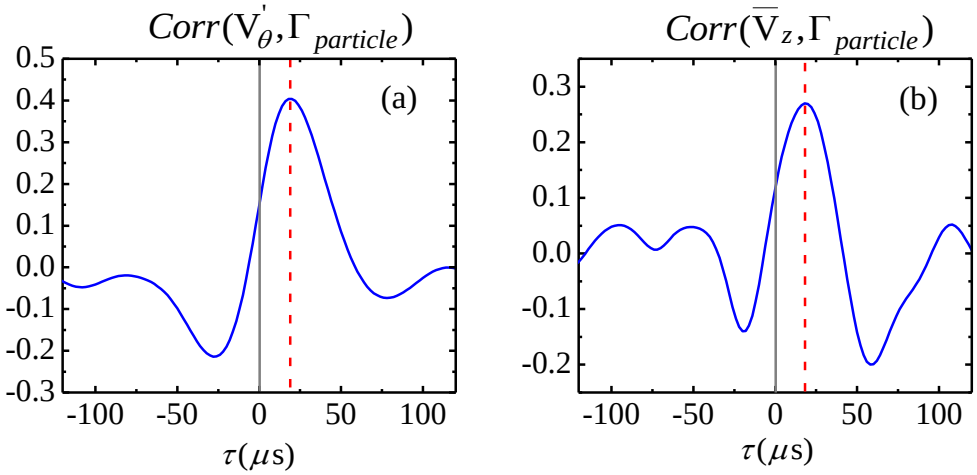

Figure 4-3 Causality: (a) Cross correlation between azimuthal velocity shearing rate and turbulent particle flux and (b) Cross correlation between mean parallel velocity and turbulent particle flux at r = 4.75cm, B = 1300G.

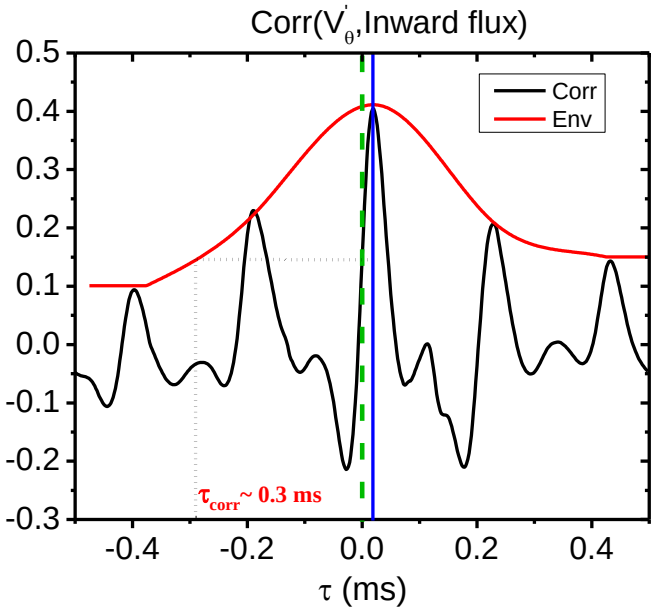

Figure 4-4 Envelope of cross correlation between azimuthal velocity shearing rate and turbulent inward particle flux.

In addition, if we plot the correlation between azimuthal flow velocity and parallel flow velocity as shown in Figure 4-5, which indicates that the two quantities have a significant correlation with almost zero time delay. Thus a burst in azimuthal shear flow is accompanied by a simultaneous burst in parallel flow.

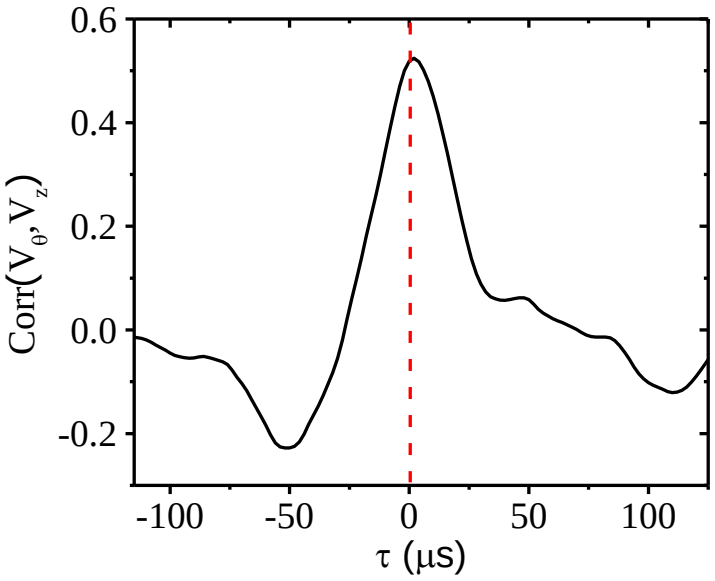

Figure 4-5 Cross correlation between azimuthal velocity shearing rate and parallel velocity at r = 4.75cm, B = 1300G.

4.3 Study of nonlinear flow-fluctuation energy transfer in frequency domain

The foregoing results show that the azimuthal shear flow is primarily responsible for driving the up-gradient particle flux. We further explore this link between shear flow and up-gradient flux by considering the frequency-resolved flux Γ_{turb} computed from data using Eqn. (1.26). At position r = 4.5cm, the inward flux

is due primarily to fluctuations at ~ 5 kHz [Figure 4-6 (a)] while at r = 6cm, the outward particle flux is also carried primarily by ~5kHz fluctuations [Figure 4-6 (b)].

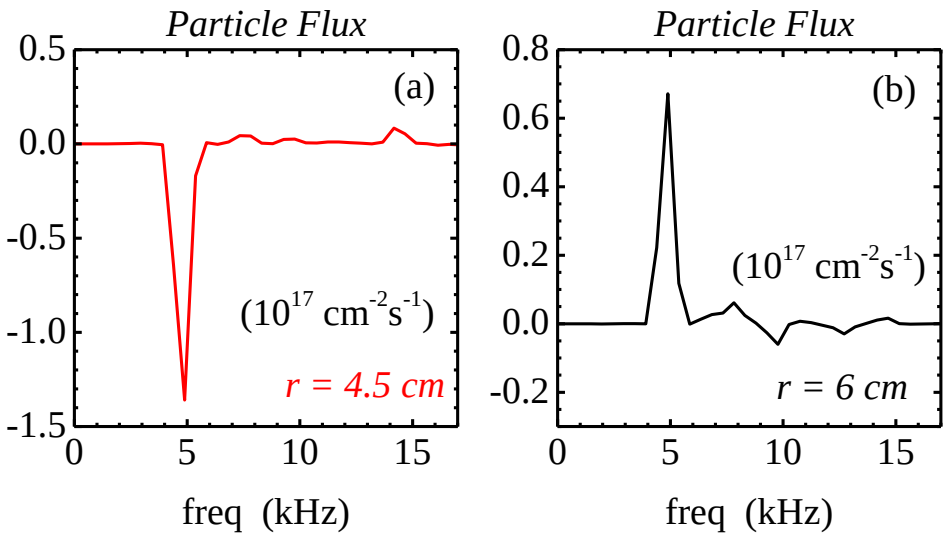

Figure 4-6 Frequency-resolved turbulent particle flux for B = 1300G at different radial position. (a) r = 4.5 cm corresponding to a net inward particle flux location (b) r = 6 cm corresponding to the location of the shear layer.

According to Eqn. (1.26), the cross-phase between density and potential fluctuations is the only quantity that can be responsible for the change of sign of particle flux. Therefore, the correlation between the shearing rate and inward flux (refer to Figure 4-3 (a)) shows that the shear flow is responsible for the up-gradient inward particle flux. Thus the velocity shear evolution must be accompanied by changes in the cross-phase between density and potential fluctuations, resulting in a

change of direction of particle transport. In Figure 4-7, we show the radially resolved cross-phase for B = 1000 G and B = 1300G two conditions. In this figure, for clarity we have isolated the frequency band around 5 kHz, which is predominantly responsible for the turbulent particle flux across the whole profile. We can see that at low magnetic field B = 1000G the cross-phase between density and potential fluctuates is between 0 and π, which gives rise to an *outward-transport* particle flux at all the radii. At higher magnetic field B = 1300G, we find the cross-phase change from positive to $[-\pi, 0]$ at $3 \leq r \leq 5\text{cm}$, exactly the same region where we observe the *inward-transport* particle flux. Thus the cross-phase for this frequency band that dominates in an inward particle flux shows a change in it is associated with the shear flow evolution.

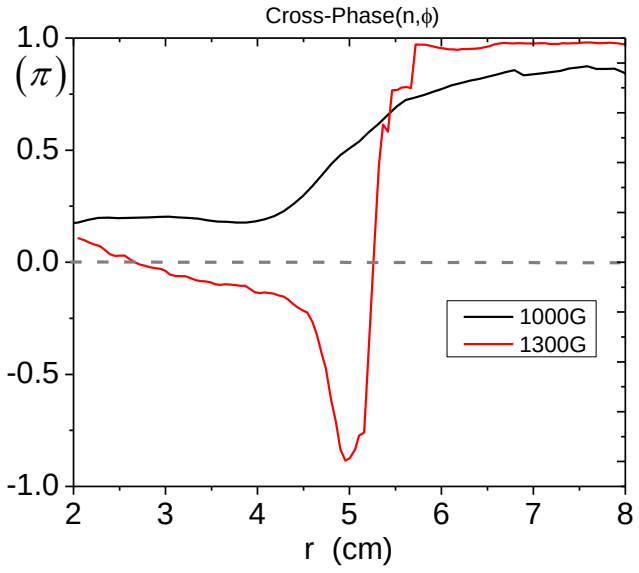

Figure 4-7 Radially resolved cross-phase between density and potential for 4-6 kHz fluctuations at B = 1000G and B = 1300G.

The Reynolds work results discussed earlier, which were obtained by time-domain analysis, show that the direction of energy transfer between the turbulence and the shear flow changes as the up-gradient flux develops. Thus it would be useful to examine this evolution further in the Fourier domain. This can be accomplished by using cross-bispectral analysis techniques to examine the frequency-resolved kinetic energy transfer $T_u(f) = \sum_{f_1} T_u(f, f_1)$, where $T_u(f, f_1) = -R_e\langle \tilde{u}_f^* \cdot (\tilde{u}_{f_2} \cdot \nabla)\tilde{u}_{f_1} \rangle$, $f_2 = f - f_1$ and $\tilde{u}_f$ denotes the Fourier-transformed fluctuating **E×B** velocity estimated from the probe array, using previously developed technique introduced in Chapter 2 [48,63]. Here a positive (negative) value of $T_u(f)$ indicates that kinetic energy is being nonlinearly transferred into (out of) the frequency f due to phase coherent interactions with fluctuations at f_1 and $f - f1$. Examining the net kinetic energy transfer rate at r = 4.5cm and r = 6cm respectively, the results are shown in Figure 4-8 for r = 6cm and Figure 4-9 for r = 4.5 cm. We find that at r = 6 cm, where the shearing rate is largest, the higher frequency fluctuations (f > 10 kHz) are *losing energy* to the low-frequency shear flow (f ~ 0 kHz) and to the 5 Khz fluctuations. This result is qualitatively consistent with earlier results in CSDX which show that the sheared azimuthal flow is associated with and sustained against dissipation by the turbulence, and thus appears to be a fluctuation-driven sheared zonal flow. At the intermedia region r = 4.5cm, where the net particle flux is negative, the frequency region from several kilohertz up to 12 kHz (including the up-gradient flux at f = 5 kHz) is gaining energy from the low frequency (f < 1-2 kHz) sheared flow. Thus the fluctuation-driven shear flow at ~ 6cm acts to drive finite frequency fluctuations at

smaller radii which in turn drive the inward particle flux. At f ~ 5kHz, fluctuations in the region between the density gradient maximum and outer velocity shear layer associated with the inward particle flux receive energy from the shear flow, and they act to steepen the mean density gradient as seen in Figure 4-1 (a). The velocity and density fluctuations are phase-coherent (since the cross-bispectrum does not vanish) resulting in nonlinear kinetic energy transfer and a finite time-averaged fluctuating particle flux. It is also noted from Figure 4-9 that the zonal flow is losing energy to turbulence due to some nonlinear damping process, indicating the possible existence of tertiary KH instability [9].

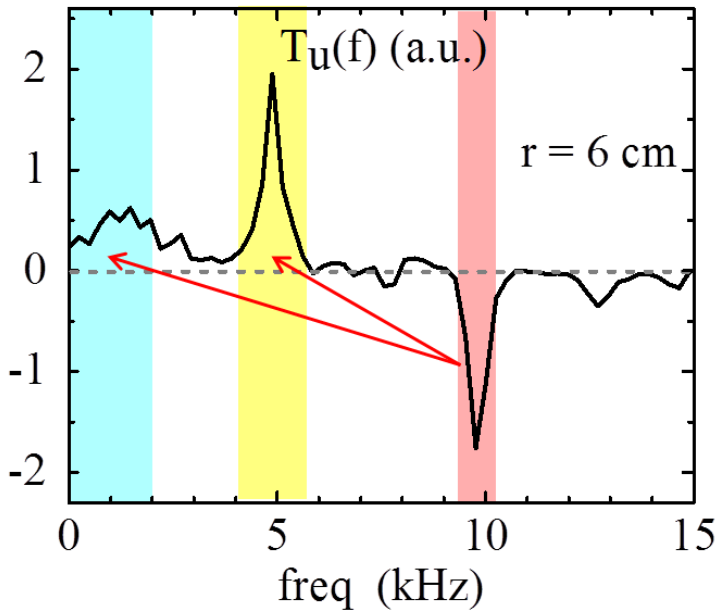

Figure 4-8 Total net kinetic energy transfer rate for B = 1300G at r = 6cm. Here a negative value means that frequency f is losing energy and a positive value means that it is gaining energy. [82]

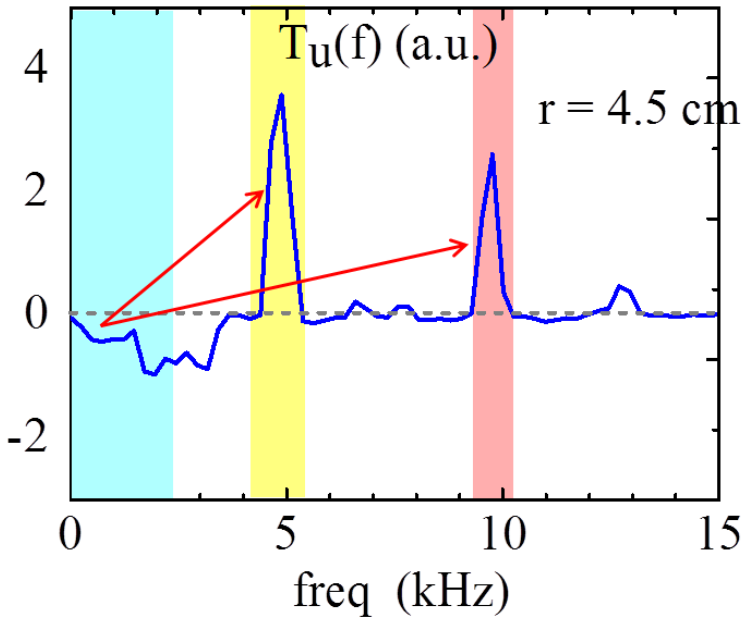

Figure 4-9 Total net kinetic energy transfer rate for B = 1300G at r = 4.5cm [82]

These above results show that the up-gradient, inward particle flux is primarily carried by f = 5 kHz fluctuations. Thus we filtered the camera movies to show the motion of structures at f ~ 5 kHz only to more clearly elucidate the up-gradient flux phenomena. The results are shown in Figure 4-10, which was obtained from sequential framed from the high-speed camera at a magnetic field of B = 1300G where we observed an inward flux from probe measurements. The snapshots shown here were taken at the same operation parameters as the probe measurement described previously in this dissertation. The two black dash circles (3 < x< 5cm) correspond to the region of radial inward particle flux as measured by Langmuir probes. Examining Figure 4-10 carefully, we observe that the motion of bright structure, which corresponds to a high density fluctuation in probe signal, contains an inward radial component in addition to the azimuthal component in the region of the black dash circles and these

high density regions tend to spiral inwards, consistent with the existence of the up-gradient flux in the region and the dynamics illustrated by the earlier frame-by-frame broadband fluctuation images.

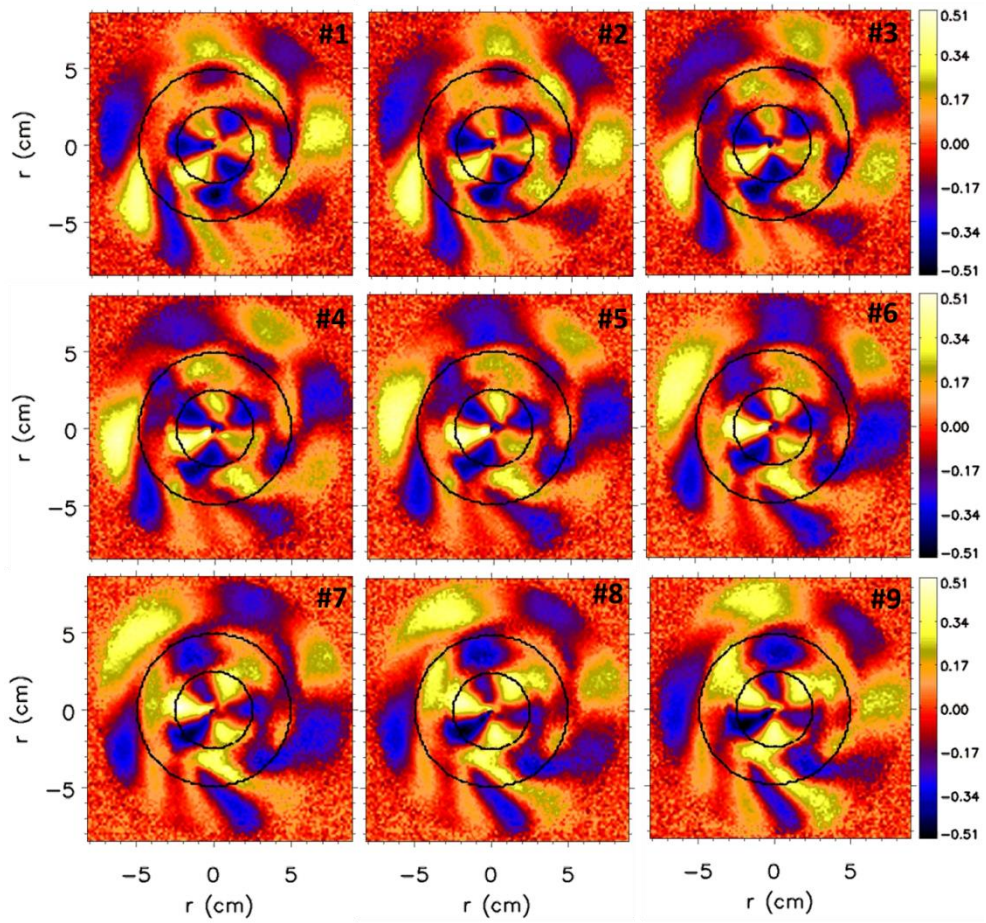

Figure 4-10 Filtered at f = 5 kHz, sequential visible light emissions images at B = 1300G. Radii of r = 3 cm and r = 5 cm are denoted by the two dashed circles.

4.4 Discussion

The above experimental findings can be summarized with the schematic shown in Figure 4-11. In configuration space, the maximum density gradient is located at the inner region of plasma, and drives fluctuations corresponding to the intermediate wavenumber drift turbulence scales. The maximum shearing rate is located outside of this region and has its kinetic energy concentrated in the low-k region. Between these two spatial locations there is a net inward particle flux. Examining kinetic energy transfer in *k*-space at two representative radial locations we find the region of shear layer formation region (denoted by the red circle) is associated with an outward flux, and in the Fourier domain kinetic energy is nonlinearly transferred from turbulent scales to low-frequency (and thus large scales) as denoted by a solid red arrow in the figure via the usual turbulent-driven zonal flow process. In the spatial location with inward flux (denoted by the black circle), kinetic energy is transferred from the low-k large-scale shear flow to higher-k turbulent scales (solid black arrow). The up-gradient particle flux occurs when and where the sheared flow nonlinearly performs work (presumably by some sort of shear layer-turbulent structure interaction) on the fluctuations and thereby enable this non-diffusive transport in a manner that is reminiscent of the up-gradient transport in other systems experiments [22,33-37].

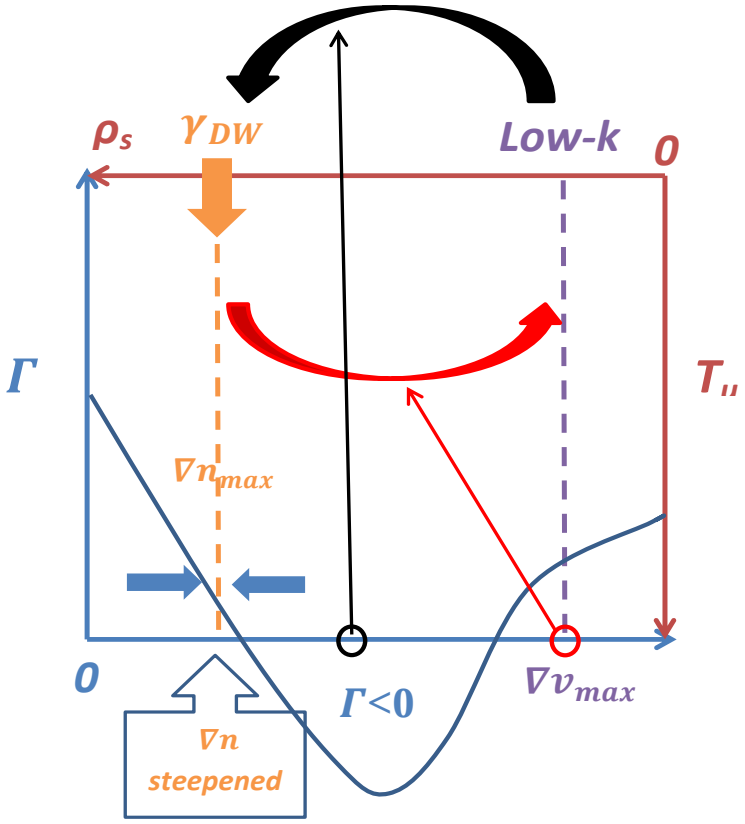

Figure 4-11 Schematic view of energy transfer in *k-space* and turbulent particle flux in configuration space.

4.5 Summary

In summary, we have investigated the role of sheared flows plays in the development of up-gradient inward particle flux. The correlation between shearing rate and inward flux demonstrates the causality that the flow is responsible in driving particle flux. The turbulent Reynolds work in time domain and frequency resolved net kinetic energy transfer in bispectrum show that when and where the inward flux is observed, the fluctuations are gaining energy from the zonal flow. We found that the 5 kHz fluctuations are dominant in inward particle transport. Therefore, we conducted a frequency resolved movie that shows the 5 kHz fluctuation move inwards.

The DWT-ZF system is thought to be well described by the Hasengawa-Wakani model [9,12]. Thus in the final part of this dissertation, we study this model to determine if the seeds of this physics mechanism can be found in the coupled drift wave-sheared flow system.

Chapter 4, in part, has been accepted for publication of the material as it may appear in “Up-Gradient Particle Flux in Drift wave- Zonal Flow Systems”, L. Cui, G. R. Tynan, P.H. Diamond, S.C. Thakur and C. Brandt, Phys. Plasmas, 2015. The dissertation author was the primary investigator and author of this paper.

Chapter 5

Study of underlying physics mechanism for inward particle flux in a multi-instability plasma system

5.1 Introduction

In Chapter 3 and 4, the detailed identification of the net inward up-gradient particle flux and its possible link to flow shear observed in the experiments has been documented. It has been known that the various free energy sources can drive corresponding linear instabilities that can be characterized by their radial location and the parameters that give rise to the instabilities, e.g. the density gradient for DW, ion temperature gradient for the ITG and velocity shear in case of the K-H. For example the usual drive for collisional drift wave is ∇n which causes only an outward particle flux. In order to obtain a net inward particle flux, a relaxation mechanism for other mean gradient is required. In quasilinear theory the crucial challenge to generate an up-gradient net particle flux lies in identifying a mechanism or mechanisms that yield a strong enough inward flux so as to overcome the outward diffusive transport inward pinch. As we show here, high field operations in CSDX-U create a multi-instability

system with coexistence of ∇n , ∇T_e , ∇T_i , ∇V_θ and $\nabla V_\parallel$. Experiments on CSDX have shown that the magnetic field strength is an important control parameter governing the development of turbulence. This effect is attributed to the reduction of ion-ion collisional viscosity $\mu_{ii} \propto \rho_i^2 \nu_{ii} \propto \frac{1}{B^2}$ that occurs at higher magnetic fields.

In this chapter, we will examine the possible candidates that are responsible for the net inward up-gradient flux.

5.2 Fluctuation power spectra in CSDX-U

In Figure 5-1 we show the spectrograms of the density (a1) to (e1) and potential (a2) to (e2) fluctuations as the magnetic field is increased from B = 400G to B = 1500G. In addition, in columns 1 and 2 the time-averaged radial profiles of plasma density and floating potential are indicated by the white line superimposed on each spectrogram. Note that magnetic field steps are non-uniform. The spectrograms are calculated by windowed fast Fourier transforms. For low B fields (B < 1200G), spectra are dominated by several discrete modes over a weak broadband background. Both density and potential fluctuations peak at the location of the density gradient and have similar frequency components with comparable intensity. With increasing B (up to ~1200G), these modes grow and nonlinearly interact to broaden the spectra and reach a state of weakly developed turbulence. This is reminiscent of previous results from CSDX (with a smaller source and maximum magnetic field of 1000G), where these have been identified as nonlinearly coupled drift interchange modes [46,75], as well as with the identification of collisional drift waves in a 15cm diameter source

equipped with a m=0 antenna operating at 900G, in conditions very similar to those reported here [61]. Figure 5-1 (*a*3) to (e3) show the cross-phase between density and potential fluctuations. From B = 400G to roughly 1100G the cross-phase profiles look very similar. The cross-phase between density and potential fluctuates is small in the region around the mean density gradients (r = 1–6 cm)- a standard signature of DWs [18], while at the edge the cross-phase is between [$\pi/2, \pi$]. From B = 1200 to 1500G, this region of large potential fluctuations with cross-phase of [$\pi/2, \pi$] expands from the edge toward the center. The cross-phase goes up to π at the threshold ($B \sim$ 1400G), consistent with signatures of the K–H instability [18].

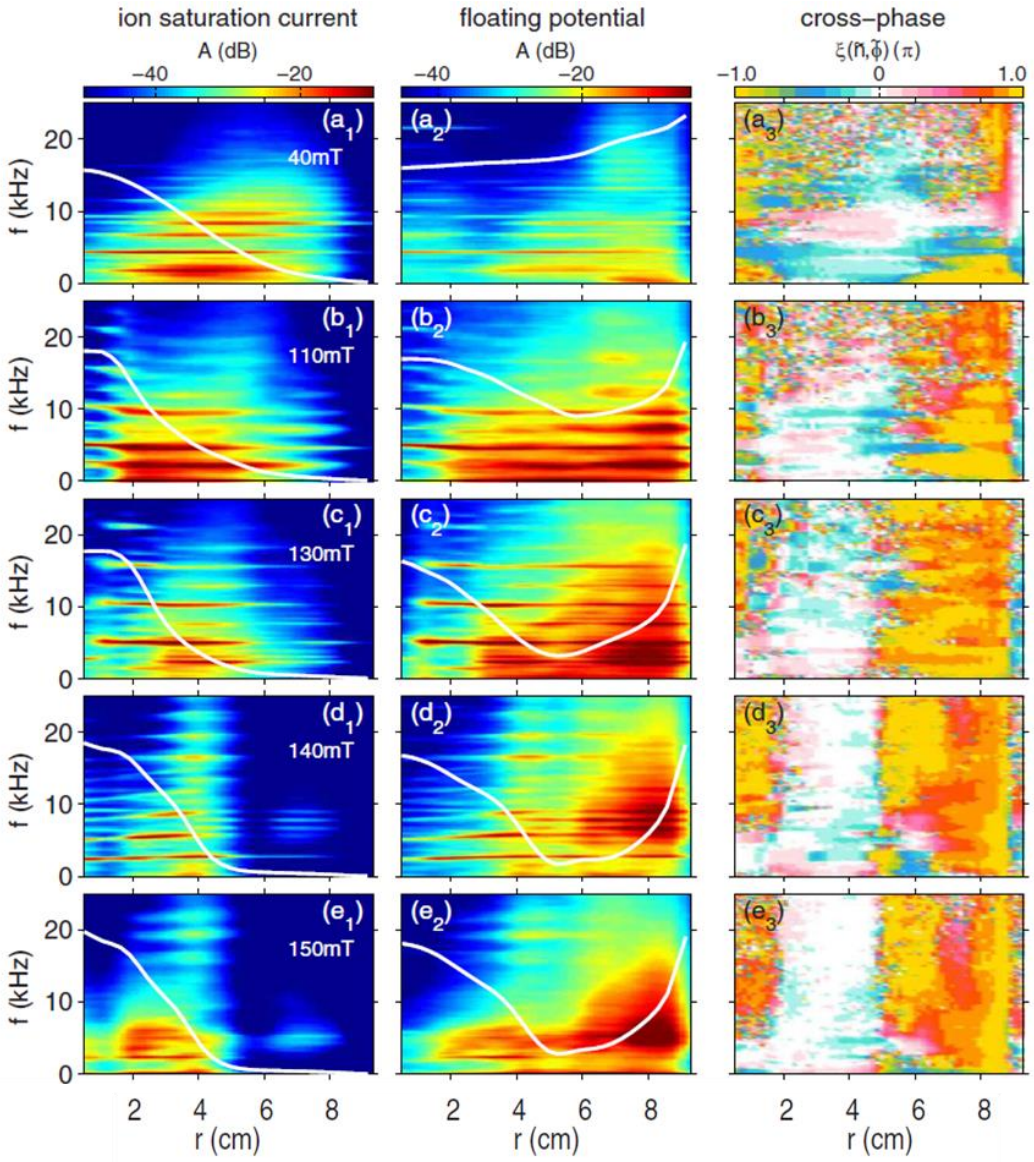

Figure 5-1 Evolution of frequency spectra and cross-phases with magnetic field: radially resolved frequency spectra obtained from fluctuations of ion saturation current (column 1), floating potential (column 2) and cross-phase between density and potential (column 3). [21]

5.3 Flow shear-driven inward pinch

In Chapter 4, the experimental results suggested that there was a possible link between flow shear and inward flux. In order to find the underlying physical mechanism which results in an up-gradient inward particle flux, we perform a linear stability analysis on using a Gaussian fit to the experimental density and $\mathbf{E} \times \mathbf{B}$ azimuthal flow profiles obtained using the LIF measurement, which gives a more accurate flow profile than Langmuir probe). To this purpose, we use a linear, modified Hasegawa-Wakatani theory model to describe the time evolution of the coupled potential and density fluctuations shown as follows: [80]

$$\partial_t \tilde{n} + \frac{V_{E0}}{r}\frac{\partial \tilde{n}}{\partial \theta} + \tilde{z} \times \nabla\tilde{\phi} \cdot \frac{\nabla n_0}{n_0} = \frac{1}{\eta}\nabla_{\parallel}\tilde{j}_{\parallel} + \widehat{D}_n \nabla_{\perp}^2 \tilde{n} \tag{5.1}$$

$$\partial_t\left(\nabla_{\perp}^2\tilde{\phi}\right) + \nabla \cdot [V_E \cdot \nabla(\nabla\tilde{\phi}) = \frac{1}{n_0\eta}\nabla_{\parallel}\tilde{j}_{\parallel} + \mu_{ii}\nabla_{\perp}^2\nabla_{\perp}^2\tilde{\phi} \tag{5.2}$$

in the presence of the density and azimuthal flow profiles, which we take from experiments and assume to be steady in time. The model profiles used in this analysis are shown in Figure 5-2, and are based upon a fit to the relevant experimental profiles for the given magnetic fields. In this analysis finite ion temperature effects are completely neglected, to isolate the possible role of transverse velocity shear on driving the up-gradient flux, providing an initial (linear) test of the hypothesis proposed earlier in this dissertation.

From Figure 3-2, we can see that the transition from a regime with an all outward (down-gradient) particle flux to a regime with a large inward (up-gradient)

particle flux occurs as the magnetic field is raised to around 1200G. Therefore, we first perform our stability analysis on the density profiles and **E** × **B** flow profiles related to the magnetic field values 1200G (high field) to see if there is an inward particle flux in this condition. Figure 5-2(a) and Figure 5-2(b), show the density from Langmuir probe and the **E** × **B** azimuthal velocity radial profiles estimated from LIF measurement respectively. The **E** × **B** azimuthal velocity was estimated by subtracting the ion diamagnetic velocity from ion fluid velocity: $V_{EXB} = V_{ion} - V_{diam}$. The ion total fluid velocity V_{ion} is measured directly from LIF with a Polynomial fit on it. And also we can calculate ion diamagnetic velocity from density and Ti profiles as $V_{diam} = \frac{\nabla(nT_i)}{enB}$. The resulting V_{EXB} radial profiles are showing in Figure 5-2(b).

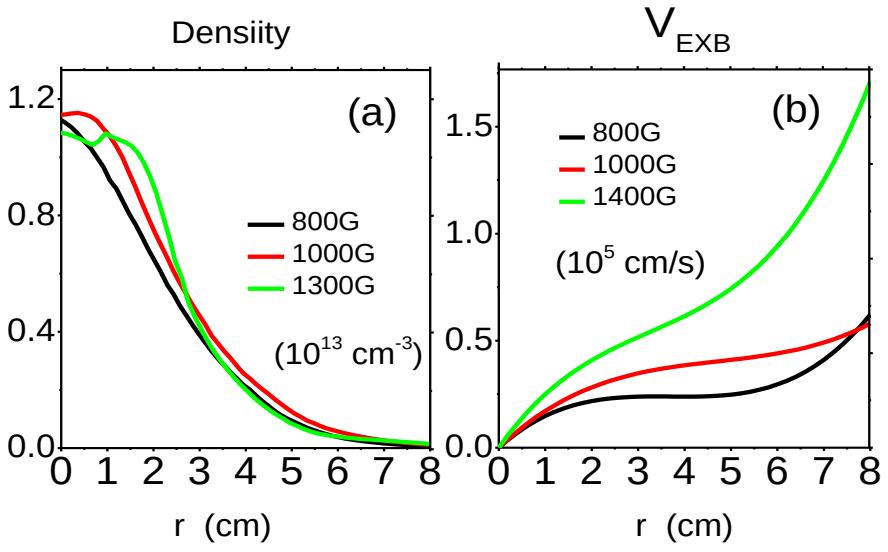

Figure 5-2 Equilibrium profiles used for linear analysis: (a) Density, (b) **E** × **B** azimuthal flow velocity from LIF measurement, obtained by fitting a Gaussian to the experimentally measured data.

Therefore, in search of an inward particle flux we examine finite $k_{\|}$ modes. Both the density gradient and the vorticity gradient can drive finite $k_{\|}$ instabilities. In the cases where the system is dominated by the density gradient or the vorticity gradient, the instabilities can have properties which are respectively more pertinent to resistive drift waves or resistive Kelvin-Helmholtz modes. Figure 5-3 shows the growth rate for finite $k_{\|}$ modes with n = 1 versus their azimuthal mode numbers, for B = 1200G. Using the experimentally measured density and E × B flow profiles in our calculations, the modes are drift wave-like, i.e. the frequencies are close to those of pure drift waves and the growth in the mode frequencies is due to the steepening of density profiles for larger magnetic fields which we see in Figure 5-2(a) (rather than the steepening of the velocity profile which resulted in higher growth rates for the pure KH modes as seen black dots in Figure 5-3). In these drift wave dominated regimes, shear flow lowers the mode frequency and growth rate and therefore has a stabilizing effect.

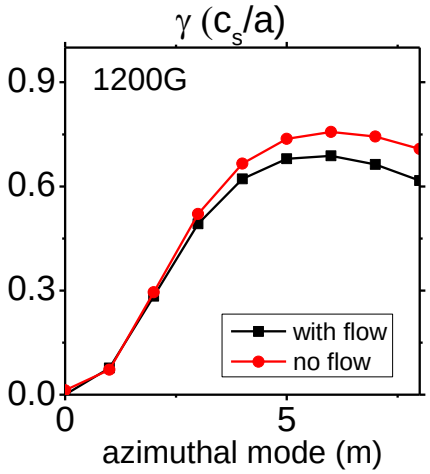

Figure 5-3 Linear growth rates for n=1 modes as a function of azimuthal mode number for B = 1200G with $\boldsymbol{V_{EXB}}$ flow (shown in black line) and without $\boldsymbol{V_{EXB}}$ flow (red line).

Figure 5-4 illustrate the calculated cross-phase of density and potential as a function of radius, at B = 1200G, for mode n = 1, m = 4, which has been observed to have the largest contribution to the inward particle flux in the experiments. The sign of particle flux is decided by the sign of the cross-phase of density and potential (refer to Eqn. (1.26)). Thus the positive value of cross-phase indicates an outward particle flux; the negative value of cross-phase indicates an inward flux. In Figure 5-4, the red dash line indicates the cross-phase for pure DWs and the black solid line indicates the cross-phase for the drift-KH modes. As we see, the cross-phase for both pure DWs and drift-KH is positive at all radii, which also means the particle flux is positive at all radius for B = 1200G, suggesting by using this 2-filed modified H-W mode could not explain our experimental finding of net inward particle flux at high magnetic fields. There must be some other mechanism for this inward flux.

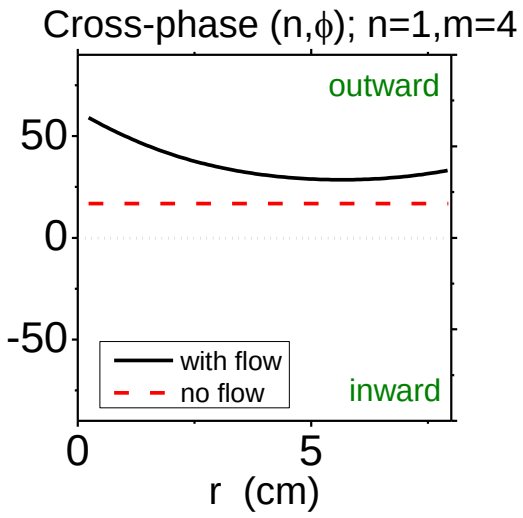

Figure 5-4 Cross phase of density and potential for n = 1, m = 4 mode with V_{EXB} flow (shown in solid line) and without V_{EXB} flow (dash line). Here a positive value in cross-phase indicates a mean outward flux and negative indicates inward flux.

5.4 Inward pinch driven by ion mixing mode mechanism

Due to the fact that a linear instability analyses using experimentally measured density and $\mathbf{E} \times \mathbf{B}$ flow profiles in a linear, modified Hasegawa-Wakatani theory model with the coupled potential and density fluctuations failed to reproduce the essential elements of our experimental observations namely the generation of an inward particle flux, we search for other free energy sources that could possibly contribute to the generation of an inward flux.

5.4.1 Evidences of Ion Temperature Gradient (ITG) instability

By using laser induced fluorescence (LIF) measurements [58], we can obtain radial profiles of azimuthal ion total fluid velocity and ion temperature. Figure 5-5 show the radial profiles of Gaussian-fitted LIF measured ion temperature $\boldsymbol{T_i}$ with error bar and mean density $\langle \boldsymbol{n_0} \rangle$ measured by Langmuir probe. As we can see from the mean density radial profiles, in the central plasma region r < 2cm, the mean density remains almost the same as we increase the magnetic field. In contrast, in the same region r < 2 cm, we observe a strong ion temperature gradient as we increase the magnetic field, with which that fluctuations associated the ion-temperature gradient could possibly be excited when $B > B_{crit} \sim 1200G$.

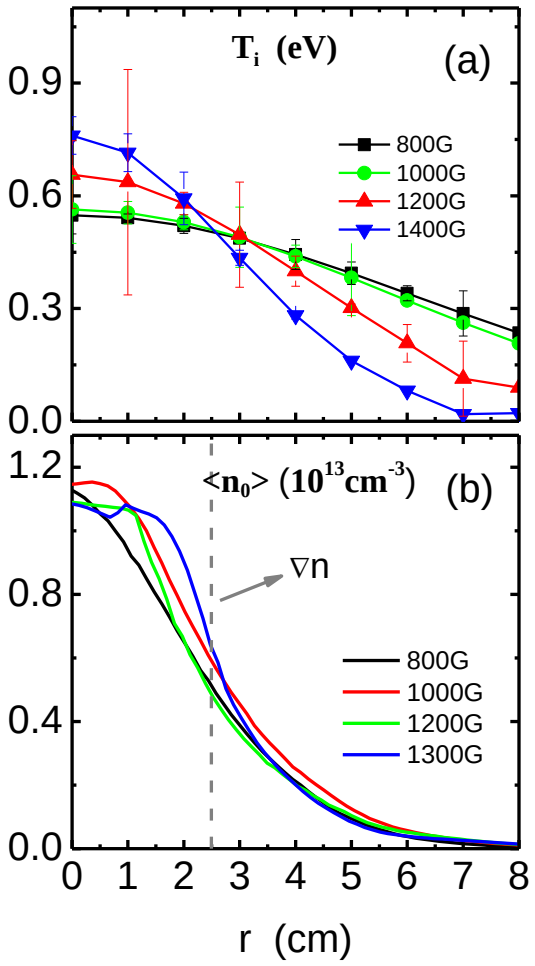

Figure 5-5 Radial profiles of (a) ion temperature $\boldsymbol{T_i}$ measured by LIF and (b) mean density $\langle \boldsymbol{n_0} \rangle$ measured by Langmuir probe.

This observation is bolstered or reinforced by noting that in Figure 3-8 in Chapter 3, we observed in the center region r < 2 cm there are structures with relatively large azimuthal mode number that propagate in counter-clockwise direction (which corresponds to the ion diamagnetic drift direction) when the inward flux was observed. Figure 5-6 shows a snapshot for movies recording light of Ar I emission at

1000G and 1400G (for movies, see supplemental files). At 1000G, the electron fluctuation features are dominant in whole plasma cross-section, propagating in electron diamagnetic drift direction. As we increase B field to above 1200G, we found the ion fluctuation features propagating in the opposite direction in the center, which coincides with the development of inward particle flux. The motions for ion/electron features for two different magnetic fields can be simplified in the cartoons below the imaging snapshots.

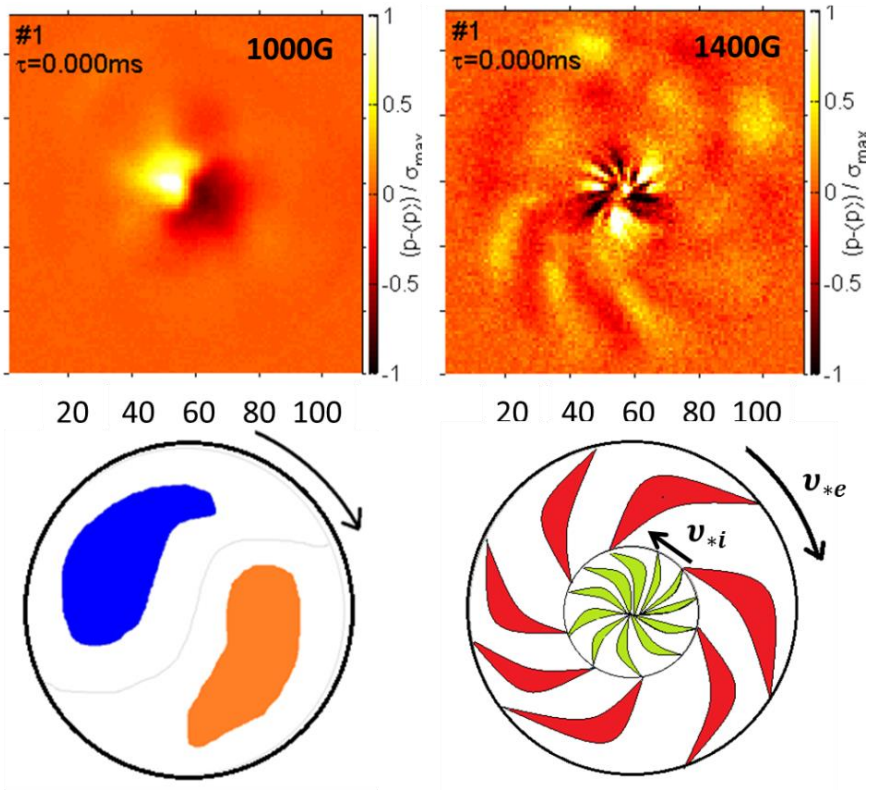

Figure 5-6 Ion and electron fluctuation features observed from fast imaging.

The development of the high azimuthal mode number counter-clockwise propagating ion fluctuations can be seen more clearly by applying a high-pass filter on the movies. The results are shown in Figure 5-7 which shows the space-time evolution of fluctuating light intensity plots at a radius of r = 1.7 cm obtained from the movie at B = 1600G. In the plot low-frequency modes ($f \sim 3$ kHz and $m \sim 1$–2) propagating in the electron diamagnetic drift direction are pronounced. In addition, fine-scaled dynamics are noticeable. If we conduct a high-pass filtering of this space–time diagram with a cutoff frequency of 25 kHz to isolate this feature, we obtain the results shown in Figure 5-7(b), showing an opposite propagation mode feature at the center of plasma where T_i steepens. This is a robust evidence of a feature propagating in the ion diamagnetic drift direction, suggestive of an ITG or some other instability associated with the ion dynamics.

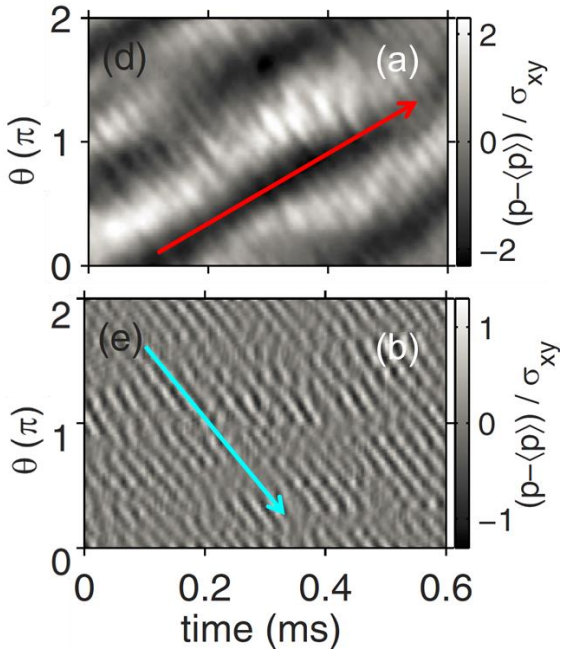

Figure 5-7 Space–time plots of normalized light fluctuations in an azimuthal circumference at r = 1.7 cm for the magnetic field B = 1600G: (a) unfiltered, (b) high pass zero phase frequency filtered with a cutoff frequency of 25 kHz. [21]

Coppi and Spight have worked out that the threshold for an ITG instability is determined by $\eta_i > 2/3$ [78], where $\eta_i = d \ln T_i / d \ln n$. While in our experiments, the data show that $d \ln T_i$ increases dramatically as B is raised, and also shows that $d \ln n$ decreases drastically as B is raised. So η_i is increased significantly. However, calling this an η_i instability is a bit misleading because our experimental density profile is nearly flat in the center region. In addition, our experiment has $k_\perp \rho_s > 1$ whereas classic η_i theory has L_n finite and $k_\perp \rho_s << 1$. A modified Hasengawa-Mima model has been developed [81] (Eqn. (5.3)-(5.5)) including parallel velocity fluctuation plus pressure gradient ($P_{i0} = nT_i$), as well as adiabatic electrons (which cannot give the

particle flux directly), but we can use this model to examine the evolution of this ITG instability with increasing in magnetic field,

$$\partial_t(\nabla_\perp^2 - 1)\tilde{\phi} + \tilde{z} \times \nabla\tilde{\phi} \cdot \frac{\nabla n_0}{n_0} + \tilde{z} \times \nabla\left(\nabla_\perp^2 \tilde{\phi}\right) \cdot \frac{\nabla P_{i0}}{P_{i0}} = \nabla_\parallel \tilde{u}_\parallel \tag{5.3}$$

$$\partial_t \tilde{u}_\parallel + \nabla_\parallel\left(\tilde{\phi} + \tilde{P}_i\right) = 0 \tag{5.4}$$

$$\partial_t \tilde{P}_i + \tilde{z} \times \nabla\tilde{\phi} \cdot \frac{\nabla P_{i0}}{P_{i0}} + \gamma \nabla_\parallel \tilde{u}_\parallel = 0 \tag{5.5}$$

By applying the experimental profiles shown in Figure 5-2 and Figure 5-5 into this model, we are able to achieve the real frequency, linear growth rates and maximum unstable mode number. Table 5-1summarized the evidence we obtained both from experimental observations and simple linear analysis for three difference conditions: 800G (weak field), 1000G (middle field) and 1200G (high field). The experimental results show that there is a big increase in ion temperature gradient length scale at 1200G where we observed a net inward particle flux. From the imaging data, we saw very clearly a transition change in mode types as the magnetic field is raised. In particular, at 800G the electron fluctuation feature clearly dominates; at 1000G a burst of ion feature starts to appear but the electron fluctuation is still pronounced in whole plasma. Finally, at 1200G, there is a robust ion fluctuation feature located in the center region where T_i steepens. By applying the experimental profiles in the simple linear model, we calculated the real frequency along with the linear growth rate for three conditions. The real frequency is negative which confirms that this is an ion mode. And the linear growth rate increases when we increase the

magnetic fields, showing the ITG mode becomes more unstable at high magnetic field. And the maximum $k_\perp \rho_s$ calculated from linear modeling is larger than 1 in our machine and roughly close the experimental observed ITG unstable mode number. We also note that this linear model neglects ion viscous damping, which will be stronger at lower magnetic fields and thus would be expected to reduce or even stabilize the system at lower magnetic fields.

Figure 5-8 shows the eigenfunction for ITG maximum growing modes (m=7-8) [81], and we can see at B ≥ 1200G the eigenfunction peaks around the same radial location, 3 < r < 5cm, where the inward flux observed. Since this modified H-M model has adiabatic electrons, it cannot have a collisional drift wave instability. Thus it cannot provide a comparison of the combined DW/ITG eigenmode with the experiment.

Table 5-1 Evidence for ITG modes excited at higher B field from both experimental observation and linear studies.

	800G	1000G	1200G
Flux	$\Gamma > 0$	$\Gamma \sim 0$	$\Gamma < 0$
Fluctuations	electron feature	bursty ion feature	robust ion features
$1/L_{Ti}$	0.16	0.18	0.25
ITG	-0.2+i 0.2	$-0.2 + i\ 0.19$	$-0.2 + i\ 0.23$
$(k_\perp \rho_s)_{max}$	4	3	2

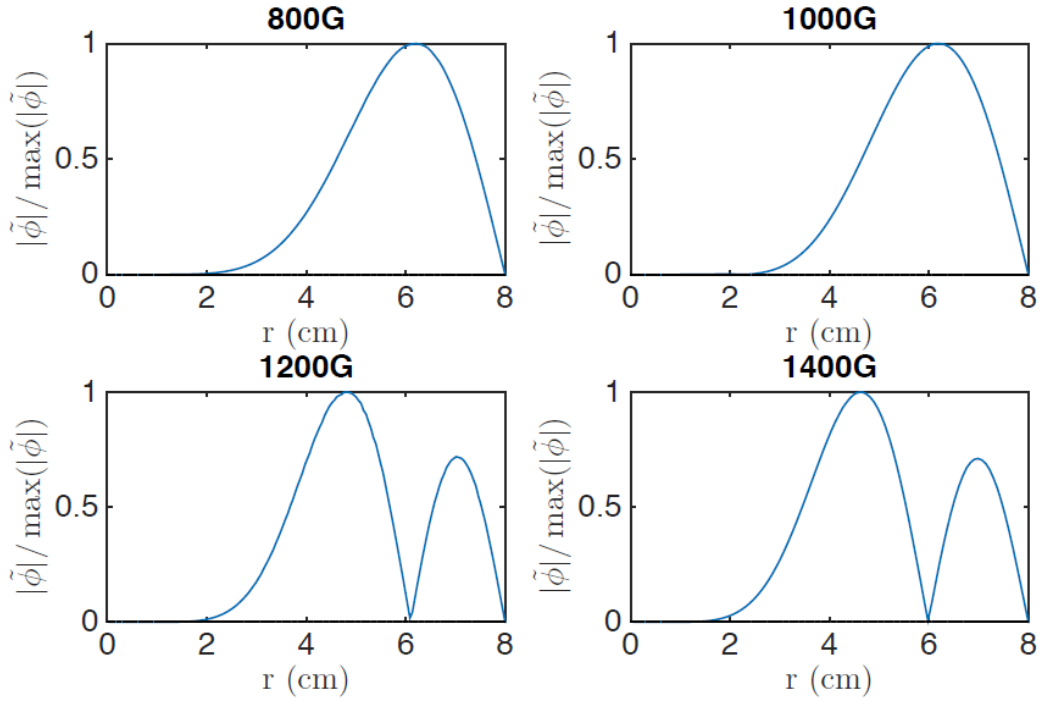

Figure 5-8 Eigenfunction for maximum growing modes (m=7-8).

5.4.2 Ion mixing mode driven inward pinch

When there is a sharp ion temperature gradient $|d \ln T / dr|$ relative to the density gradient $|d \ln n / dr|$ as shown in Figure 5-9, then the ion drift features that tend to mix the hot and cold ion populations can be excited, which is called ion mixing mode [78]. The ion mixing mode with finite electron thermal conductivity can lead to an excitation of electron temperature fluctuations which can produce a net inward particle transport of electrons.

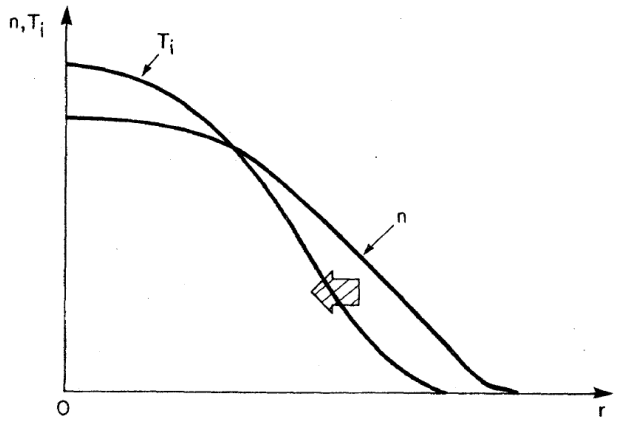

Figure 5-9 Type of ion temperature and density profiles leading to the excitation of ion-mixing modes.

Theory predicts that with the existence of ITG instability and collisional electrons, an inward pinch can be driven by thermal electron-ion mixing mode mechanism. In this case, quasilinear theory gives a particle flux shown in Eqn. (1.28) $\Gamma_{turb} = -D\nabla n + V_{pinch} n$, with diffusive coefficient D and pinch velocity V_{pinch} given as [79]:

$$D = (1+\alpha)\sum_{k} \frac{k_\theta^2 |\phi_k|^2}{\chi_\parallel k_\parallel^2} \tag{5.6}$$

$$V_{pinch} = \frac{3}{2}(\alpha+1) d\ln T_e \sum_{k} \frac{k_\theta^2 |\phi_k|^2}{\chi_\parallel k_\parallel^2} \tag{5.7}$$

where α is the thermal force coefficient. In order to have a net inward particle flux, it is required that $\frac{V}{D} < \frac{\nabla n}{n}$, thus the threshold for a net inward particle flux driven by ion mixing mode mechanism becomes:

$$\eta_e = \frac{d \ln Te}{d \ln n} > \frac{2}{3} \tag{5.8}$$

To conclusively claim that it is the ion mixing mode driven inward pinch that cause the net inward flux in our experiments, then the key element η_e > 2/3 must be satisfied, and the electron temperature gradient must occur in the same region where the other gradients are found, and where the up-gradient flux occurs. Figure 5-8 suggested that the ITG unstable mode peaks at the same region of inward particle flux. However, due to the limitation of current diagnostics for electron temperature, so far we do not have a very accurate electron temperature profile for the upgraded-CSDX. Figure 5-10 shows the equilibrium density profile and electron temperature profile from the old CSDX. Estimated η_e from these old experiments [46] obtained at B=1000G is about 0.5, which is close to this threshold value. Also we note that these old data show that the electron temperature gradient is growing steeper as the magnetic field was raised, while density gradient isn't changing so much, suggesting η_e is increasing as B is raised. Our LIF data also show that grad-Ti is increasing. Those trends very likely support our hypothesis that the mixing mode is at work here. In addition, as we can see from Figure 5-10(b), ∇T_e locates ~ 3cm. Since the old CSDX was using a smaller antenna with radius of 5cm. Our experiments were using a larger antenna with radius of 7.5cm. Thus it is reasonable to expect the new T_e profile should peak at a relatively outer region ~ 4cm. However, further work is needed to provide multiple independent diagnostic measurement of T_e profile and make that an

urgent work to confirm the role of ion mixing mode driven inward pinch in causing this net inward particle flux.

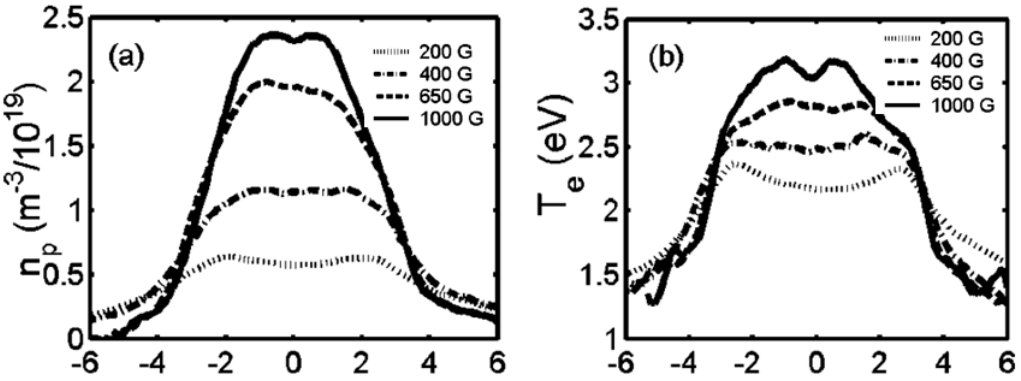

Figure 5-10 Radial profiles of old CSDX experiments: (a) Equilibrium density profiles; (b) equilibrium electron temperatures.

5.5 Inward pinch driven by parallel flow shear

Preliminary main ion parallel flow velocity measurements by LIF suggests there is a strong parallel velocity shear developed as we increase the magnetic field to 1200G where the inward particle flux starts, shown in Figure 5-11. Due to the fact that the data become very noisy out of the region r =3cm, thus we are only showing the parallel flow velocity for r < 3cm. We observe a strong parallel flow shear develops as we increase the magnetic field above 1200G.

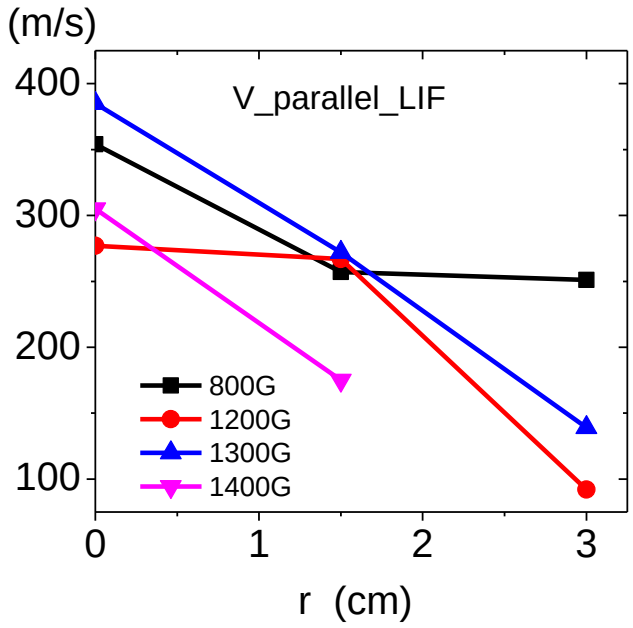

Figure 5-11 Radial profiles parallel flow velocity by LIF measurement.

Theory indicates that $\nabla V_{\parallel}$ can give rise to a negative compressibility that couples with an acoustic wave, which then drives an inward pinch:

$$J_{\parallel} = en\left(\tilde{V}_{\parallel i} - \tilde{V}_{\parallel e}\right) \tag{5.9}$$

$$\frac{\partial}{\partial t}\left(\frac{\tilde{n}_e}{n}\right) + d\ln n\,\tilde{V}_x + \nabla_{\parallel}\tilde{V}_{\parallel e} = 0 \tag{5.10}$$

$$\frac{3}{2}n\left(\frac{\partial \tilde{T}_e}{\partial t} + \tilde{V}_x\frac{d\tilde{T}_e}{dx}\right) + nT_e\nabla_{\parallel}\tilde{V}_{\parallel e} = \nabla_{\parallel}n\chi_{\parallel}\nabla_{\parallel}\tilde{T}_e = 0 \tag{5.11}$$

$$\nabla\cdot J = 0 \Leftrightarrow -\frac{d}{dt}\nabla_{\perp}^2\tilde{\phi} = -\nabla_{\parallel}\left(\tilde{V}_{\parallel i} - \tilde{V}_{\parallel e}\right) \tag{5.12}$$

$$\frac{\partial}{\partial t}\tilde{V}_{\parallel i} + \tilde{V}_x\frac{dV}{dx} = -\nabla_{\parallel}\tilde{\phi} \tag{5.13}$$

The first equation defines parallel current, the second equation is the linearized electron continuity equation, the third equation is the linearized electron heat equation, the forth equation is the charge balance equation which equates polarization current across B field with parallel current and the last one is the ion parallel momentum equation which we can solve for the parallel velocity. From Eqn. (5.9)-(5.13), the ion mixing mode–driven ∇T_epinch term and parallel flow shear driven pinch term have been worked out respectively by P. Diamond and J. Li:

$$V_{\nabla V_{T_e}} = -\frac{3}{2}\eta_e \tag{5.14}$$

$$V_{\nabla V_\parallel} = (1 + k_\perp^2 \rho_s^2)\frac{L_\parallel}{\rho_s}\left(\frac{V_\parallel}{C_s}\right)\frac{k_\parallel}{k_\theta}\eta_V \tag{5.15}$$

By taking the ratio of the two terms, we can compare which is more dominant for our experiment. The ratio of the two pinch terms is:

$$\frac{V_{\nabla V_\parallel}}{V_{\nabla V_{T_e}}} = \frac{2}{3}\frac{L_{T_e}}{L_V}\frac{L_\parallel}{\rho_s}\left(\frac{V_\parallel}{C_s}\right)\frac{k_\parallel}{k_\theta} \tag{5.16}$$

By applying CSDX parameters: $\frac{L_{T_e}}{L_V} \sim 1.5, \frac{L_\parallel}{\rho_s} \sim 2.3, \frac{V_\parallel}{C_s} \sim 0.1$ and $\frac{k_\parallel}{k_\theta} \sim 0.1$ to Eqn. (5.17), the ratio is about 0.03 for our experiments. Therefore, the preliminary linear studies suggest that the $\nabla V_\parallel$ is not as effective as ITG in driving an inward pinch in our experiments. However, this is to be explored in the future study.

5.6 Summary

This chapter has provided a first brief examination of the linear stability of these CSDX-U discharges to get an initial idea of which free energy sources may be most likely to lead to up-gradient fluxes for the conditions of our experiments. Firstly we have conducted the linear stability analyses using a linear, modified Hasengwa-Wakani model that include instability driven by both, density and vorticity gradients to test the link between flow and inward flux. We then applied the density profiles from Langmuir probe and $\mathbf{E} \times \mathbf{B}$ azimuthal flow profiles form LIF measurement and found the resulting cross-phase between the density and potential fluctuation eigenmodes for these experimental conditions. This linear stability analysis failed to reproduce change in sign of the cross-phase necessary to cause a reversal of the particle flux. This suggests some other mechanism is responsible for the inward flux. From the experiments, we observed a steepening in ion temperature profile with the increasing of magnetic fields. Furthermore, fast-framing imaging of the fluctuations show the development of a pronounced feature propagating in the ion diamagnetic drift direction and co-existing with previously existing drift-wave like features located in the center region where T_i steepens. KH instability also is likely, particularly in the outer regions of the plasma. By applying the experimental parameters into a simple linear model, we obtain a negative real frequency and a linear growth rate at B = 1200G, which confirms the existence of a strong ITG instability at B = 1200G. Therefore, a robust ITG instability occurs in the same conditions where an inward particle flux developed. Noting that electron temperature gradients have been

significant in previous CSDX experiments, we used published theory to work out the condition for a net inward particle flux driven by thermal electron-ion mixing mode mechanism. No reliable electron temperature profiles are yet available for the 15 cm m=1 source used in these experiment. Previous measurements of T_e profiles in other smaller sources in CSDX show that the electron temperature gradient gets steeper as the magnetic field was increased, and suggest that the electron temperature gradient in the these new experiments may be significant enough to reverse the particle flux. However further study of T_e profile is clearly needed and in particular independent diagnostics are needed to confirm the T_e profile before a clearer conclusion can be drawn between the up-gradient flux observations and the possible role of the so-called "mixing mode" as an explanation of these results. Also due to the observation of a parallel flow shear in our experiments at ~1200G, the possible role of parallel flow shear is examined for driving an inward pinch. We found that in these CSDX-U experiments, the parallel flow shear driven inward pinch has negligible effect on driving an inward flux comparing to ion mixing mode. Thus based on this initial survey of possible linear instabilities, a drift wave combined with ion temperature gradient and electron temperature gradients, i.e. the so-called "mixing mode" appears to emerge as the most likely instability responsible for the up-gradient flux. Reliable T_e profiles in these new experiments are needed to determine if this is indeed the case.

Chapter 6

Summary and future plans

6.1 Summary and discussion

Inward particle transport has been observed in many different plasma devices as we described in Chapter 1. However, so far there have been no explicit physics explanation for this phenomena and no studies of how the turbulent statistics lead to the development of the up-gradient inward particle flux profile. Since the theory of drift wave turbulence suggests a diffusive, down-gradient particle transport. It is then clear that new components of gradient driving force must be taken into consideration. In light of this state of affairs at the beginning of this thesis we identified the following questions to be answered by our work:

1. Is this net inward particle transport observed from experiments real, i.e. can the same physics phenomena be confirmed in a single experiment using multiple, independent diagnostics?

2. In a drift wave turbulence/ zonal flow system, what is the relationship, if any, between the universally observed density steepening, particle transport and zonal flow?

3. Can we confirm the hypnosis that the inward flux is driven by flow with linear instability analysis using the same experimental parameters?

4. If it is not the flow drives the inward flux, then what are the other possible candidates responsible for the inward flux?

To answer the first question, we performed experiments in different plasma discharge conditions with different independent diagnostics, the Langmuir probes and high-speed imaging. Due to the high correlation of ion saturation current and light intensity, we can compare the experimental results from probes and camera. First of all, by measuring ion saturation current fluctuations and fluctuating $\mathbf{E} \times \mathbf{B}$ radial velocity we obtained the time-averaged turbulent particle flux radial profiles for different magnetic fields from probes. Similarly, by measuring light intensity fluctuations and effective fluctuating radial velocity by TDE method, we can calculate the effective mean turbulent intensity flux. We found that as we increased the magnetic fields from very low magnetic fields (B = 400G) to a certain high magnetic field ($B \sim 1300G$), a similar evolution of inward turbulent flux from both diagnostics has been observed. Secondly, by applying the conditional averaging analysis method, we find that when and where this up-gradient flux occurs, the turbulent structures which carried positive density fluctuations ($\tilde{n} > \sigma_n$) move inward against the density gradient and the negative density excursion ($\tilde{n} < -\sigma_n$) move outward down the density gradient. The bulk (80%) of the up-gradient flux is carried by large amplitude (exceeding one standard deviation) positive (negative) density perturbations that move up (down) the density gradient. Then the high-speed imaging provides a more direct picture of inward particle motion. The velocity fields that were obtained from velocimetry of the camera movies showed the development of the spiral inward

motion of turbulent density structures , consistent with probe measurements of inward fluxes.

It has been known that in a collisional drift wave system, the primary free energy source comes from the mean density gradient (later the ion temperature gradient also needs to be taken into account) and the particles move outward, down the density gradient. While our experimental findings indicate the existence of net inward particle flux in a drift-ZF system. Previous experiments on CSDX have shown that at moderate magnetic fields the plasma develops coherent, finite amplitude collisional drift wave fluctuations in the region around the density gradient maximum. As the magnetic field is increased further, a velocity shear was observed developed at outer region of plasma. Detailed study of turbulence-driven shear flow has been reported in elsewhere literatures [7,51]. Experiments reported in this dissertation were carried on Upgraded-CSDX, which allowed us to increase magnetic field beyond the limit of drift resistive wave instability. It has been found that the as we increase magnetic field approach to 1200G (onset of inward particle flux) plasma develops two velocity shear layers that sit on either side of the density gradient maximum [21,46] and the density gradient gets steepened. In the region between the maximum density gradient and outer shear layer, a net inward flux is observed.

Based on those findings, we then calculated the turbulent Reynolds work for the conditions before and at onset of inward particle flux separately. Before the onset of inward particle flux (B~1000G), the turbulent Reynolds work were positive at all radii, which agrees with previous experimental observations that the turbulence gives rise to the zonal flow via turbulent Reynolds stress. At the onset of inward particle

flux, at the outer shear layer the turbulent stress does work on and sustains the shear flow against dissipation, consistent with earlier results [47-51,55,69,73].However, in the region of this up-gradient flux occurs, the zonal flow does work on the fluctuations that appears to be responsible for the up-gradient flux. These observations imply that there is a link between flow shear and inward particle flux formation and therefore lead to the second question "In a drift wave turbulence/ zonal flow system, what is the relationship, if any, between the universally observed density steepening, particle transport and zonal flow?"

To answer this question, we need to seek the causality between velocity shear and inward particle flux. A cross-correlation analysis of these inward-transport structures showed that the fluctuations that moves particles against density gradient are significantly correlated with azimuthal mean velocity shear with a finite time delay (~ 18 μs), indicating that a transient increase in the local azimuthal shearing rate is followed by a subsequent increase in the inward-directed fluctuation-driven particle flux. Thus, velocity shear is essential for driving the up-gradient particle flux.

To directly measure the energy exchange rates among different frequencies, especially between turbulence and shear flows that allows us to determine the energy transfer from turbulence to shear flows through nonlinear processes, we applied a cross-bispectrum analysis. Experiments with this technique showed that at r = 6cm, where the outer velocity shear layer is located, the kinetic energy was nonlinearly transferred from fluctuations with higher frequencies into shear flows with low frequencies (f <1 kHz) consistent expectations for a turbulent-driven zonal flow. However, at r = 4.5cm, where the net particle flux is negative, the fluctuations which

are responsible for the inward particle flux are *gaining energy* from the low frequency (f <1-2 kHz) sheared flow. This provides yet an additional piece of evidence linking the shear flow to the generation of the inward, up-gradient particle flux. It was also found through experiments that the radial component of vorticity flux is dominantly responsible for the kinetic energy transfer to shear flows, which suggested that the vorticity flux mediates the transfer of kinetic energy.

Although experimental results suggest a strong link between flow and inward particle flux, it is important to confirm this hypnosis with linear stability analyses. Thus third question that "can we confirm the hypnosis that the inward flux is driven by flow with linear instability analysis using the same experimental parameters?" was answered. We used a simple, linear modified Hasengea-Wakatani theory model to describe the time evolution of the coupled potential-density fluctuations, with presence of the density and azimuthal flow profiles. Applying the density profiles and $\mathbf{E} \times \mathbf{B}$ azimuthal velocity profiles from experiments into this modified linear model, we failed to obtain a net inward quasilinear particle flux. This result then leads to the the last question "If it is not the flow drives the inward flux, then what are the other possible candidates responsible for the inward flux?"

The most likely candidate according to the recent experimental results on our machine is the ITG driven inward pinch by thermal-ion mixing mode mechanism. The ion temperature profiles measured by LIF measurement show a significant steepening in ion temperature profile around r ~ 2 cm when the inward particle flux was observed to occur. At the same time, the density profile at the region where T_i steepens remain almost the same, which is one of the typical features of ITG. Also from the fast

imaging data, pronounced ion fluctuation features propagating in ion diamagnetic drift direction located inside r ~ 3 cm region, where the T_i gradient is located, under conditions that lead to the inward or up-gradient flux. Long published theory has already predicted that the ITG can drive an inward pinch by ion mixing mode mechanism. To get a net inward particle flux, the η_e is supposed to be close to 2/3 which is very likely satisfied by our experiments. However, future experiments to measure electron temperature profiles are required.

Taken together, in this dissertation we directly show for the first time that a net inward, up-gradient turbulent particle fluxes , and that this up-gradient flux occurs when and where a change in sign of the work done by the sheared flow on the smaller scaled higher frequency fluctuations. Thus we put forward hypnosis that this inward up-gradient flux is caused by the radially sheared azimuthal flow. However the modified Hasegawa-Wakatani model which considers only two fields, the density and vorticity, does not produce an inward flux, suggesting some other mechanism is responsible for the inward flux. We summarize recent new experimental results which point towards the possible role of finite ion temperature gradient effects, possibly combined with parallel flow shear, in driving up-gradient particle flux.

6.2 Limitations of present work

In the work presented in the dissertation, there are several limitations needed to be furthered improved. First of all, when using the electric field calculated from floating potential instead of plasma space potential to estimate fluctuating $\mathbf{E} \times \mathbf{B}$ velocity, we ignored the temperature fluctuation. More significantly, our analyses of

the stability of the experimental profiles has pointed to the need to carefully measure the T_e profile with multiple independent diagnostics in order to determine if the so-called "ion mixing mode" can lead to the observed up-gradient fluxes. In current work there are no detailed information of the ion-ion collisional viscosity profiles, which are needed for understanding the details of the momentum balance between the Reynolds stress and the flow damping.

Based on the accomplishments and the limitations of the present work there are some recommendations for future experimental work for a better study of underlying physics for inward particle flux.

6.3 Recommendation for Future Work

6.3.1 Better measurements for electron temperature T_e

Current analysis of the electron temperature from the I–V characteristics of swept Langmuir probes used in this source reveals a non-Maxwellian plasma in the region between r = 5 cm and 9 cm for B > 1200G. In Figure 6-1 I–V characteristics for two different magnetic fields are shown, both measured at the same radial position r = 6 cm. The slope of the I–V curve at B = 500G denotes a single-T_e plasma. At larger magnetic fields, several slopes appear, indicating a non-Maxwellian plasma. In Figures 6-1(b) and (c), we show two electron temperatures, one calculated from the smallest slope and the other calculated from the slope near the beginning of the exponentially increasing region of the I–V characteristics. We see that there is a

predominant low energy component around $T_e \sim 4$ eV near the center for all B. Near the magnetic field threshold this increases slightly to ~6 eV at the edge.

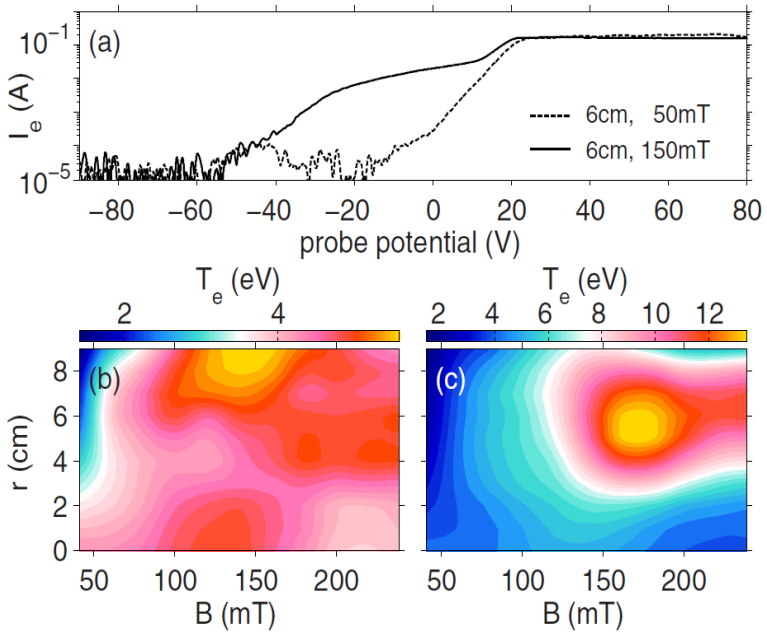

Figure 6-1 (a) I–V –characteristics for two different magnetic fields (b) for the lowest detected values and (c) obtained at the start of exponential increase of electron current. [21]

Thus the different fit of I-V curve gives us two different T_e profiles. As we discussed the ion mixing mode mechanism in previous chapter, in order to obtain a net inward particle flux there is a threshold for η_e to be larger than 2/3. Thus a more accurate of fast electron temperature measurement should be made. A One possible method is to use triple probe, consisting of two electrodes biased with the same voltage and a third which is floating. The schematic is shown in Figure 6-2. The electron temperature is computed as $kT_e = \frac{e(V_e - V_f)}{\ln(1+\frac{A_i}{A_e})}$, where V_e and V_f are the voltage of

the electron collecting tip and floating tip respectively, and A_i and A_e are the collecting area of the ion tip and electron tip respectively. It may also be possible to seed these Argon discharges with a small amount of He gas, and then use the He line ratio technique to independently determine n and T_e profiles. This technique is under development for our device and will be reported in future work.

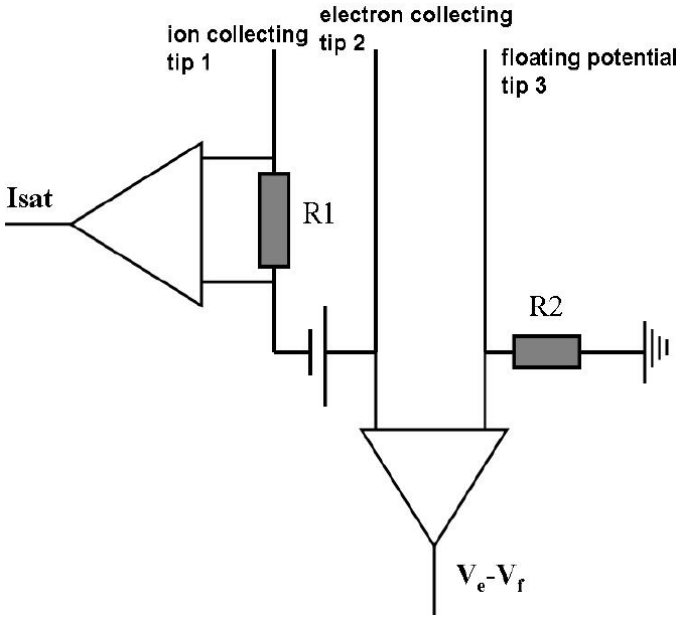

Figure 6-2 Schematic of triple probe measurement.

6.3.2 Investigation of interaction between vorticity, density gradient and velocity shear

It has already been known that at low magnetic fields, the velocity shear is weak thus the diffusive process is dominant. Turbulent eddies with positive density fluctuations are repelled from mean density gradient. Therefore the particles move down the density gradient. For higher magnetic fields, there is a density gradient located at inner region of plasma with a strong velocity gradient at the edge. Interaction between eddies and velocity shear becomes comparably significant. According to the drift wave-zonal flow theory mode, a vorticity gradient is required for inward particle flux. We can apply the conditional averaging approach to analyze spatiotemporal fluctuation. This analysis allows the study of the turbulent structure radial motion and interaction with the plasma shear layer. When the instantaneous fluctuating positive quantity $\tilde{\xi}$ (which denotes either $\tilde{n}$ or $\tilde{\omega}$) exceeds one standard deviation σ_ξ at time a, thus an event is considered being triggered. Meanwhile, a time window with length of $\Delta\tau$ is selected around i, and the corresponding data associated with this positive fluctuating event is selected too. After averaged over many windows, only the vortices large enough to trigger the events will survive, and smaller amplitude will then be averaged away.

The mean flow velocity has a mean vorticity $\bar{\omega} = \frac{\partial \bar{V}_\theta}{\partial r} < 0$. It appears that turbulent vortices with $\tilde{\omega} < 0$ are attracted towards the $\bar{\omega} < 0$ mean shear flow region while vortices with $\tilde{\omega} > 0$ are repelled away from this region. This somehow relates to

a vortex merging process which may cause the amplification of the $\mathbf{E} \times \mathbf{B}$ shear layer. Prograde turbulent vortices (i.e. turbulent structures with negative vorticity) are attracted towards the shear layer with negative vorticity, where they are absorbed. Turbulent structures with opposite (i.e. retrograde) vorticity are repelled from the $\mathbf{E} \times \mathbf{B}$ shear layer. As a result the shear layer is amplified by its interaction with these vortices. The associated density fluctuations give rise to an inward-going flux of high density structures and an outward going flux of low density structures

6.3.3 Changing gas species from Argon to Helium /Hydrogen

In theory, normalized gyro-radius according to $\frac{\rho_s}{L_n} = \frac{\sqrt{m_i T_e}}{(eB)L_n}$ is an important parameter in Hasengawa-Wakatani model and is expected to be very small for a better fit of the model. This requires the machine operated through a larger range of magnetic fields (which has been already achieved) and using gases with lighter ions such as Helium, or even Hydrogen. Replacing Argon with Helium or Hydrogen can help us to generalize the experimental results measured on a linear helicon plasma device to tokamaks fusion plasma, or to compare with theoretical and computational models is needed.

6.3.4 A testing of ideas from linear machines on tokamak plasmas

Very similar observations of inward particle flux and density steepening have been reported on many fusion devices. In principle, similar measurements of the energy transfer rates, the Reynolds stress and background poloidal and toroidal flow

velocities could be easily achieved in tokamak devices. This would be a direct test to see whether the similar mechanisms for inward particle flux physics picture at CSDX-U plasma is operative in tokamak fusion plasmas especially in the edge transport barrier (i.e. H-mode transition) and during formation of internal transport barriers when magnetic shear gets small. Table 4 shows the relevance of this dissertation to tokamak physics: 1) during LOC-SOC Transition and ECH regime, there is a change of the dominant type of turbulence Dws – ITG. In our experiments, we observed the similar changes in mode types from pure DWs to DWs coexisted with ITGs with increasing B filed. 2) in tokamak, the inward pinch that leads to the peaking in density profile remains an interesting topic. While in our linear plasma experiments, we observed not only an inward pinch but a net inward particle flux. 3) As we know the saturation for predator- prey is decided by flow damping. Flow damping via ion-electron collisional has been observed in experiments, which there is rarely a report of collisionless ZF damping. This dissertation shows a change in sign of RS work that the flow is losing energy in turbulence, suggesting a collisionless ZF damping. 4) Experimental studies of intrinsic rotation have been conducted on tokamak. Due to limitation of fluctuation measurement, it is difficult to calculate to residual stress. In our simple linear plasma device, we can measure fluctuations to calculate turbulent parallel Reynolds stress$\langle \tilde{v}_r \tilde{v}_\parallel \rangle$. By making approximation for turbulent momentum diffusivity $\chi_\parallel = \langle \tilde{v}_r^2 \rangle \tau_c$, we can obtain residual stress via equation $S_{r\parallel}^{res} = \langle \tilde{v}_r \tilde{v}_\parallel \rangle + \langle \tilde{v}_r^2 \rangle \tau_c \frac{\partial \langle V_\parallel \rangle}{\partial r}$. One of the concerns is that there is no magnetic shear in CSDX, while as we know there is usually a strong magnetic shear at the edge of tokamak that will

suppress the $\mathbf{E} \times \mathbf{B}$ velocity shear [74]. This would require the design of an appropriately arranged array of probes which could then be inserted into the edge region of such a hot plasma (pedestal region). Of course, the parallel heat flux in such a device is much higher, and care would have to be taken that the probe array does not overheat and/or cause unacceptable disturbances to the tokamak plasma discharge. It is likely that multiple discharges would have to be carried out in order to obtain adequately long datasets for the required ensemble averaging.

Table 6-1 Relevance of this dissertation to Tokamak physic. [83]

Tokamak physics	**CSDX experiments**
LOC-SOC Transition; ECH regime population changes DWs → ITG	Drift, ITG fluctuation coexistence; Changes in population with B_0
Fueling physics: inward pinch; Density peaking	Mechanism for net inward flux Study of pinch physics
Collisionless ZF damping: Predator-prey model saturation	$R_T > 0 \Longrightarrow R_T < 0$ Onset of KH; ZF damping
Intrinsic rotation: Residual stress physics	Origin of $\langle V_\parallel \rangle$ Measurement of $\langle \tilde{V}_r \tilde{V}_\parallel \rangle$, calculation of Residual stress

References

[1] J. D. Lawson, P Phys Soc Lond B **70**, 6 (1957).

[2] F.F.Chen, *Introduction to plasma physics and controlled fusion Second edition Volume 1: Plasma* (Plenum Press, New York, 1984), second edn., Vol. 1.

[3] R. H. L. Hans R. Griem, *Methods of Experimental Physics, Part A* (Academic Press, New York and London, 1970).

[4] F. F. Chen, Phys Fluids **8**, 1323 (1965).

[5] P. H. Diamond, A. Hasegawa, and K. Mima, Plasma Phys Contr F **53** (2011).

[6] K. Mima and A. Hasegawa, Phys Fluids **21**, 81 (1978).

[7] Z. Yan, University of California, San Diego, 2008.

[8] N. A. Gondarenko and P. N. Guzdar, Geophys Res Lett **26**, 3345 (1999).

[9] P. H. Diamond, S. I. Itoh, K. Itoh, and T. S. Hahm, Plasma Phys Contr F **47**, R35 (2005).

[10] Kraichna.Rh, Phys Fluids **10**, 1417 (1967).

[11] S. B. Pope, *Turbulent Flows* (Cambridge University Press, Cambridge, 2000).

[12] G. R. Tynan, A. Fujisawa, and G. McKee, Plasma Phys Contr F **51** (2009).

[13] P. H. Diamond and Y. B. Kim, Phys Fluids B-Plasma **3**, 1626 (1991).

[14] P. Manz, M. Ramisch, and U. Stroth, Phys Rev Lett **103** (2009).

[15] K. Itoh, S. I. Itoh, P. H. Diamond, T. S. Hahm, A. Fujisawa, G. R. Tynan, M. Yagi, and Y. Nagashima, Phys Plasmas **13** (2006).

[16] M. Xu, University of California, San Diego, 2010.

[17] T. Tajima, W. Horton, P. J. Morrison, J. Schutkeker, T. Kamimura, K. Mima, and Y. Abe, Phys Fluids B-Plasma **3**, 938 (1991).

[18] D. L. Jassby, Phys Fluids **15**, 1590 (1972).

[19] W. Horton and J. Liu, Phys Fluids **27**, 2067 (1984).

[20] F. F. Chen, *Introduction to Plasma Physics and controlled fusion, 2nd edition* New York, 1984), Vol. Volume 1: Plasma Physics.

[21] S. C. Thakur, C. Brandt, L. Cui, J. J. Gosselin, A. D. Light, and G. R. Tynan, Plasma Sources Sci T **23** (2014).

[22] C. Bourdelle, Plasma Phys Contr F **47**, A317 (2005).

[23] W. Horton, Rev Mod Phys **71**, 735 (1999).

[24] E. J. Powers, Nucl Fusion **14**, 749 (1974).

[25] J. H. Kaplan, Annu Rev Biochem **71**, 511 (2002).

[26] A. A. M. Holtslag and C. H. Moeng, J Atmos Sci **48**, 1690 (1991).

[27] P. Urban, D. Schmoranzer, P. Hanzelka, K. R. Sreenivasan, and L. Skrbek, P Natl Acad Sci USA **110**, 8036 (2013).

[28] Falthamm.Cg, J Geophys Res **70**, 2503 (1965).

[29] Birmingh.Tj, J Geophys Res **74**, 2169 (1969).

[30] M. Schulz, in *Particle Diffusion in the Radiation Belts* (springer 1974).

[31] J. G. Lyon, Science **288**, 1987 (2000).

[32] A. C. Boxer, R. Bergmann, J. L. Ellsworth, D. T. Garnier, J. Kesner, M. E. Mauel, and P. Woskov, Nat Phys **6**, 207 (2010).

[33] F. Wagner and U. Stroth, Plasma Phys Contr F **35**, 1321 (1993).

[34] X. Garbet, L. Garzotti, P. Mantica, H. Nordman, M. Valovic, H. Weisen, and C. Angioni, Phys Rev Lett **91** (2003).

[35] G. T. Hoang, C. Bourdelle, X. Garbet, J. F. Artaud, V. Basiuk, J. Bucalossi, F. Clairet, C. Fenzi-Bonizec, C. Gil, J. L. Segui, J. M. Travere, E. Tsitrone, L. Vermare, Phys Rev Lett **93** (2004).

[36] J. Weiland, A. Eriksson, H. Nordman, and A. Zagorodny, Plasma Phys Contr F **49**, A45 (2007).

[37] D. R. Baker, in *Transport Task Force Workshop*Madison, 2003).

[38] S. H. Muller, J. A. Boedo, K. H. Burrell, J. S. deGrassie, R. A. Moyer, D. L. Rudakov, W. M. Solomon, and G. R. Tynan, Phys Plasmas **18** (2011).

[39] U. Stroth, T. Geist, J. P. T. Koponen, H. J. Hartfuss, P. Zeiler, and E. W.-a. Team, Phys Rev Lett **82**, 928 (1999).

[40] J. Boedo, D. Gray, R. Conn, S. Jachmich, G. Van Oost, R. R. Weynants, and T. Team, Czech J Phys **48**, 99 (1998).

[41] M. G. Shats and D. L. Rudakov, Phys Rev Lett **79**, 2690 (1997).

[42] T. A. Carter and J. E. Maggs, Phys Plasmas **16** (2009).

[43] J. E. Maggs, T. A. Carter, and R. J. Taylor, Phys Plasmas **14** (2007).

[44] A. Fasoli, B. Labit, M. McGrath, S. H. Muller, G. Plyushchev, M. Podesta, and F. M. Poli, Phys Plasmas **13** (2006).

[45] S. Oldenburger, S. Inagaki, T. Kobayashi, H. Arakawa, N. Ohyama, Y. Tobimatsu, A. Fujisawa, K. Itoh, S. I. Itoh, Plasma Phys Contr F **54** (2012).

[46] M. J. Burin, G. R. Tynan, G. Y. Antar, N. A. Crocker, and C. Holland, Phys Plasmas **12** (2005).

[47] C. Holland, J. H. Yu, A. James, D. Nishijima, M. Shimada, N. Taheri, and G. R. Tynan, Phys Rev Lett **96** (2006).

[48] M. Xu, G. R. Tynan, C. Holland, Z. Yan, S. H. Muller, and J. H. Yu, Phys Plasmas **17** (2010).

[49] Z. Yan, M. Xu, P. H. Diamond, C. Holland, S. H. Muller, G. R. Tynan, and J. H. Yu, Phys Rev Lett **104** (2010).

[50] C. Holland, G. R. Tynan, J. H. Y. A. James, D. Nishijima, M. Shimada, and N. Taheri, Plasma Phys Contr F **49**, A109 (2007).

[51] Z. Yan, G. R. Tynan, C. Holland, M. Xu, S. H. Muller, and J. H. Yu, Phys Plasmas **17** (2010).

[52] A. Hasegawa and M. Wakatani, Phys Rev Lett **59**, 1581 (1987).

[53] S. C. Thakur, M. Xu, P. Manz, N. Fedorczak, C. Holland, and G. R. Tynan, Phys Plasmas **20** (2013).

[54] G. R. Tynan, A. D. Bailey, G. A. Campbell, R. Charatan, A. deChambrier, G. Gibson, D. J. Hemker, K. Jones, A. Kuthi, C. Lee, T. Shoji, M. Wilcoxson, Journal of Vacuum Science & Technology a-Vacuum Surfaces and Films **15**, 2885 (1997).

[55] M. Xu, G. R. Tynan, P. H. Diamond, C. Holland, J. H. Yu, and Z. Yan, Phys Rev Lett **107** (2011).

[56] T. Shikama, S. Kado, A. Okamoto, S. Kajita, and S. Tanaka, Phys Plasmas **12** 044504 (2005).

[57] I. H. Hutchinson, Plasma Phys Contr F **47**, 71 (2005).

[58] S. C. Thakur, D. McCarren, T. Lee, N. Fedorczak, P. Manz, E. E. Scime, G. R. Tynan, and M. Xu, Phys Plasmas **19** (2012).

[59] G. Y. Antar, J. H. Yu, and G. Tynan, Phys Plasmas **14** (2007).

[60] S. Oldenburger, C. Brandt, F. Brochard, N. Lemoine, and G. Bonhomme, Rev Sci Instrum **81** (2010).

[61] A. D. Light, S. C. Thakur, C. Brandt, Y. Sechrest, G. R. Tynan, and T. Munsat, Phys Plasmas **20** (2013).

[62] H. Johnsen, H. L. Pecseli, and J. Trulsen, Phys Fluids **30**, 2239 (1987).

[63] M. Xu, G. R. Tynan, C. Holland, Z. Yan, S. H. Muller, and J. H. Yu, Phys Plasmas **16** (2009).

[64] Y. C. Kim and E. J. Powers, Ieee T Plasma Sci **7**, 120 (1979).

[65] C. Holland, G. R. Tynan, G. R. McKee, and R. J. Fonck, Rev Sci Instrum **75**, 4278 (2004).

[66] J. M. Beall, Y. C. Kim, and E. J. Powers, J Appl Phys **53**, 3933 (1982).

[67] P. H. Diamond, C. J. McDevitt, O. D. Gurcan, T. S. Hahm, W. X. Wang, E. S. Yoon, I. Holod, Z. Lin, V. Naulin, R. Singh Nucl Fusion **49** (2009).

[68] P. H. Diamond, S. Champeaux, M. Malkov, A. Das, I. Gruzinov, M. N. Rosenbluth, C. Holland, B. Wecht, A. I. Smolyakov, F. L. Hinton, Z. Lin, T. S. Hahm, Nucl Fusion **41**, 1067 (2001).

[69] G. R. Tynan, C. Holland, J. H. Yu, A. James, D. Nishijima, M. Shimada, and N. Taheri, Plasma Phys Contr F **48**, S51 (2006).

[70] J. A. Boedo, D. Rudakov, R. Moyer, S. Krasheninnikov, D. Whyte, G. McKee, G. Tynan, M. Schaffer, P. Stangeby, P. West, S. Allen, T. Evans, R. Fonck, E. Hollmann, A. Leonard, A. Mahdavi, G. Porter, M. Tillack, G. Antar, Phys Plasmas **8**, 4826 (2001).

[71] P. H. Diamond and T. S. Hahm, Phys Plasmas **2**, 3640 (1995).

[72] T. Hwa and M. Kardar, Phys Rev A **45**, 7002 (1992).

[73] Z. Yan, G. R. Tynan, C. Holland, M. Xu, S. H. Muller, and J. H. Yu, Phys Plasmas **17** (2010).

[74] T. Chiueh, P. W. Terry, P. H. Diamond, and J. E. Sedlak, Phys Fluids **29**, 231 (1986).

[75] P. Manz, M. Xu, S. C. Thakur, and G. R. Tynan, Plasma Phys Contr F **53** (2011).

[76] G. Tynan, in *22nd IAEA Fusion Energy Conference*, Geneva, (2008).

[77] G. R. Tynan, P. H. Diamond, C. Holland, S. H. Muller, M. Xu, Z. Yan, and J. Yu, Plasma Phys Contr F **51** (2009).

[78] B. Coppi and C. Spight, Phys Rev Lett **41**, 551 (1978).

[79] P. H. Diamond, S. I. Itoh, and K. Itoh, *Modern plasma physics* (Cambridge University Press, Cambridge, UK ; New York, 2010).

[80] A. Ashourvan, US/EU Transport Task Force Workshop, Salem, 2005

[81] P. Veazi, US/EU Transport Task Force Workshop, Salem, 2005

[82] L. Cui, G. R. Tynan, P. H. Diamond, S. C. Thakur and C. Brandt, Phys. Plasmas **22**, 050704 (2015).

[83] L. Cui, *" Physics of Up-gradient Particle Flux in Drift-ITG turbulence"*, presented in US/EU Transport Task Force Workshop, Salem, 2005.